A&A 572, A21 (2014)
DOI: 10.1051/0004-6361/201424267

Astronomy & Astrophysics

Water in star-forming regions with *Herschel* (WISH)

V. The physical conditions in low-mass protostellar outflows revealed by multi-transition water observations⋆,⋆⋆,⋆⋆⋆

J. C. Mottram[1], L. E. Kristensen[2], E. F. van Dishoeck[1,3], S. Bruderer[3], I. San José-García[1], A. Karska[3], R. Visser[4], G. Santangelo[5,6], A. O. Benz[7], E. A. Bergin[4], P. Caselli[8,3], F. Herpin[9,10], M. R. Hogerheijde[1], D. Johnstone[11,12,13], T. A. van Kempen[1], R. Liseau[14], B. Nisini[6], M. Tafalla[15], F. F. S. van der Tak[16,17], and F. Wyrowski[18]

[1] Leiden Observatory, Leiden University, PO Box 9513, 2300 RA Leiden, The Netherlands
e-mail: mottram@strw.leidenuniv.nl
[2] Harvard-Smithsonian Center for Astrophysics, 60 Garden Street, Cambridge, MA 02138, USA
[3] Max Planck Institut für Extraterrestrische Physik, Giessenbachstrasse 1, 85748 Garching, Germany
[4] Department of Astronomy, University of Michigan, 500 Church Street, Ann Arbor, MI 48109-1042, USA
[5] Osservatorio Astrofisico di Arcetri, Largo Enrico Fermi 5, 50125 Florence, Italy
[6] Osservatorio Astronomico di Roma, via di Frascati 33, 00040 Monteporzio Catone, Italy
[7] Institute for Astronomy, ETH Zurich, 8093 Zurich, Switzerland
[8] School of Physics and Astronomy, University of Leeds, Leeds LS2 9JT, UK
[9] Université de Bordeaux, Observatoire Aquitain des Sciences de l'Univers, 2 rue de l'Observatoire, BP 89, 33270 Floirac Cedex, France
[10] CNRS, LAB, UMR 5804, Laboratoire d'Astrophysique de Bordeaux, 2 rue de l'Observatoire, BP 89, 33270 Floirac Cedex, France
[11] Joint Astronomy Centre, 660 North Aohoku Place, University Park, Hilo, HI 96720, USA
[12] Department of Physics and Astronomy, University of Victoria, PO Box 3055 STN CSC, Victoria, BC V8W 3P6, Canada
[13] NRC-Herzberg Institute of Astrophysics, 5071 West Saanich Road, Victoria, BC V9E 2E7, Canada
[14] Department of Earth and Space Sciences, Chalmers University of Technology, Onsala Space Observatory, 439 92 Onsala, Sweden
[15] Observatorio Astronómico Nacional (IGN), Alfonso XII 3, 28014 Madrid, Spain
[16] SRON Netherlands Institute for Space Research, PO Box 800, 9700 AV Groningen, The Netherlands
[17] Kapteyn Astronomical Institute, University of Groningen, PO Box 800, 9700 AV Groningen, The Netherlands
[18] Max-Planck-Institut für Radioastronomie, Auf dem Hügel 69, 53121 Bonn, Germany

Received 24 May 2014 / Accepted 19 September 2014

ABSTRACT

Context. Outflows are an important part of the star formation process as both the result of ongoing active accretion and one of the main sources of mechanical feedback on small scales. Water is the ideal tracer of these effects because it is present in high abundance for the conditions expected in various parts of the protostar, particularly the outflow.
Aims. We constrain and quantify the physical conditions probed by water in the outflow-jet system for Class 0 and I sources.
Methods. We present velocity-resolved *Herschel* HIFI spectra of multiple water-transitions observed towards 29 nearby Class 0/I protostars as part of the WISH guaranteed time key programme. The lines are decomposed into different Gaussian components, with each component related to one of three parts of the protostellar system; quiescent envelope, cavity shock and spot shocks in the jet and at the base of the outflow. We then use non-LTE RADEX models to constrain the excitation conditions present in the two outflow-related components.
Results. Water emission at the source position is optically thick but effectively thin, with line ratios that do not vary with velocity, in contrast to CO. The physical conditions of the cavity and spot shocks are similar, with post-shock H_2 densities of order 10^5–10^8 cm^{-3} and H_2O column densities of order 10^{16}–10^{18} cm^{-2}. H_2O emission originates in compact emitting regions: for the spot shocks these correspond to point sources with radii of order 10–200 AU, while for the cavity shocks these come from a thin layer along the outflow cavity wall with thickness of order 1–30 AU.
Conclusions. Water emission at the source position traces two distinct kinematic components in the outflow; J shocks at the base of the outflow or in the jet, and C shocks in a thin layer in the cavity wall. The similarity of the physical conditions is in contrast to off-source determinations which show similar densities but lower column densities and larger filling factors. We propose that this is due to the differences in shock properties and geometry between these positions. Class I sources have similar excitation conditions to Class 0 sources, but generally smaller line-widths and emitting region sizes. We suggest that it is the velocity of the wind driving the outflow, rather than the decrease in envelope density or mass, that is the cause of the decrease in H_2O intensity between Class 0 and I sources.

Key words. stars: formation – ISM: jets and outflows – ISM: molecules – stars: protostars

⋆ *Herschel* is an ESA space observatory with science instruments provided by European-led Principal Investigator consortia and with important participation from NASA.
⋆⋆ Appendices are available in electronic form at http://www.aanda.org
⋆⋆⋆ Reduced spectra are only available at the CDS via anonymous ftp to cdsarc.u-strasbg.fr (130.79.128.5) or via http://cdsarc.u-strasbg.fr/viz-bin/qcat?J/A+A/572/A21

1. Introduction

Molecular outflows are a ubiquitous and necessary part of the star formation process. They remove angular momentum and material from the protostellar environment in a feedback process which helps the protostar form a disk and gain mass in the short-term while ultimately conspiring with the initial core conditions to starve it in the long term. Thus understanding outflows is at the heart of developing a true law of star formation which can predict the stellar outcome based on initial core properties.

The classical tracer of such outflows, low-J CO ($J \leq 4$), traces material in a mixing layer which has undergone turbulent entrainment from the quiescent envelope (e.g. Canto & Raga 1991; Raga et al. 1995) with gas temperatures of order 50−100 K (e.g. Yıldiz et al. 2013). This carries away a significant amount of mass from the envelope, but at relatively low velocities of order 5−20 km s^{-1} and likely from material entrained at some distance from the protostar. Therefore, the properties derived from this emission may not accurately reflect the total momentum, angular momentum and kinetic energy transport of the system. In addition, it does not trace the active surface where the envelope is currently being sculpted (e.g. Nisini et al. 2010; Santangelo et al. 2013) and so does not probe the true feedback conditions.

In contrast, protostellar jets, as traced in atomic gas or shocked H_2 (e.g. Reipurth et al. 2000), are more directly linked with accretion onto the central protostar (e.g. Pudritz et al. 2007; Shang et al. 2007). This material is moving faster (100−1000 km s^{-1}, Frank et al. 2014) and is at higher temperatures but lower H_2 number densities compared to the outflow (of order 10^3−10^4 K and $n_H \sim 10^3$−10^4 cm^{-3} respectively, Bacciotti & Eislöffel 1999), and therefore has higher momentum and kinetic energy but lower mass. So-called "bullets" can be seen in molecular species such as CO, SiO and more recently H_2O (Bachiller et al. 1990, 1991; Hirano et al. 2006; Santiago-García et al. 2009; Kristensen et al. 2011), where material is compressed (and thus cools more efficiently) due to shocks within the jet. However, the pencil-beam nature of the jet means that it is unlikely to be a major factor in the disruption of the envelope as the protostar evolves from Class 0 ($T_{bol} < 70$ K) to Class I ($70 \leq T_{bol} < 650$ K; Lada & Wilking 1984; Andre et al. 1993).

Between these two extremes are two intermediate regions; the outflow cavity which may be filled with a wind which has a similar or larger density than the jet (Panoglou et al. 2012), and the active cavity shock at the boundary between the cavity and the quiescent envelope (e.g. Velusamy et al. 2007; Visser et al. 2012). For the latter, the gas temperature and H_2 number density are of order 300−1000 K and 10^5−10^7 cm^{-3} respectively, as traced by H_2O and high-J CO (e.g. Goicoechea et al. 2012; Karska et al. 2014; Kristensen et al. 2013), while the dust is below 100 K. Studies based on *Herschel* PACS (Poglitsch et al. 2010) and/or SPIRE (Griffin et al. 2010) observations see multiple distinct temperature components in CO excitation diagrams: cold emission (~100 K) for $J < 14$, warm emission (~300 K) for $14 \lesssim J \lesssim 24$ and sometimes also hot emission (~750 K) for $J \gtrsim 24$ with the column density decreasing with increasing temperature (Manoj et al. 2013; Karska et al. 2014; Green et al. 2013). However, these observations are spectrally unresolved, which makes relating these temperature components to physical parts of the protostar more challenging.

Therefore, how the physical and excitation conditions in the different parts of protostellar outflow-jet systems are related, and how these vary both with distance from the central protostar and between sources, is not currently well understood. In addition, while outflow line-width and force decrease on average as the protostar evolves (Bontemps et al. 1996), in particular from Class 0 to Class I, it is not clear if this is because the outflow actually decreases in strength or simply because there is less envelope material available to reveal its presence.

Water is the ideal molecule to resolve these questions. It is the primary ice constituent and oxygen reservoir in protostellar envelopes, sublimates at dust temperatures above ~100 K and can also be formed efficiently in the gas phase at temperatures above a few 100 K (see van Dishoeck et al. 2013, and references therein). At shock velocities above ~10−20 km s^{-1} it can also be sputtered from the grain mantles (see e.g. Jiménez-Serra et al. 2008a; Van Loo et al. 2013; Neufeld et al. 2014; Suutarinen et al. 2014). It is therefore potentially present in relatively high abundance in the gas-phase in the cavity shock, wind and shocks within the jet. Water also has a large dipole moment and Einstein A coefficients, and therefore more intense line emission than species with smaller dipole moments. Even for subthermal excitation, where the number density is well below the critical density, water lines can be more easily detected than emission from species such as CO. The favourable combination of these factors makes water a good tracer of the kinematics of these regions.

The expected kinematic signatures are related to the properties of the shocks in the outflow and jet (see, e.g. Draine 1980; Hollenbach 1997). In discontinuous, "jump" (J-type) shocks, there is a sharp increase in the acceleration of gas in the shock with respect to the ambient un-shocked material by the passage of the shock front. The line-centre of the emission from these molecules is therefore shifted from the source velocity to some fraction of the shock velocity dependent on the viewing angle. The distribution of velocities in the post-shock material, and thus the FWHM of the emission line, will also be different from that of the ambient material. Alternatively, in "continuous" (C-type) shocks, the molecules are smoothly accelerated by the shock and so emission extends from the source velocity to the velocity of the shock. Therefore, for the same shock geometry larger line-widths are expected for C-type shocks. Hybrid C-J-type shocks can be formed if the shock conditions are such that a C-type shock does not have time to reach steady-state; in this case, a J-type front develops at the time the shock is truncated (Chieze et al. 1998). For simplicity, in the remainder of the paper we will only refer to C and J shocks given the time dependant nature of C-J shocks. Multiple discrete shocks with different conditions or orientations with respect to the line of sight will give rise to multiple emission line components. It is also possible that both C and J type shocks exist as part of the same structure (e.g., see Fig. 9 of Suutarinen et al. 2014), in which case the physical conditions will be similar but the two shocks will produce different line profiles.

Strong, broad and complex line profiles have been observed in water towards Class 0 and I protostars (Kristensen et al. 2010, 2012), most recently using the *Herschel* Space Observatory (Pilbratt et al. 2010) as part of the "Water in star-forming regions with *Herschel*" (WISH; van Dishoeck et al. 2011) guaranteed time key programme. These have been complemented by spectra at off-source positions along several promenant outflows (Santangelo et al. 2012, 2013; Vasta et al. 2012; Nisini et al. 2013). While Kristensen et al. (2012) looked at the dynamical components for one water line, the 1_{10}−1_{01} ground-state transition at 557 GHz, this paper seeks to use multiple water transitions to probe the excitation conditions and water chemistry in these sources. In addition, studying how the excitation of water varies between the different physical components is required to

disentangle the temperature components seen in spectrally unresolved PACS/SPIRE observations.

The goals of this paper are therefore: to use the multiple transitions of water observed towards low-mass Class 0/I protostars as part of the WISH survey to identify the physical conditions present where water is emitting within low-mass protostellar outflows, to understand the differences and similarities between the conditions in the various parts of the jet-outflow system, and to explore how this changes with source evolution.

We begin with a brief description of the sample and observations used for this study in Sect. 2. Next, we present our results in Sect. 3 and additional analysis in Sect. 4. We then discuss the implications of these results in Sect. 5, both in terms of the different parts of the jet-outflow system (Sect. 5.1), the impact of source evolution (Sect. 5.2), and comparison to off-source shocks (Sect. 5.4). Finally, we summarise our main findings and reach our conclusions in Sect. 6.

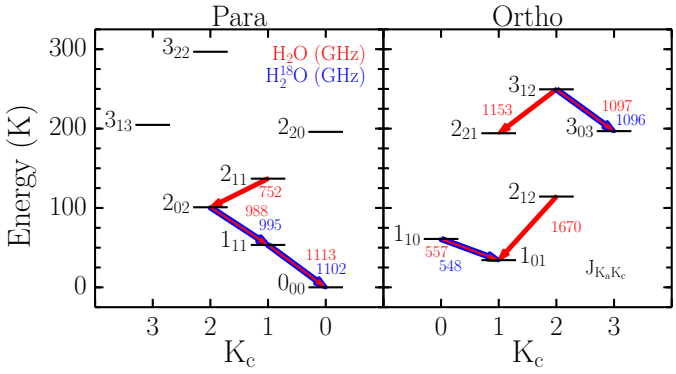

Fig. 1. Level diagram of the various H_2O (red) and $H_2^{18}O$ (blue) transitions observed with HIFI towards the WISH sample of low-mass protostars.

2. Observations

The WISH low-mass sample consists of 15 Class 0 and 14 Class I sources, the properties of which are given in Table 1. All sources have been independently verified as truly embedded sources and not edge-on disks.

This sample was the target of a series of observations of gas-phase water transitions with the Heterodyne Instrument for the Far-Infrared (HIFI; de Graauw et al. 2010) on *Herschel* between March 2010 and October 2011. Three of the Class I sources (IRAS3A, RCrA-IRS5A and HH100-IRS) were only observed in the 557 GHz H_2O $1_{10}-1_{01}$ line, which was presented for all sources by Kristensen et al. (2012). All other sources were observed in between four and seven $H_2^{16}O$ transitions and between one and four $H_2^{18}O$ transitions. Additional data from two OT2 programmes, OT2_rvisser_2 and OT2_evandish_4, are also included to augment the WISH data.

Details of the line frequency, main-beam efficiency, spectral and spatial resolutions, observing time, critical density at 300 K and upper level energy of the observed transitions are given for all lines in Table A.1. Settings primarily targeting $H_2^{18}O$ transitions were only observed towards Class 0 sources where higher line intensities were expected compared to Class I sources. This also motivated the longer integrations in the H_2O $1_{11}-0_{00}$ transition for Class 0 than Class I sources as that setting also includes the corresponding $H_2^{18}O$ transition. Longer integrations were performed for Class I sources in the $1_{10}-1_{01}$ transition to ensure detections in at least one line in the maximum number of sources. A level diagram of the various lines is shown in Fig. 1 and the observations identification numbers of all data used in this paper are given in Table A.2.

All observations were taken in both horizontal and vertical polarisations with both the Wide Band Spectrometer (WBS) and High Resolution Spectrometer (HRS) backends. Observations were taken as single pointings in dual-beam-switch (DBS) mode with a chop throw of 3′, with the exception of some of the H_2O $1_{10}-1_{01}$ observations, which were taken in position-switch mode (see Kristensen et al. 2012, for more details). The *Herschel* beam ranges from 12.7″ to 38.7″ over the frequency range of the various water lines, close to the diffraction limit of the primary mirror.

The data were reduced with HIPE (Ott 2010). After initial spectrum formation, further processing was also performed using HIPE. This began with removal of instrumental standing waves where required, followed by baseline subtraction with a low-order (≤2) polynomial in each sub-band. The fit to the baseline was then used to calculate the continuum level, compensating for the dual-sideband nature of the HIFI detectors i.e. the initial continuum level is the combination of emission from both the upper and lower sideband, which we assumed to be equal. Following this the WBS sub-bands were stitched into a continuous spectrum and all data were converted to the T_{MB} scale using efficiencies from Roelfsema et al. (2012). Finally, for ease of analysis all data were converted to FITS format and resampled to 0.3 km s^{-1} spectral resolution on the same velocity grid using bespoke PYTHON routines.

Comparison of the two polarisations for each source revealed insignificant differences, so these were co-added to reduce the noise. Comparison of peak and integrated intensities between the original WISH observations and those obtained as part of OT2_rvisser_2 for the same sources suggest that the calibration uncertainty is ≲10%. For the $2_{02}-1_{11}$ line for BHR71, the off-positions of the DBS mode coincided with outflow emission, resulting in a broad absorption. This is masked out during the analysis so does not impact the results for this source. In addition, as also noted for the $1_{10}-1_{01}$ transition by Kristensen et al. (2012), observations of the three Serpens sources sometimes show a weak narrow absorption feature at v_{LSR} = 1 km s^{-1} which probably arrises from emission in the reference position. This does not have any impact on the results derived below and so is ignored.

In five sources the $C^{18}O$ J = 10–9 line is detected in the line wing of the H_2O $3_{12}-3_{03}$ (1097 GHz) line. Before performing analysis on these data, we remove the $C^{18}O$ emission by subtracting a Gaussian with the same FWHM, line-centre and amplitude as obtained by San José-García et al. (2013).

As noted in Table 1, the more accurate SMA coordinates for IRAS 15398 were observed in two settings, H_2O $1_{11}-0_{00}$ and $H_2^{18}O$ $1_{10}-1_{01}$, as part of programme OT2_evandish_4. Comparison of these observations with the WISH observations is discussed in Appendix B.1. In the rest of this paper we will focus on the WISH observations as these include the most transitions observed towards the same position.

3. Results

This section begins with presentation of those results that can be obtained simply from the data themselves (Sect. 3.1). The profiles are then fitted with multiple Gaussian components, which are subsequently divided into different physically motivated categories based on their properties (Sect. 3.2).

Table 1. Source parameters.

Source	RA (h m s)	Dec (° ′ ″)	D^a (pc)	$v_{LSR}{}^b$ (km s^{-1})	$L_{bol}{}^c$ ($L_\odot$)	$T_{bol}{}^c$ (K)	$M_{env}{}^d$ ($M_\odot$)	$F_{CO}{}^e$ ($M_\odot$ yr^{-1} km s^{-1})
L1448-MM	03 25 38.9	+30 44 05.4	235	+5.2	9.0	46	3.9	3.7×10^{-3}
NGC 1333-IRAS2A	03 28 55.6	+31 14 37.1	235	+7.7	35.7	50	5.1	7.4×10^{-3}
NGC 1333-IRAS4A	03 29 10.5	+31 13 30.9	235	+7.2	9.1	33	5.2	2.1×10^{-3}
NGC 1333-IRAS4B	03 29 12.0	+31 13 08.1	235	+7.4	4.4	28	3.0	2.2×10^{-4}
L1527	04 39 53.9	+26 03 09.8	140	+5.9	1.9	44	0.9	4.4×10^{-4}
Ced110-IRS4	11 06 47.0	−77 22 32.4	125	+4.2	0.8	56	0.2	–
BHR71	12 01 36.3	−65 08 53.0	200	−4.4	14.8	44	3.1	–
IRAS 15398[f]	15 43 01.3	−34 09 15.0	130	+5.1	1.6	52	0.5	9.5×10^{-5}
L483	18 17 29.9	−04 39 39.5	200	+5.2	10.2	49	4.4	5.9×10^{-4}
Ser-SMM1	18 29 49.8	+01 15 20.5	415	+8.5	99.0	39	52.5	3.0×10^{-3}
Ser-SMM3	18 29 59.2	+01 14 00.3	415	+7.6	16.6	38	10.4	4.2×10^{-3}
Ser-SMM4	18 29 56.6	+01 13 15.1	415	+8.0	6.2	26	6.9	4.8×10^{-3}
L723	19 17 53.7	+19 12 20.0	300	+11.2	3.6	39	1.3	2.9×10^{-3}
B335	19 37 00.9	+07 34 09.6	250	+8.4	3.3	36	1.2	6.0×10^{-4}
L1157	20 39 06.3	+68 02 15.8	325	+2.6	4.7	46	1.5	3.7×10^{-3}
NGC 1333-IRAS3A	03 29 03.8	+31 16 04.0	235	+8.5	41.8	149	8.6	–
L1489	04 04 43.0	+26 18 57.0	140	+7.2	3.8	200	0.2	1.6×10^{-4}
L1551-IRS5	04 31 34.1	+18 08 05.0	140	+6.2	22.1	94	2.3	5.1×10^{-4}
TMR1[f]	04 39 13.7	+25 53 21.0	140	+6.3	3.8	133	0.2	2.5×10^{-5}
TMC1A[f]	04 39 34.9	+25 41 45.0	140	+6.6	2.7	118	0.3	1.3×10^{-4}
TMC1	04 41 12.4	+25 46 36.0	140	+5.2	0.9	101	0.2	4.5×10^{-4}
HH46-IRS	08 25 43.9	−51 00 36.0	450	+5.2	27.9	104	4.4	1.1×10^{-3}
IRAS 12496	12 53 17.2	−77 07 10.6	178	+3.1	35.4	569	0.8	–
GSS30-IRS1	16 26 21.4	−24 23 04.0	125	+3.5	13.9	142	0.6	5.2×10^{-4}
Elias 29	16 27 09.4	−24 37 19.6	125	+4.3	14.1	299	0.3	6.4×10^{-5}
Oph-IRS63	16 31 35.6	−24 01 29.6	125	+2.8	1.0	327	0.3	1.1×10^{-5}
RNO91	16 34 29.3	−15 47 01.4	125	+0.5	2.6	340	0.5	1.0×10^{-4}
RCrA-IRS5A	19 01 48.0	−36 57 21.6	130	+5.7	7.1	126	2.0	–
HH100-IRS	19 01 49.1	−36 58 16.0	130	+5.6	17.7	256	8.1	–

Notes. Sources above the horizontal line are Class 0, sources below are Class I. [(a)] Taken from van Dishoeck et al. (2011) with the exception of sources in Serpens, where we use the distance determined using VLBA observations by Dzib et al. (2010). [(b)] Obtained from ground-based $C^{18}O$ or $C^{17}O$ observations (Yıldiz et al. 2013) with the exception of IRAS4A for which the value from Kristensen et al. (2012) is more consistent with our data. [(c)] Measured using *Herschel* PACS data from the WISH and DIGIT key programmes (Karska et al. 2014). [(d)] Mass within the 10 K radius, determined by Kristensen et al. (2012) from DUSTY modelling of the sources. [(e)] Taken from Yıldiz et al. (2014) for CO 3–2. [(f)] The coordinates used in WISH; more accurate SMA coordinates of the sources are $15^h43^m02\overset{s}{.}2$, −34°09′06.″8 (IRAS 15398), $04^h39^m13\overset{s}{.}9$, +25°53′20.″6 (TMR1) and $04^h39^m35\overset{s}{.}2$, +25°41′44.″4 (TMC1A; Jørgensen et al. 2009). For IRAS 15398, these coordinates were observed in two settings as part of the OT2 programme OT2_evandish_4.

3.1. Line profiles

All H_2O spectra for three Class 0 and two Class I sources are shown in Fig. 2 as an example, with spectra for all WISH sources presented in Figs. A.1–A.6 for all H_2O transitions. The $H_2^{18}O$ spectra for sources with at least one detection are shown in Fig. A.7.

As can be seen in Fig. 2, the water line profiles are often broad and complex, with generally narrower emission towards Class I with respect to Class 0 sources. There is significant variation in line intensity and shape between different sources, which is not particularly surprising given the range the sample covers in terms of luminosity, envelope mass and outflow activity (see further discussion in Sect. 4.3).

The basic properties of the spectra; noise level in 0.3 km s^{-1} bins, peak brightness temperature, integrated intensity and full-width at zero intensity (FWZI), are tabulated for all sources and lines in Tables A.3–A.5.

The FWZI is measured on spectra resampled to 3 km s^{-1} to improve the signal-to-noise ratio (S/N). First, the furthest points from the source velocity that are above $2\sigma_{rms}$ of the resampled spectrum within a window around the line are found. The FWZI is then between the first channel moving away from the source velocity in each direction where the spectrum drops below $1\sigma_{rms}$. The integrated intensity is then calculated over the range identified by the FWZI. While this approach is more data than source driven, there is approximately a factor of 10 difference in the noise level between the deepest and shallowest spectra (see Table 2). Thus using an alternative definition of the FWZI based on a set fraction of the peak in a way that is consistent and comparable between the different transitions would require a high enough threshold that it would not reflect the broadness of the line wings. It could also be skewed in the lower excitation lines by the narrow emission and/or absorption at the source velocity (for example, see IRAS4B in Fig. 2).

Table 2 presents the detection statistics, median noise level, and the mean and median FWZI for all detections separated by the evolutionary stage of the source. For the Class 0 sources, BHR71 and L1448-MM are excluded because they have bullet

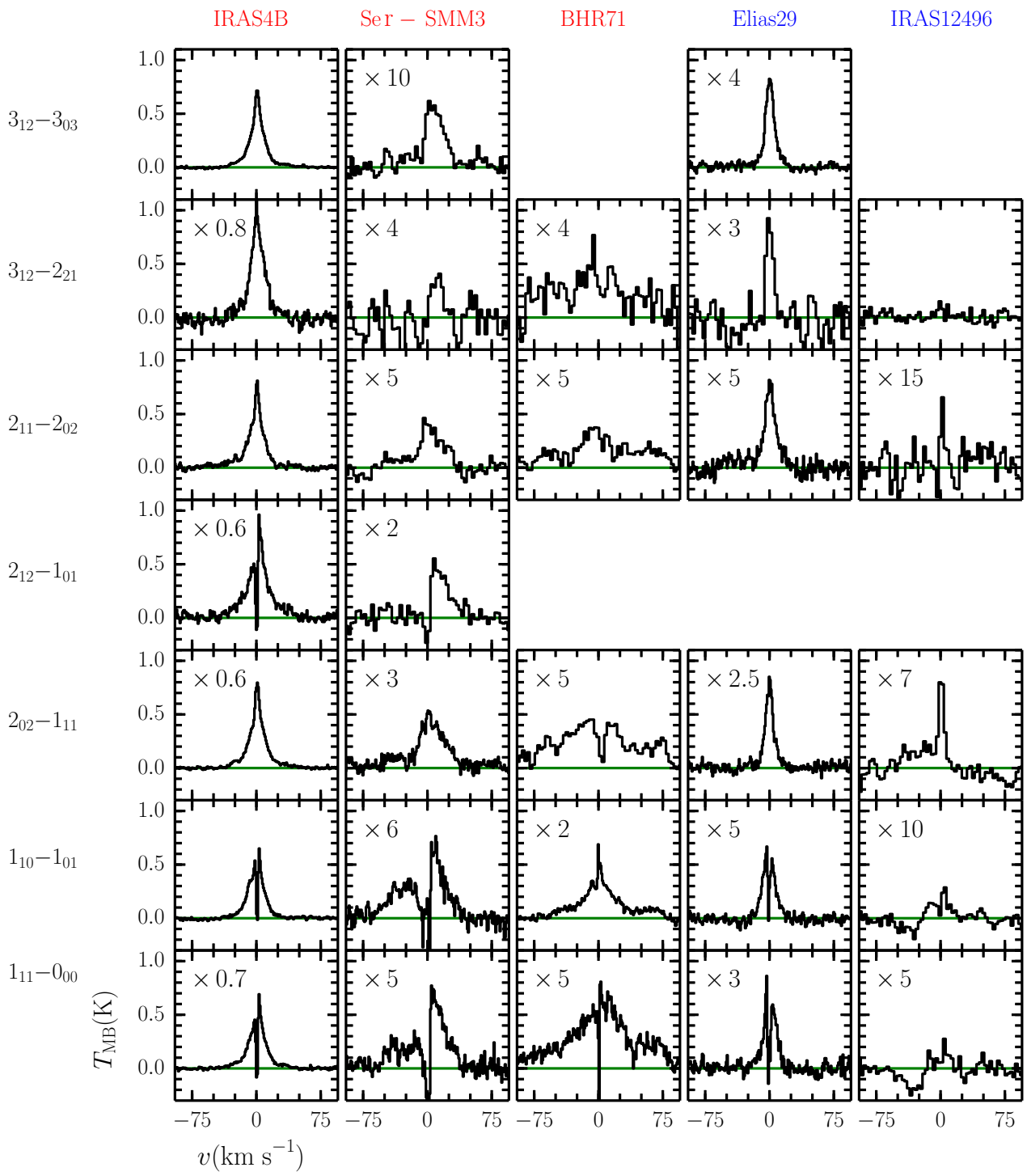

Fig. 2. Example H_2O spectra for three Class 0 and two Class I sources (names in red and blue respectively). All spectra have been recentred so that the source velocity is at 0 km s^{-1} and scaled by the number in the top-right corner of each panel. Some spectra have also been resampled to a lower velocity resolution for ease of comparison. The green line indicates the baseline.

emission (discussed further in Sect. 3.2.4) which significantly increases their FWZI compared to other sources but were not observed in all lines.

The average H_2O FWZIs (see Table 2) are remarkably similar for Class 0 sources. There is also little difference between the mean and median values, suggesting that these values are not dominated by a few sources and so are representative of general source properties. Given the order of magnitude difference between the highest and lowest sensitivity observations, this suggests that on average our observations have a high-enough sensitivity to detect the full extent of the line wings. While the Class I sources are fainter and so have a lower S/N, the transitions also look narrower, so it seems unlikely that higher sensitivity would increase their mean FWZI to the point where it was consistent with the Class 0 sources. Variation in line shape between transitions for a given source is relatively small, particularly in the line wings for the Class 0 sources. In a few cases the FWZI varies between the different transitions for a given source,

Table 2. Detection statistics, average noise and FWZI for each line and evolutionary stage.

Line	Class 0				Class I			
	D/O.[a]	$\overline{\sigma_{\rm rms}}$ (mK)	Mean FWZI (km s^{-1})	Median FWZI (km s^{-1})	D/O[a]	$\overline{\sigma_{\rm rms}}$ (mK)	Mean FWZI (km s^{-1})	Median FWZI (km s^{-1})
H_2O $1_{11}-0_{00}$	14/15	19	79 ± 32^b	82^b	7/11	24	47 ± 18	42
H_2O $1_{10}-1_{01}$	15/15	12	72 ± 32^b	69^b	12/14	10	50 ± 19	48
H_2O $2_{12}-1_{01}$	5/5	123	69 ± 13	63	0/0	–	–	–
H_2O $2_{02}-1_{11}$	14/15	22	75 ± 33^b	81^b	9/11	22	34 ± 13	34
H_2O $2_{11}-2_{02}$	12/15	20	65 ± 27^b	62^b	7/9	17	33 ± 15	33
H_2O $3_{12}-2_{21}$	7/15	105	58 ± 21^b	54^b	4/11	122	22 ± 5	22
H_2O $3_{12}-3_{03}$	8/8	17	81 ± 26^c	75^c	2/2	9	42^d	42^d
$H_2^{18}O$ $1_{11}-0_{00}$	1/15	18	16^d	16^d	0/11	26	–	–
$H_2^{18}O$ $1_{10}-1_{01}$	3/13	4	41 ± 8	45	0/1	4	–	–
$H_2^{18}O$ $2_{02}-1_{11}$	0/3	16	–	–	0/0	–	–	–
$H_2^{18}O$ $3_{12}-3_{03}$	2/8	14	12^d	12^d	1/2	8	33^d	33^d

Notes. [(a)] No. of sources with detections out of the total observed in each line. [(b)] Detections for BHR71 and L1448-MM excluded. [(c)] Detection for L1448-MM excluded, BHR71 not observed. [(d)] No standard deviation is given for detections in less than three sources.

but in all cases except Ser-SMM3 the results are due to variation in the noise level of the different spectra. The reason that Ser-SMM3 is likely still consistent with the general picture is discussed in Appendix B.2.

The FWZI for all $H_2^{18}O$ detections except the $3_{12}-3_{03}$ line towards Elias 29 are smaller than those for the corresponding $H_2^{16}O$ transition by a factor of 2–8. However, as shown in Fig. 3, the spectra are consistent within the noise. Thus the difference is most likely a S/N issue. Comparison of the integrated intensities assuming an isotopic $^{16}O/^{18}O$ ratio of 540 (Wilson & Rood 1994) results in an optical depth for the H_2O transitions of order 20–30 assuming that $H_2^{18}O$ is optically thin.

Only TMC1A and Oph-IRS63, both Class I sources, were not detected in any transition at the 3σ level (in 0.3 km s^{-1} bins). All sources detected in the $1_{10}-1_{01}$ line are also detected, where observed, in all other H_2O lines except the $3_{12}-2_{21}$ transition. The non-detections in this line are likely due to the higher noise in these data as it is generally sources that are fainter in the other lines that are not detected. This is also likely the reason for the non-detections in $H_2^{18}O$ as it is only the very brightest sources that are detected, and even then most have a peak signal-to-noise of less than 10. Of the 14 sources observed in the $H_2^{18}O$ $1_{10}-1_{01}$ transition, seven (BHR71, L1527, NGC 1333-IRAS2A, NGC 1333-IRAS4A, NGC 1333-IRAS4B, Ser-SMM1 and Ser-SMM4) have detections of the CH triplet at 536.76–536.80 GHz in emission in the other side-band. For NGC 1333-IRAS4A, this is confused with the $H_2^{18}O$ line, so the CH triplet is masked during the analysis. Analysis of the CH emission itself is beyond the scope of this paper.

The conclusion from the comparison of line profiles and FWZIs is therefore that the lower FWZI for the $H_2^{18}O$ transitions compared to the corresponding $H_2^{16}O$ line for a given source is just a S/N issue. However, the decrease in the average FWZI between Class 0 and I is real and not related to the sensitivity of the data.

3.2. Line components

3.2.1. Gaussian decomposition

As can be seen in Fig. 2, the water line profiles towards low-mass protostars are complex and generally not well reproduced by a single line shape, e.g. a single Gaussian, Lorentzian or triangular profile. However, as shown by Kristensen et al. (2010, 2012) they can be decomposed into multiple components, each relating to different parts of the protostellar system.

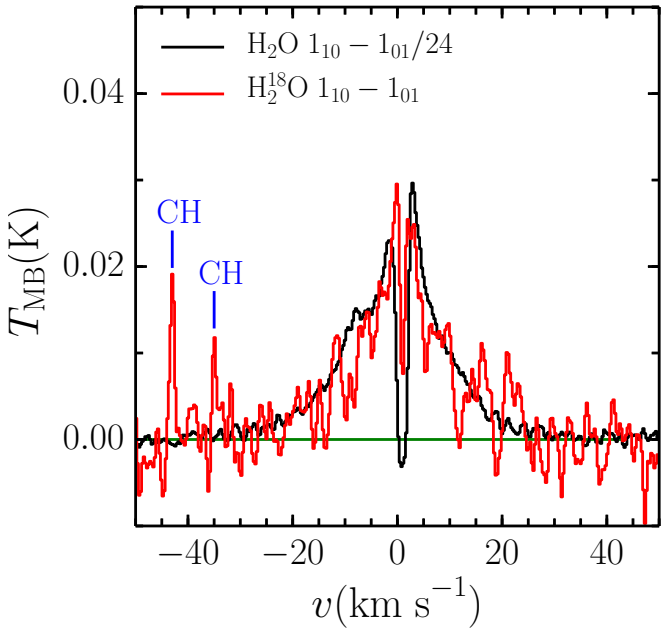

Fig. 3. Comparison of the H_2O (black) and $H_2^{18}O$ (red) $1_{10}-1_{01}$ spectra for IRAS4B where the H_2O spectrum has been scaled down such that the peak intensities are the same. The green line indicates the baseline. The blue lines indicate the approximate velocities of the CH transitions from the other sideband in the $H_2^{18}O$ observations. The third component of the CH triplet is just beyond the plotted range but is also detected.

In reality, the detailed shape of the emission from a given region will depend on both the physics and geometry, particularly for shocks, and so a range of line shapes may indeed be present (see e.g. Jiménez-Serra et al. 2008b). However, the observed H_2O line-shapes, particularly in high S/N data, appear Gaussian-like, so this is the most reasonable line-shape to assume. The reason that the emission from shocks is Gaussian-like may be due to our observations encompassing a number of shocks with a range of viewing angles. Alternatively, this may be the result of mixing and turbulence induced by Kelvin-Helmholtz instabilities along the cavity wall (see e.g. Bodo et al. 1994; Shadmehri & Downes 2008).

As discussed in Sect. 3.1, the width of the line profiles does not change significantly between the observed transitions, though the relative and absolute intensity of individual components does change. Therefore, while the physical conditions in the different regions within the protostar where water is emitting may be different, all transitions are probably emitting from the same parcels of gas in each case.

We therefore choose to require that the line centre and width of each Gaussian component are exactly the same for all transitions observed towards a given source, though the intensity of a given component can be different for each line. In practical terms, this is achieved by creating an array which contains all H_2O and $H_2^{18}O$ spectra for a given source and fitting a global function to this array which contains a number of Gaussians equal to the number of components multiplied by the number of transitions. For a given component, the line centre and width are common variables between the Gaussians applied to each transition. They are therefore constrained by all available data for a particular source, decreasing the uncertainties and improving the reliability of the fit, particularly in cases where the emission in some transitions is weak. For high S/N spectra, the difference between fitting each line separately and this global fitting approach is small, as shown in Fig. 2 of Kristensen et al. (2013). Those authors were able to use individual fits because they focused on the brightest Class 0 sources in the WISH sample and were interested in one relatively distinct component. Here we want to isolate and analyse all components in all sources, so a global fitting approach is preferred.

An example best-fit result is shown in Fig. 4 for BHR71, a source with a mix of low and high S/N spectra. For this source, the quiescent envelope component shows an inverse P-Cygni profile at full resolution and so is masked out from the fitting process. In other cases where only a simple emission or absorption profile from the envelope is observed, this is included in the Gaussian fit. For the $2_{02}-1_{11}$ transition the absorption is due to reference contamination and so is also masked from the fitting.

The fit results were obtained using the ordinary least-squares solver in the PYTHON module SCIPY.ODR[1] starting from an initial guess for a single Gaussian. The results and residuals of this fit were examined and the number of components increased or the initial guess modified to result in residuals below the rms. While this approach can be susceptible to finding local minima in some cases, particularly with very complex line profiles such as for BHR71, the combination of varying the initial guess and visual inspection of the residuals ensured that this returned reasonable results (e.g. combinations of large positive and negative Gaussians which mostly cancel out are excluded). In all cases the number of Gaussian components used was the minimum required for the residuals to be within the rms noise. The results of the Gaussian fitting for all sources are presented in Tables A.6 to A.10. Where a component is not detected in a given line, a 3σ upper limit is calculated from the noise in the spectrum. The results are consistent with those presented in previous papers (Kristensen et al. 2012, 2013; Mottram et al. 2013) taking into account the latest reduction and calibration.

Having identified these components, it is then a question of attempting to relate them to the different physical components of a protostellar system. In previous work (Kristensen et al. 2010, 2012; San José-García et al. 2013; Yıldız et al. 2013) the different components have been established and named based primarily on their line-width. However, this is a rather phenomenological convention and does not always allow for clear distinction between different excitation conditions, as also noted in Kristensen et al. (2013). We therefore prefer to use terms which indicate the most likely physical origin of the emission component (cf. van der Tak et al. 2013, for similar terminology applied to high-mass protostars). Table 3 provides a summary of how these new terms are related to those used in previous papers on low-mass protostars in order to ensure continuity.

The different components for each source are divided into three categories: envelope, cavity shock and spot shock, building on the work of Kristensen et al. (2012, 2013), with the first

[1] http://scipy.org/

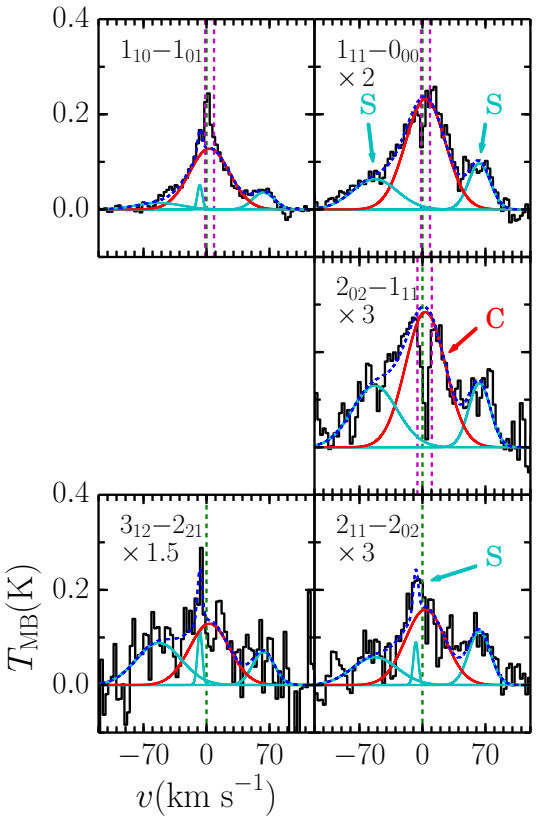

Fig. 4. Continuum subtracted WBS spectra for BHR71 (black) resampled to 3 km s^{-1}. The red and cyan lines show the individual Gaussian components for the cavity shock (C) and spot shocks (S) respectively (see text and Table 3 for details) while the blue dashed line shows the combined fit for each line. All spectra have been shifted so that the source velocity is at 0 km s^{-1}, which is indicated by the green dashed lines. At full resolution the quiescent envelope component has an inverse P-cygni profile (see Mottram et al. 2013) and so is masked (indicated by the magenta dashed lines) rather than being fit by multiple components during the Gaussian fitting. The broad absorption in the $2_{02}-1_{11}$ transition (*middle left panel*) is caused by reference contamination and is also masked during the fitting process.

Table 3. Component terminology.

This paper[a]	Previous papers	References
Envelope	Narrow	1
Cavity shock	Broad or medium	1
Spot shock	Bullet or EHV, also offset or medium if broad also present	1, 2

Notes. [(a)] See Sects. 3.2.2–3.2.4 and Fig. 6 for criteria.

References. (1) Kristensen et al. (2012); (2) Kristensen et al. (2013).

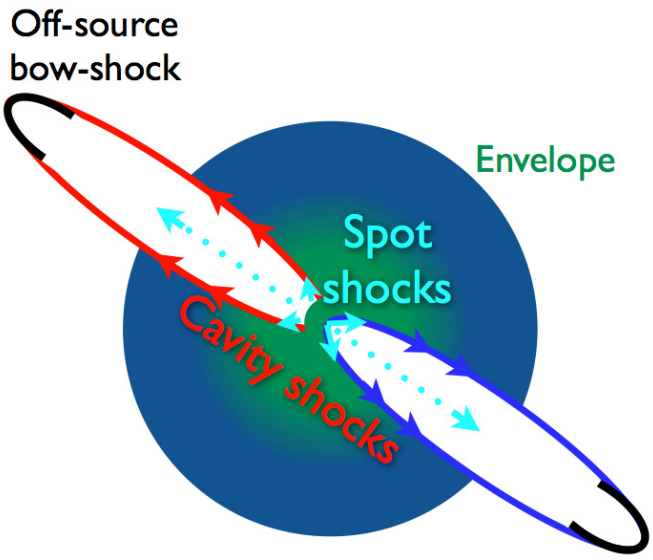

Fig. 5. Cartoon showing the proposed origin of the various distinct kinematic gas components observed in low-J water line profiles.

letter of each term being used to identify them in Tables A.6 to A.10. The following subsections (Sect. 3.2.2–3.2.4) will discuss and motivate the definition of each of these components in turn, with Fig. 5 indicating their expected physical location in a protostellar system. Following this, a summary and comparison showing how the kinematic properties of the different components relate to each other will be presented to verify that they are distinct (Sect. 3.2.5).

3.2.2. Envelope

Emission from the quiescent envelope is characterised by small FWHM and offset from the source velocity, thus we assign this designation to the component with the smallest FWHM for each source which has $FWHM \leq 5$ km s^{-1} and offset $\leq$2 km s^{-1}. This can be in absorption in the ground-state lines, particularly for Class 0 sources, and even saturated where all line and continuum photons are absorbed. One confirmation that this emission and absorption comes from the envelope is that the line centres and widths are similar to those observed in C^{18}O towards these sources (San José-García et al. 2013). No sources show distinct foreground absorptions offset from the source velocity, unlike HIFI spectra towards high-mass protostars (e.g. van der Tak et al. 2013), primarily due to the much smaller distances to our sources. Thus most of the absorption likely comes from the protostars own envelope. Given that the sub-mm continuum and line emission from the envelope is centrally condensed (Jørgensen et al. 2007; Kristensen et al. 2012; Mottram et al. 2013) we assume that the emission scales as a point-source.

While many sources also show envelope emission, it is often non-Gaussian in shape in the ground-state lines, consisting of combinations of emission and absorption in either inverse or regular P-Cygni profiles which are indicative of infall and expansion respectively. This was characterised in the $1_{10}-1_{01}$ (557 GHz) line by Kristensen et al. (2012), and the cases showing infall profiles were analysed in more detail by Mottram et al. (2013). In these cases, the combination of envelope emission and absorption is not a single Gaussian and so the relevant parts of the spectra are masked during the fitting process (e.g. see Fig. 4).

Absorption from the envelope is also observed in the $H_2^{18}O$ $1_{11}-0_{00}$ and $1_{10}-1_{01}$ lines towards SMM1, which is consistent with the envelope of this source being particularly massive and having a relatively shallow density power-law slope (cf. Kristensen et al. 2012). The only source to show emission from the envelope in any $H_2^{18}O$ transitions is IRAS2A, where the tentative detections in the $H_2^{18}O$ $3_{12}-3_{03}$ and $2_{02}-1_{11}$ lines are the narrowest for any source and offset from the main outflow emission detected in the $H_2^{16}O$ transitions. This emission is likely related to the hot core where $T_{\rm dust} > 100$ K (see Visser et al. 2013, for more details) and originates on arcsecond scales based on interferometric observations (Persson et al. 2012, 2014). We do not study the envelope emission further in this paper. Further analysis of other sources showing absorption in the ground-state water lines, including the link with water ice, will be presented in Schmalzl et al. (2014).

3.2.3. Cavity shock

Having identified any envelope contribution, we designate the remaining component which is not in absorption in any line and has the smallest ratio of offset to FWHM as the cavity shock component. This is an empirical determination based on the assumption that the average velocity offset of the currently shocked gas in the outflow cavity is lower than for more discrete and energetic shocks and that it should not be in absorption against the continuum because the emission is most likely formed on larger scales. The offset of this component is always less than 15 km s^{-1} and decreases with smaller FWHM. That this component is Gaussian in shape, combined with the small offset compared to the FWHM, suggests that we are detecting both the red and blue-shifted lobes of the outflow cavity.

Water emission is elongated along the direction of the outflow (e.g. Nisini et al. 2010; Santangelo et al. 2012) with the dominant extended component having similar velocity distributions (e.g. Santangelo et al. 2014) as this component. As cavity shocks also dominate the on-source line profiles, we assume that it is elongated along the outflow direction but does not fill the beam parallel to the outflow axis, as in the spectrally unresolved PACS H_2O observations.

This component should not be confused with the entrained outflow material typically probed by low-J CO observations, as H_2O and low-J CO emission are not spatially coincident (e.g. Nisini et al. 2010; Santangelo et al. 2013). A detailed comparison between CO $J = 3-2$ and H_2O $1_{10}-1_{01}$ was presented in Kristensen et al. (2012) with the clear conclusion that these two transitions do not trace the same material. One of the main reasons is the enormous difference in critical density between these two transitions (10^4 cm^{-3} and 10^7 cm^{-3} respectively). As the gas is heated and compressed in the cavity shocks, the water abundance increases dramatically through both gas-phase synthesis and ice sputtering. During this warm and dense phase, water is one of the dominant coolants. However, as the gas cools and expands to come into pressure equilibrium with its surroundings, water excitation becomes highly inefficient due to high critical densities so little water emission originates from the cold entrained low-density outflow. Therefore, the non-coincidence of water and low-J CO is consistent with the expectation that water is significantly depleted under the typical conditions in the entrained outflowing gas.

Most detections in the $H_2^{18}O$ observations are associated with the cavity shock component, with the exception of IRAS2A as discussed above and IRAS4A, which is discussed in more detail in Appendix B.3.

3.2.4. Spot shock

All remaining components which show larger offset/FWHM are designated as spot shock components. The separation of the cavity and spot shock components is necessary because the line profiles show separate and distinct kinematic components (e.g. see Fig. 4), suggesting that they come from different shocks within the protostellar system. The use of offset/FWHM is also chosen so as to separate the component most likely associated with C-type shocks (cavity shock), where emission is centred at the source velocity, with components more likely associated with *J*-type shocks (spot shock), where emission is shifted away from the source velocity to the shock velocity relative to the line of sight (see e.g. Hollenbach 1997).

Some spot shock components are significantly offset from the source velocity, such that they are characteristic of "bullet" emission with large offsets (>20 km s^{-1}) from the source velocity and large FWHM (also >20 km s^{-1}, e.g. see Fig. 4). These are most likely associated with *J*-type shocks along the jet, as they have similar kinematic properties to EHV bullet emission in CO and SiO which is spatially located in knots along the jet axis (e.g. Bachiller et al. 1990, 1991; Hirano et al. 2006; Santiago-García et al. 2009).

The spot shock emission with lower velocity offset may originate in *J*-type shocks near the base of the outflow where the wind first impacts the envelope or outflow cavity, as first suggested by Kristensen et al. (2013). Those authors based this conclusion on: (i) some of the spot shock components detected in water line profiles are seen in absorption against the continuum but not the outflow; (ii) when detected in OH^+ and CH^+, the components are always in absorption against the continuum with no emission component and no outflow component. These two pieces of evidence point to an origin in front of the continuum and behind the outflow. In both cases, the velocity offset strongly suggests that the components are associated with *J*-type shocks (e.g. Hollenbach 1997).

As already noted by Kristensen et al. (2013) for NGC 1333-IRAS3A and Ser-SMM3, a few sources show spot shock components in absorption. These components are too offset and/or broad to be consistent with absorption due to the envelope or foreground clouds. In addition, they are present in excited transitions which makes a foreground origin highly unlikely. Off-position contamination can also be excluded due to the offset from the source velocity and that the $1_{10}-1_{01}$ position-switched observations share reference positions with other sources which do not show these components. The depth of these absorption features are consistent with absorption against the continuum only, suggesting that they originate between the observer and the continuum source, but not between the observer and the outflow emission.

We do not separate the "bullet" and less offset spot shocks into separate categories because the inclination of the shock relative to the line of sight plays a role in how offset a component is. However, in the cases where the offset from the source velocity is small, the spot shock components are always narrower than the cavity shock.

The suggested physical location of the spot shocks, whether in the jet or at the base of the outflow, is indicated in Fig. 5. Bullets are observed to be small (few arcseconds) and point-like knots in interferometric observations (e.g. Hirano et al. 2006; Santiago-García et al. 2009) and the analysis of Kristensen et al. (2013) suggests that the non-bullet spot shocks originate from very small regions (~100 AU) near the central protostar. This is also supported by the strong similarity in line shape between the spot shock component observed in water for IRAS2A and the compact (~1″) emission seen in SiO and SO towards MM3 in recent interferometry observations by Codella et al. (2014). A point-like geometry is therefore the most appropriate assumption for the spot shock component.

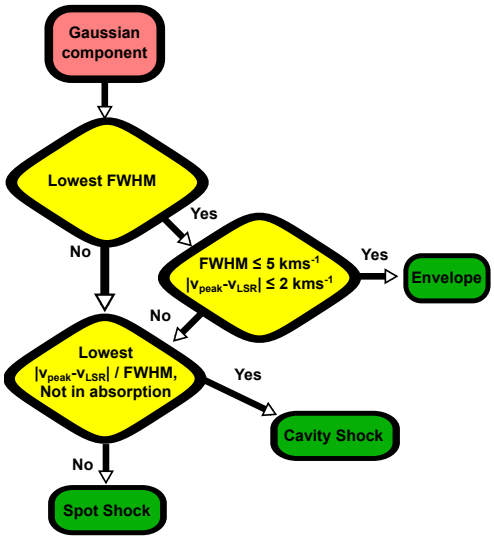

Fig. 6. Flow diagram for component type determination. $|v_{\rm peak} - v_{\rm LSR}|$ is the offset of the component centre from the source velocity.

3.2.5. Comparison of components

A summary of the overall classification scheme for the various components is shown in Fig. 6. Figure 7 then shows the relationship between FWHM and both velocity offset and the intensity in the $2_{02}-1_{11}$ (988 GHz) transition for the various components scaled to the typical distance for the sample of 200 pc. As most of the outflows from these sources are larger than the *Herschel* beam along the outflow axis (see Yıldiz et al. 2014), the intensity of the cavity shock component was corrected using a linear scaling, i.e. assuming that the emission fills the beam in one direction and is point-like perpendicular to it ($I_{\rm obs}\,(d/200)^1$). The spot shock and quiescent envelope components are assumed to be point-like ($I_{\rm obs}\,(d/200)^2$).

Though there are a few exceptions, the different components generally lie in distinct regions of the FWHM vs. offset parameter space, supporting the idea that they are formed under different conditions. In particular, the cavity shock and spot shock components are relatively well separated. The regions of FWHM vs. offset covered by the different components for the Class 0 and I sources are also similar.

The spot shock component which lies in the middle of the cluster cavity shocks in the Class 0 FWHM vs. offset plot is the broader of the two spot shocks towards NGC 1333-IRAS4A, marked with a black arrow in Fig. 7. This is likely related to bow-shocks which lie within the HIFI beam for the lower-frequency transitions (see Appendix B.3 for more details).

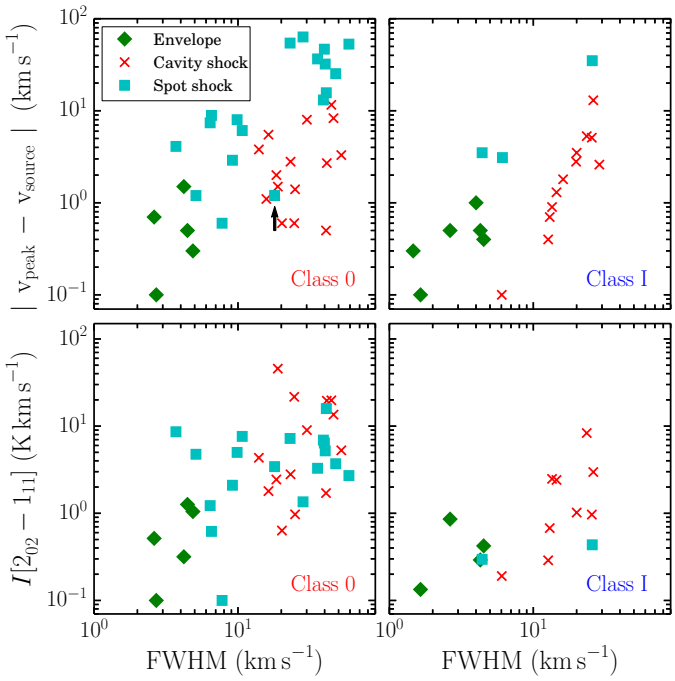

Fig. 7. Scatter plots of FWHM vs. offset of the peak from the source velocity (*top*) and intensity in the $2_{02}-1_{11}$ line corrected to a common distance of 200 pc (*bottom*) for the Gaussian components for Class 0 (*left*) and I (*right*) sources. When scaling the intensities, a linear scaling was used for the cavity shock components while a point-source scaling was used for the spot shock and envelope components. The black arrow indicates the broader of the two shock spots towards NGC 1333-IRAS4A which is discussed further in Appendix B.3.

In general, the intensity of the components in the Class I sources is lower than for the Class 0s. Table 4 shows the number of Class 0 and I sources in which the cavity shock and spot shock components are detected for each transition, as well as the mean and standard deviation in the fractional intensity in each component with respect to the total observed intensity. For the quiescent envelope component as this can sometimes include both absorption and emission, this was calculated by subtracting the intensity of the other detected components from the total observed intensity, but may include emission and absorption which cancel each other out. Absorptions in some components can lead to other components having larger intensities than the total.

While there is significant overlap in the intensity of components in the lower panels of Fig. 7, the results in Table 4 show that for a given source, the cavity shock dominates all the lines observed with HIFI, consisting of between 70 and 100% of the integrated emission. The spot shocks contribute ~20% for Class 0 sources and are on average negligible for Class I sources. The detection fraction of spot shocks is also much lower for Class I sources. The quiescent envelope does not have a strong contribution in the excited lines for Class 0 sources, though it can reduce the integrated intensity in the ground-state lines by up to 20% depending on the balance of emission and absorption. It plays a more significant role in Class I sources, contributing up to 30% of the total intensity.

4. Analysis

In this section we present analysis building on the results from the previous section. Discussion of the wider implication of the results and analysis, including comparison with other results in the literature, will be presented in Sect. 5.

4.1. Integrated intensity ratios

A first step in studying the excitation and physical conditions of the water-emitting gas in young protostars is to understand the opacity of the observed transitions, for which there are four regimes. Below a certain N_{H_2O}, a given transition will be optically thin while at high column density it will be optically thick. Both of these cases can be either in local thermodynamical equilibrium (LTE), when n_{H_2} is above the critical density for that transition, or sub-thermally excited if $n_{H_2} \ll n_{crit}$. As water has large Einstein A coefficients and high critical densities, there is a significant part of realistic parameter space that is optically thick but sub-thermally excited. In this regime, the lines are said to be effectively thin because the chance of collisional de-excitation is low, so photons effectively scatter within the region and will all eventually escape the $\tau = 1$ surface. As such, the intensity still scales as $N_{H_2O} \times n_{H_2}$ as in the optically thin sub-critical case (see e.g. Linke et al. 1977) even though $\tau > 1$.

As discussed in Sect. 3.1, for those few sources and transitions where we can obtain $H_2O/H_2^{18}O$ ratios, these suggest that those components detected in $H_2^{18}O$ are optically thick in those transitions. However, the number of lines, components and sources where this is the case is small. For sources or components for which $H_2^{18}O$ data are not available or detected, we can also use the ratios of the integrated intensity of the different components in pairs of $H_2^{16}O$ lines which share a common level. In the limit where both lines are optically thin, in LTE and have the same beam size, following Goldsmith & Langer (1999), the line ratio becomes:

$$\frac{I_1}{I_2} = \frac{g_{u1}A_{ul1}}{g_{u2}A_{ul2}}\frac{\nu_2^2}{\nu_1^2}\, e^{(E_{u2}-E_{u1})/k_b T_{ex}}, \quad (1)$$

where, for each transition, g_{u1} is the statistical weight of the upper level, A_{ul} is the Einstein A coefficient between the two levels, ν is the frequency, E_u is the upper level energy and T_{ex} is the excitation temperature. Alternatively, if both lines are optically thick, in LTE and have the same beam size the line ratio is given by:

$$\frac{I_1}{I_2} = \frac{\nu_1}{\nu_2}\frac{(e^{h\nu_2/k_b T_{ex}} - 1)}{(e^{h\nu_1/k_b T_{ex}} - 1)}. \quad (2)$$

If one line is optically thick but the other is optically thin, and/or if the transitions are sub-thermally excited, then the line ratio can take a range of values depending on the excitation conditions of the gas.

Figure 8 shows such a comparison, covering the middle and upper excitation range probed by the water transitions accessible to HIFI. The intensity ratios for all components detected in both lines are consistent with or close to the limit where all lines are optically thick. The optically thin limits have been calculated for each ratio assuming excitation temperatures of 100, 300 and 500 K, to show that the temperature variation of this limit does not impact the result of this simple analysis. For the $3_{12}-3_{03}/3_{12}-2_{21}$ ratio, the lines come from the same upper energy level, so the optically thin LTE ratio is not sensitive to temperature. What is more, a search of a wide parameter space using the non-LTE molecular line radiative transfer code RADEX (van der Tak et al. 2007, discussed in more detail in Sect. 4.4) no non-LTE optically thin solutions where the $3_{12}-3_{03}/3_{12}-2_{21}$ is

Table 4. Detection statistics and average fraction of the total intensity that each component contributes for each transition.

Line	Class 0						Class I					
	Envelope[a]		Cavity shock		Spot shock		Envelope[a]		Cavity shock		Spot shock	
	D^b	I_{comp}/I_{tot}	D^b	I_{comp}/I_{tot}	D^b	I_{comp}/I_{tot}	D^b	I_{comp}/I_{tot}	D^b	I_{comp}/I_{tot}	D^b	I_{comp}/I_{tot}
H_2O $1_{11}-0_{00}$	14	0.0 ± 0.1	14	0.8 ± 0.1	9	0.3 ± 0.1	4	-0.1 ± 0.1	4	1.1 ± 0.1	0	–
H_2O $1_{10}-1_{01}$	15	0.0 ± 0.1	15	0.8 ± 0.1	8	0.2 ± 0.1	12	0.1 ± 0.1	11	1.1 ± 0.3	3	-0.2 ± 0.2
H_2O $2_{12}-1_{01}$	5	0.1 ± 0.2	5	0.6 ± 0.1	5	0.2 ± 0.2	–	–	–	–	–	–
H_2O $2_{02}-1_{11}$	14	0.1 ± 0.1	14	0.6 ± 0.1	10	0.3 ± 0.1	8	0.2 ± 0.1	7	0.8 ± 0.1	1	0.0 ± 0.0
H_2O $2_{11}-2_{02}$	11	0.2 ± 0.1	11	0.6 ± 0.1	8	0.2 ± 0.1	7	0.3 ± 0.2	5	0.7 ± 0.2	0	–
H_2O $3_{12}-2_{21}$	7	0.2 ± 0.1	7	0.6 ± 0.1	5	0.2 ± 0.1	3	0.0 ± 0.1	3	1.0 ± 0.1	0	–
H_2O $3_{12}-3_{03}$	8	0.2 ± 0.1	8	0.5 ± 0.1	7	0.2 ± 0.1	2	-0.3 ± 0.2	2	1.3 ± 0.2	0	–

Notes. [a] Calculated for all sources with detected emission as $I_{tot} - I_{outflow} - I_{shock} - I_{bullet}$. May include emission and absorption. [b] No. of sources with detections in this component.

Table 5. Average H_2O line ratios.

Transitions	D^a		Observed ratio[b]		Thin LTE[c]	Thick LTE[c]	θ_1/θ_2[d]
	C[e]	S[f]	C[e]	S[f]			
$1_{10}-1_{01}/2_{12}-1_{01}$	5	4	0.43 ± 0.06	0.58 ± 0.17	0.40	1.10	3.00
$3_{12}-3_{03}/3_{12}-2_{21}$	8	5	0.61 ± 0.04	0.62 ± 0.19	6.91	1.00	1.05
$1_{11}-0_{00}/2_{02}-1_{11}$	19	13	1.02 ± 0.05	1.02 ± 0.07	0.04	0.99	0.89
$1_{10}-1_{01}/2_{02}-1_{11}$	20	12	0.79 ± 0.07	0.73 ± 0.11	0.26	3.11	1.77
$2_{12}-1_{01}/2_{02}-1_{11}$	5	4	1.50 ± 0.12	1.15 ± 0.28	0.65	2.84	0.59
$2_{11}-2_{02}/2_{02}-1_{11}$	15	11	0.57 ± 0.04	0.58 ± 0.05	0.04	1.02	1.31
$3_{12}-2_{21}/2_{02}-1_{11}$	10	7	1.04 ± 0.09	0.99 ± 0.17	0.06	2.96	0.86
$3_{12}-3_{03}/2_{02}-1_{11}$	10	8	0.52 ± 0.04	0.50 ± 0.05	0.39	2.97	0.90

Notes. [a] Number of components with detections. [b] Mean and standard error on the mean. Not corrected for beam size. [c] Calculated for T_{ex} = 300 K and an ortho-to-para ratio of 3. [d] Beam size ratio. [e] Cavity shock component. [f] Spot shock component.

below 1. We can therefore exclude both the LTE and sub-thermal optically thin regimes for these transitions.

Table 5 shows the line ratios and the standard error on the mean averaged separately for cavity and spot shock components for the transitions which share a common energy level, as well as all lines relative to the $2_{02}-1_{11}$ line. The optically thick and optically thin limits are also provided, assuming an excitation temperature of 300 K and an ortho-to-para ratio of 3. We do not present average ratios including the $H_2^{18}O$ transitions because there are so few detections that these may not be a fair comparison. The line ratios have not been corrected for the different beam-sizes of each transition, but for many ratios the difference in beam-size is small. Correction for a point source emitting region is $(\theta_1/\theta_2)^2$, for a cylindrical emitting region which fills the beam in one axis is $(\theta_1/\theta_2)^1$ and is 1 for an emitting region which fills both beams.

For all ratios except the $1_{10}-1_{01}/2_{12}-1_{01}$ we can rule out the optically thin LTE solution. Many of the ratios are close to the optically thick LTE limit, but there are a few notable exceptions (e.g. $3_{12}-3_{03}/2_{02}-1_{11}$). The average $1_{10}-1_{01}/2_{12}-1_{01}$ ratio lies close to the optically thin limit, but this has the largest difference in beam size and the emitting regions are unlikely to fill the beam (discussed further in Sect. 4.4). Given that the ratios of each of these transitions with the $2_{02}-1_{11}$ line are not in the optically thin LTE limit, we can therefore exclude this solution for all observed lines.

Comparing the two component types, most line ratios are the same. However, those including the $1_{10}-1_{01}$ and $2_{12}-1_{01}$ transitions, which have the largest difference in beam size from the other lines, are slightly different. Given the similarity of the other line ratios, this probably indicates a difference in emitting area shape between the two component types rather than a large difference in excitation conditions.

4.2. Line ratios as a function of velocity

The intensity ratios suggest that at least some of the observed transitions are optically thick. Therefore, the next thing to consider is whether this holds for the whole line or just near the peak of the emission and whether we can distinguish between the LTE and sub-thermally excited regimes. This can be explored using the ratio of the observed water lines as a function of velocity. The top panel of Fig. 9 shows $3_{12}-3_{03}/3_{12}-2_{21}$ where both lines have intensities above 3σ after being resampled to 1 km s^{-1} bins, averaged over all sources and both red and blue line wings. The standard deviation between the sources, shown by the grey region, is similar to the uncertainties in a single source, and the ratios are consistent with being constant as a function of velocity. The bottom panel of Fig. 9 shows the same line ratio as the top panel, but separately for the red and blue wings of NGC 1333-IRAS4A. The line ratio does not change significantly between different line components, a result which is not unique to this source except in a few cases where quiescent envelope emission causes a change in the ratio near the source velocity.

The middle panels of Fig. 9 show the $1_{10}-1_{01}/2_{12}-1_{01}$ and $1_{10}-1_{01}/3_{12}-3_{03}$ ratios, with the former having the largest difference in beam size and is the only ratio to show significant variation as a function of velocity, of order a factor of two. That the $1_{10}-1_{01}/3_{12}-3_{03}$ ratio is constant with velocity suggests that

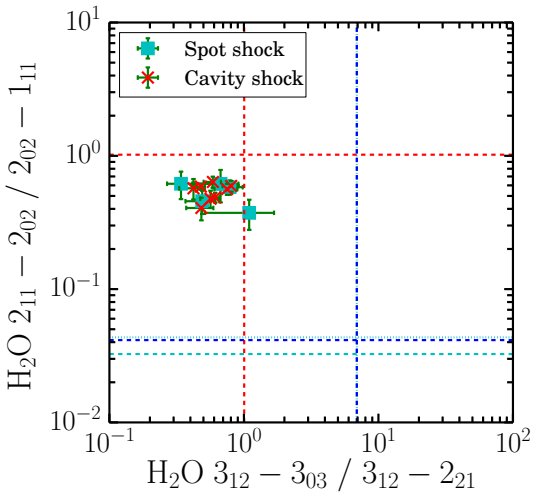

Fig. 8. Line ratio vs. line ratio plot. The red dashed lines indicate the limits in which both lines are in LTE and optically thick. The blue dashed, cyan dashed and cyan dotted lines indicate the limits in which both lines are in LTE and optically thin for excitation temperatures of 300, 100 and 500 K respectively. For the *x*-axis, since the lines share their upper energy level then the ratio is not sensitive to temperature and the optically thin lines lie on top of each other. Observed ratios not on either line indicate either subthermal excitation and/or that one transition is optically thick while the other is optically thin. In both cases, the ratio is then dependant on the excitation conditions of the gas.

this variation may be due to a variation in emitting region shape or position as a function of velocity. Indeed, it may be that some of the emission encompassed by all the other beams is on the edge of or outside the $2_{12}-1_{01}$ beam, which is the smallest of all the observations. This certainly seems to be the case for one of the spot-shock components of NGC 1333-IRAS4A which is not detected in this line and whose intensity increases with the beam-size of the transition (see Appendix B.3).

The $2_{12}-1_{01}$ line aside, the constant line-ratios as a function of velocity suggest that the excitation conditions present hold for all velocities. This is also consistent with the H_2O and $H_2^{18}O$ lines having the same shape (cf. Fig. 3). The ratios do not vary from low to high velocity in contrast to low and high-J CO line ratios (San José-García et al. 2013; Yıldiz et al. 2013), where the line-shape varies with J. This is likely caused in part by the low-J CO lines being optically thick in LTE at low velocities with τ decreasing with increasing offset. Thus, CO emission from inside the $\tau = 1$ surface is suppressed, with that surface varying with velocity and J. That this does not seem to be the case for H_2O, due to the invariant line ratio with velocity, suggests that the lines are not in the optically thick LTE solution even at low velocity. Combined with the previous analysis on the integrated intensity ratios, this suggests that the observed transitions are most likely optically thick but effectively thin, i.e. sub-thermally excited.

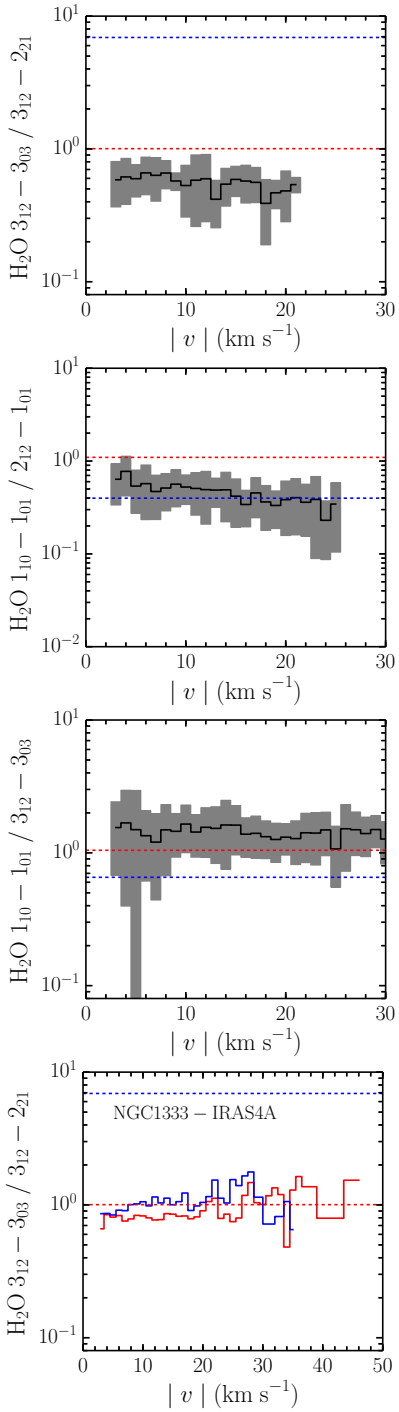

Fig. 9. *Top and middle*: line intensity ratio as a function of velocity averaged over all sources with intensities in both lines above 3σ after resampling to 1 km s^{-1} bins (black). The grey region indicates the standard deviation of the sources, which is of similar magnitude to the uncertainty in the ratio for a given source. *Bottom*: line ratio for the red and blue wings of the Class 0 source NGC 1333-IRAS4A. In all panels, the red and blue dashed lines indicate the limits in which both lines are in LTE and optically thick or optically thin respectively for an excitation temperatures of 300 K.

4.3. Correlations

Correlation plots comparing source properties (see Table 1) for all cavity shock components with $T_{\rm peak}$ corrected to a common distance of 200 pc for the $2_{02}-1_{11}$ transition assuming a linear correction (top), and with the FWHM (bottom) are shown in Fig. 10. There is a correlation of $M_{\rm envl}$ with the peak brightness temperature of the cavity shock component (3.5σ[2]), but not with FWHM. There is a correlation between the H_2 density at

[2] The significance of a Pearson correlation coefficient p for sample size n is given in terms of σ as $|\ p\ |\ \sqrt{n-1}$ (Marseille et al. 2010).

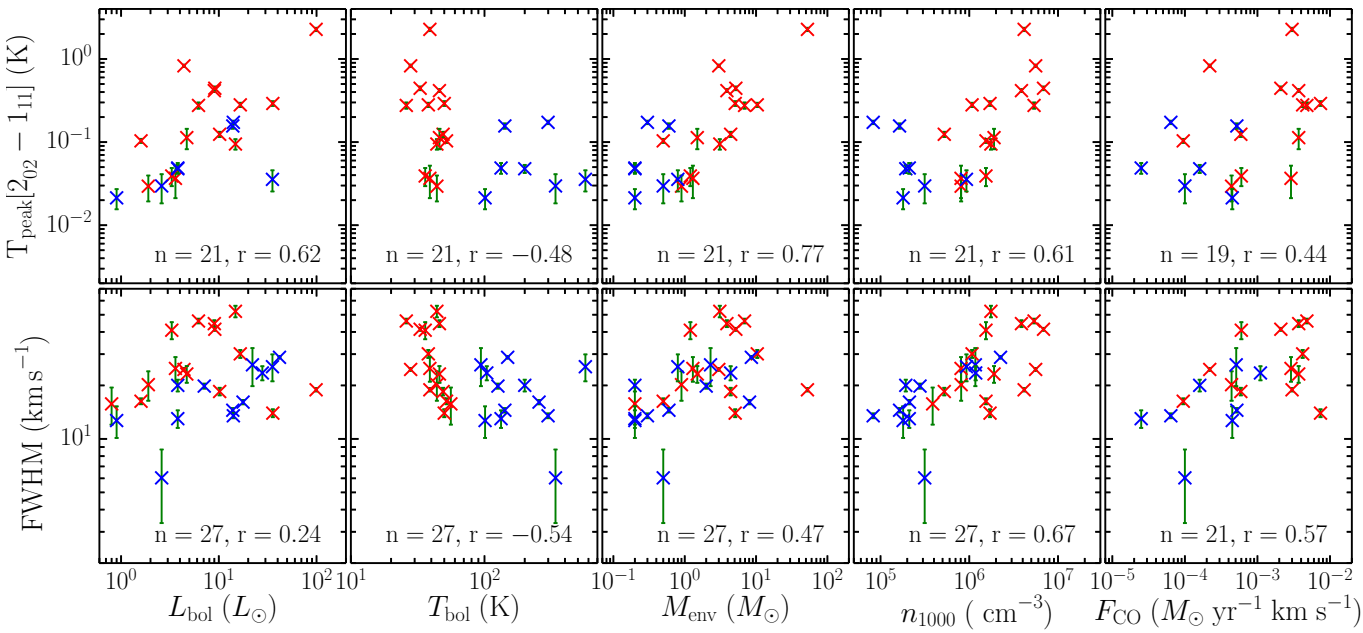

Fig. 10. Correlation plots of T_{peak} for the $2_{02}-1_{11}$ line corrected to a common distance of 200 pc assuming a linear scaling (*top*) and FWHM (*bottom*) of the cavity shock component vs., from *left to right*, L_{bol}, T_{bol}, M_{env}, n_{1000} and F_{CO} as presented in Table 1. Class 0 and I sources are coloured red and blue respectively. The number of sources and Pearson correlation coefficient are given at the *bottom* of each panel.

1000 AU (n_{1000}) as obtained from the DUSTY continuum models of Kristensen et al. (2012) and FWHM, and a weaker trend with T_{peak} (3.4 and 2.7σ respectively). There is also a weak trend between T_{peak} and L_{bol} (2.8σ) and a weak negative trend between T_{bol} and FWHM (2.7σ). Finally, there is no correlation or trend between F_{CO} and T_{peak}, but there is a weak trend with FWHM (2.5σ).

The different behaviour of T_{peak} and FWHM explains why Kristensen et al. (2012) did not see correlations or trends between some of these properties and the integrated intensity of the $1_{10}-1_{01}$ line. The integrated intensity is effectively a multiplication of these two separate quantities which, as shown in Fig. 10, have different behaviours, particularly with F_{CO}. More sources are needed to confirm some of the weaker trends. The implications of these results will be discussed in Sect. 5.

4.4. Excitation conditions

4.4.1. Method

In order to constrain the excitation conditions (e.g. n_{H_2}, N_{H_2O}, T) under which water is excited in the cavity and spot shock components, a series of calculations were run using RADEX. This assumes that the various transitions of a given species have the same line width, as imposed during the Gaussian fitting, and returns the integrated intensity and optical depth for each transition for a given H_2 volume density, molecule column density and temperature. We assume plane-parallel geometry, that the ortho-to-para ratios of H_2O and H_2 are both in the high-temperature limit of 3, a $H_2O/H_2^{18}O$ ratio of 540 (Wilson & Rood 1994), and use the latest collisional rate coefficients from Daniel et al. (2011) and Dubernet et al. (2009) and molecular spectroscopy from the Cologne Database for Molecular Spectroscopy (CDMS Müller et al. 2005) as collected from the Leiden Atomic and Molecular Database (LAMDA[3] Schöier et al. 2005). Even if the pre-shock ortho-to-para ratio for H_2 is as low as 10^{-3}, as can be the case in the cold envelope (e.g. Pagani et al. 2009), shocks which are fast enough to sputter water from the grains are also efficient at ortho-to-para conversion of H_2 (Kristensen et al. 2007). A value of 3 is therefore not unreasonable even for shocks in pristine envelope material.

Grids of RADEX models were run both for the average line ratios presented in Table 5 and for each component with n_{H_2} varying from 10^2 to 10^{10} cm^{-3} and N_{H_2O} varying from 10^{12} to 10^{20} cm^{-2} for six representative temperatures (100, 300, 500, 750, 1000 and 1500 K). For the individual components the line-width in the models was set to the value derived from the Gaussian fitting while a typical line-width of 20 km s^{-1} was used for the average ratios. The density in these calculations is that of the material that has already passed through the shock, i.e. the post-shock gas. This is therefore different from the (pre-shock) density in the envelope as given by n_{1000} in the Sect. 4.3, and for shocks in the jet can be entirely unrelated.

In order to compare the model ratios for each grid to the observed ratios, the observations must be corrected for differences in beam-size. All observed intensities and upper limits are corrected to the $2_{02}-1_{11}$ (988 GHz) beam and ratioed to that line. For the cavity shock component this is done assuming that the emission comes from a 1D structure (i.e. $I \propto \theta_{beam}$) due to the extended nature of the outflows as discussed in Sect. 3.2.3. The spot shock components are assumed to be point-like (i.e. $I \propto \theta_{beam}^2$) as discussed in Sect. 3.2.4.

The best-fit and significance of the models are found using χ^2 minimisation of the observed and model line ratios with respect to the $2_{02}-1_{11}$ line. For most lines, the beam correction is relatively small, particularly for the cavity shock (see Table 5). However, as already discussed in Sects. 4.1 and 4.2, there may be some emission which is not included in the $2_{12}-1_{01}$ line but is inside the beam for the other lines, or equally is included in the $1_{10}-1_{01}$ line but none of the others. In theory this should be accounted for by the beam correction, but since we do not know the true spatial distribution of the emission then we do not know

[3] http://home.strw.leidenuniv.nl/~moldata/

how good our assumption of point-like and linear emission is for the spot and cavity shocks respectively.

We therefore include an uncertainty in the beam correction factor in our calculation of the χ^2 when this correction is more than a factor of 1.5, added in quadrature with the uncertainties on the intensities. The exponent of the beam correction factor can only be between 0 (for uniform emission) and 2 (for a point source), so for the shock components where we assume a point-source emitting region this uncertainty is only applied in the direction of a smaller correction exponent. The effect of this additional uncertainty is to give less weight to those lines which have large beam correction factors with respect to the $2_{02}-1_{11}$ line.

The area of the emitting region in the plane of the sky is then calculated from the ratio of the model and observed $2_{02}-1_{11}$ integrated intensity, i.e. the fraction of the beam that can be at the model intensity in order to match the observed value. This is converted to a radius assuming a circular emitting region at the distance of the object for ease of comparison.

In certain parts of the parameter space searched with RADEX, certain water transitions show strong maser activity (see e.g. Kaufman & Neufeld 1996). These are mostly models with low post-shock density and high water column density. As described in van der Tak et al. (2007), RADEX is not well suited to modelling maser activity. While none of the fitted lines are affected, masing in other lines can hamper convergence of the calculation. We have therefore limited the opacity to a certain negative value (−10) as also implemented in RATRAN (Hogerheijde & van der Tak 2000). Changing this value does not affect the results of our fitting.

In addition, the standard version of RADEX calculates the line excitation and τ using a Gaussian profile, but the integrated intensity assuming a box-line-profile and thus $I \propto (1 - \exp(-\tau))$ which is almost independent of τ for $\tau >$ a few. However, for a Gaussian line profile, $I \propto \int(1 - \exp^{-\tau \exp(-k(v/\sigma)^2)})\mathrm{d}v$ (see e.g. Avrett & Hummer 1965). This leads to RADEX underestimating the line intensity for high opacity, which is relevant for water. We therefore correct the line fluxes in the vein of a curve-of-growth analysis by multiplying those output by RADEX by a factor α given by:

$$\alpha = \frac{\int_{-\infty}^{\infty} 1 - \exp\left(-\tau \mathrm{e}^{-x^2}\right) \mathrm{d}x}{\sqrt{\pi}\,(1 - \mathrm{e}^{-\tau})}, \quad (3)$$

where $x = \sqrt{k}v/\sigma$. For $\tau \lesssim 0.2$, $\alpha \simeq 1$ because no correction is required. The largest correction at high τ (e.g. 10^4) is approximately a factor of three.

In some extra-galactic sources, pumping of the higher-excited water lines by the far-IR dust continuum is required to reproduce the line ratios (e.g. González-Alfonso et al. 2010). We therefore ran grids of models including the far-IR continuum from the SEDs reported by Kristensen et al. (2012) scaled by a range of scaling factors to test if this is important in low-mass protostars. The radiation field must be smaller than 2×10^{-5} times the bolometric luminosity before any reasonable fits to the observations could be found. Even for these low radiation levels, the best fits were not significantly different or better than those without the continuum radiation field included. In particular, there are no moderate-density ($n_{\mathrm{H_2}}$ of order 10^{5-6}), high radiation field solutions which fit the data, as is the case for external galaxies. In addition, our observed line ratios, particularly for $1_{11}-0_{00}/2_{02}-1_{11}$ and $2_{11}-2_{02}/2_{02}-1_{11}$, differ from the extragalactic case, where the $2_{02}-1_{11}$ transition is significantly enhanced with respect to all other lines. We conclude that the far-IR radiation field does not play an important role in the excitation of water in low-mass sources, and is therefore not considered further.

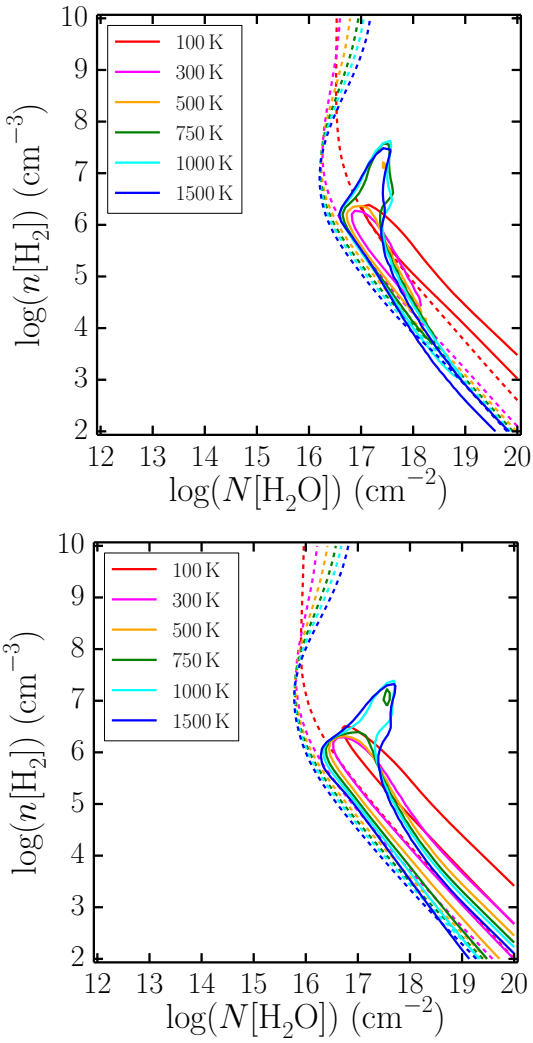

Fig. 11. Results of comparison between the average line ratios presented in Table 5 with RADEX models for a range of $n_{\mathrm{H_2}}$ and $N_{\mathrm{H_2O}}$ for six different temperatures ranging from 100 to 1500 K. The solid lines indicate the region within 1σ while the dashed lines show where the plane-of-the-sky emitting area, obtained from the ratio of the observed and model intensity in the $2_{02}-1_{11}$ line, corresponds to a circle with radius 100 AU.

4.4.2. Results

Figure 11 shows, in solid lines, a comparison of the 1σ χ^2 contours for fits between grids of RADEX models over $N_{\mathrm{H_2O}}$ and $n_{\mathrm{H_2}}$ at a range of temperatures from 100−1500 K to the average line ratios for cavity and spot shocks given in Table 5. A typical FWHM of 20 km s^{-1}, distance of 200 pc and intensities of the 988 GHz line of 5 and 2.4 K km s^{-1} were used based on the average of the sample. For the $H_2^{18}O$ lines, since most sources show non-detections in all lines, the σ_{rms} values for Class 0 sources from Table 2 were converted to upper-limit intensities. The dashed lines show where the ratio of the model and observed fluxes corresponds to a radius of 100 AU in the plane of the sky for a circular emitting region, with smaller regions to the upper right of this line and larger to the lower left.

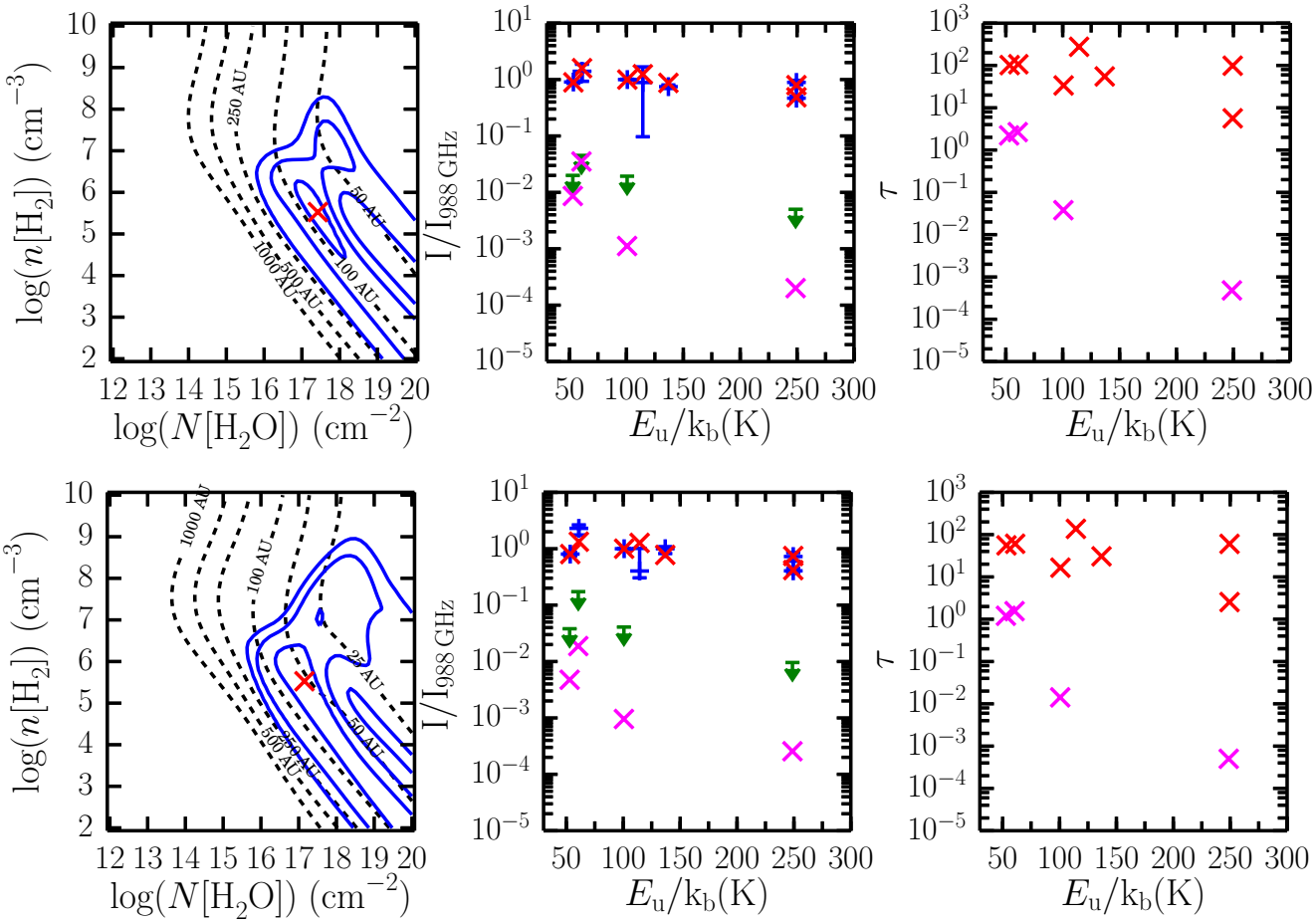

Fig. 12. RADEX results for the average line ratios for the cavity shock (*top*) and spot shock (*bottom*) components assuming T = 300 and 750 K respectively. The *left-hand panels* show the best-fit (*red cross*) and 1, 3 and 5σ confidence limits (blue contours) for a grid in $n_{\rm H_2}$ and $N_{\rm H_2O}$. The black dashed contours show the corresponding radius of the emitting region. The *middle panels* show a spectral line energy distribution comparing the observed (blue for H_2O, green for $H_2^{18}O$) and best-fit model (red for H_2O, magenta for $H_2^{18}O$) results. The *right-hand panels* show the optical depth for each line for the best-fit model.

Aside from the 100 K model, there is a slight trend towards higher $n_{\rm H_2}$ and lower $N_{\rm H_2O}$ with increasing temperature but the contours and emitting region sizes derived from the different models are effectively the same within the uncertainties. This insensitivity of low-J water emission lines to temperature within the post-shock density and column density regime present towards our sources has also been seen in other studies (see also Kristensen et al. 2013; Santangelo et al. 2014). The temperature and density cannot both be the same as traced by low-J CO, which traces temperatures of ∼100 K but is insensitive to density (Yıldiz et al. 2013), because otherwise water would trace similar gas (and thus have similar line profiles), which is not the case (e.g. Nisini et al. 2010; Kristensen et al. 2012). Higher-J line profiles, such as ^{12}CO 16−15 are more similar to water (Kristensen et al. 2013; Kristensen et al., in prep.), and trace warmer gas (e.g. Karska et al. 2014), supporting the idea that water is tracing material which is warmer than 100 K.

We therefore follow Kristensen et al. (2013) in assuming a temperature of 750 K for the spot shock components. This is also similar to the hot component observed in CO rotation diagrams with PACS (e.g. Karska et al. 2014). These same observations also show a warm component in CO with a temperature of ∼300 K, which the observations of Santangelo et al. (2013) show is spatially associated with H_2O in the outflow cavity. We therefore assume a temperature of 300 K for the cavity shock components.

The fit to the average line ratios for the cavity and spot shock components are shown for 300 K and 750 K respectively in Fig. 12. The left-hand panel of each row shows 1, 3 and 5σ contours in blue with the best-fit (i.e. model with the lowest χ^2) marked with a red cross. These typically centre around two diagonal solutions; one with $n_{\rm H_2} \lesssim 10^6$ cm^{-3} and $N_{\rm H_2O} \gtrsim 10^{16}$ cm^{-2} and a parallel solution with $n_{\rm H_2} \lesssim 10^7$ cm^{-3} and $N_{\rm H_2O} \gtrsim 10^{17}$ cm^{-2}. In the first solution, the density is well below the critical density for all lines and the excitation is sub-thermal. For the second solution at least some of the lines are nearing thermal equilibrium. In both cases all H_2O lines, and even the lowest two non-detected $H_2^{18}O$ transitions, are optically thick (right-hand panels). Despite this, both the higher-density thermal solution and low lower-density non-thermal solution are likely still in the effectively thin regime.

The emitting region area for the average line ratios in the plane of the sky at the typical distance for our sources (200 pc) is relatively small, equivalent to a circular radius of order 50−100 AU. The solutions for the cavity and spot-shocks are very similar in terms of $n_{\rm H_2}$ and $N_{\rm H_2O}$, with the spot shocks having a slightly smaller emitting region due to the smaller absolute fluxes.

Though the tail of possible solutions within 1σ extends to lower densities and higher column densities, it is unlikely that the emission comes from a long cylinder in all sources, given the range in viewing angles within the sample. For example, assuming an abundance for water of 10^{-4} with respect to H_2, a water column density of 10^{19} cm^{-2} at a molecular hydrogen density of 10^3 cm^{-3} corresponds to a length along the column of 7×10^6 AU which is physically unlikely. Therefore, though there are formally solutions extending to the lower right in Fig. 11 and the left-hand panels of Fig. 12, the models at the upper left part of the solution are more likely from a geometrical point of view. The best-fit therefore provides a characteristic determination, with uncertainties in n_{H_2} and N_{H_2O} typically half to one order of magnitude if the other property is held constant. In comparison, a factor of two change in the temperature results in less than a factor of three change in n_{H_2} and N_{H_2O}, as does changing the assumed beam-correction from linear to point-like or vice versa.

The same analysis was also performed separately for all individual source components, with the average ratios used in cases where specific lines were not observed. We also restrict the best-fit solution to have a length along the column of no more than 5000 AU, assuming a water abundance of 10^{-4}, as lengths larger than this would be larger than the beam if rotated to the plane of the sky. Table 6 presents the best-fit results for the average line ratios and those sources where the 1σ contour covers less than 10% of the probed parameter space. Figures of the same form as Fig. 11 for these individual components are shown in Figs. A.8 to A.16. For the remaining sources the excitation conditions cannot be well-constrained, usually due to upper limits in multiple H_2O transitions. The χ^2 contours are usually elongated as also seen in Fig. 12.

The overall spread of best-fit H_2 number density vs. H_2O column density is shown in Fig. 13. The column densities given are over the emitting region in the plane of the sky, which have radii of order 5−300 AU assuming a circular shape (see Table 6). In all cases the observations exclude water column densities below $\sim10^{15}$ cm^{-2}. For those shock components already studied by Kristensen et al. (2013) we derive slightly lower densities, lower emitting region sizes and higher column densities. This partly stems from our correction of the RADEX intensities using Eq. (3), but is also because Kristensen et al. (2013) only considered water column densities of 4×10^{15}−10^{17} cm^{-2} and H_2 densities of 10^6−10^9 cm^{-3} and therefore only considered the thermal solution.

For most cavity shock components, the best fit favours the sub-thermal solution but there is usually a thermal solution within the 3 or 5σ contours as well. The analysis for the majority of spot shock components favours the thermal solution, resulting also in smaller emitting regions sizes on the sky, but in all components where this is the case there are also solutions within the 1σ contours in the sub-thermal solution. Therefore, while there is some spread in best-fit results, we cannot conclude that there is a significant difference between cavity and spot shock results when considering the 1σ results, as also seen for the average line ratios. The Class I sources tend to have smaller emitting region sizes compared to the Class 0 sources, but there is no significant difference in n_{H_2} and N_{H_2O}.

5. Discussion

The following subsections discuss separately the variation in properties between the different shock components (Sect. 5.1) and as a function of source evolutionary stage (Sect. 5.2).

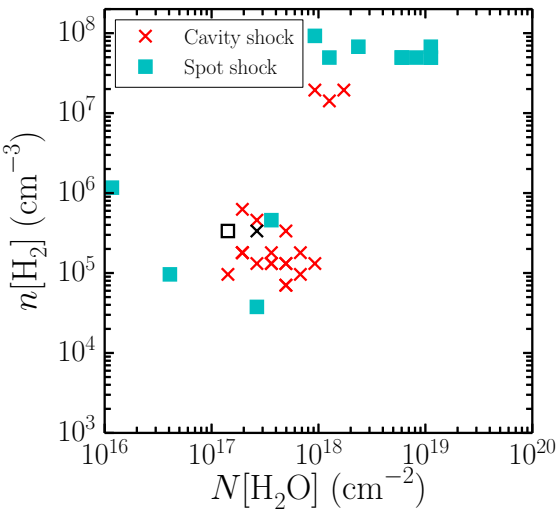

Fig. 13. Best-fit N_{H_2O} vs. n_{H_2} from the RADEX model grids for sources with well-constrained best-fits (i.e. 1σ contours include <10% of all models). The black square and cross indicate the best fit for the average spot and cavity shock line ratios.

We then attempt to synthesise this into a consistent picture in Sect. 5.3, before also comparing our results at the source position with others further from the central source (Sect. 5.4).

5.1. Cavity and spot shocks

The two different components seen in water spectra related to the outflow-jet system (cavity and spot shock) exhibit differences in terms of their line width and offset from the source velocity (see Fig. 7), in part due to how the components are classified. Some spot shock components have similar widths to the cavity shock component but are significantly offset from the source velocity while other spot shock components have similar offsets but smaller FWHM than the cavity shock components. However, the cavity and spot shock components show little difference in terms of their integrated intensity ratios or their line intensity ratios as a function of velocity (see Figs. 8 and 9). The relatively small spread in line ratios leads to the similarity of the physical conditions under which each component is generated, though the variation in absolute fluxes and line-widths leads to variation of $\sim$1 order of magnitude in N_{H_2O} and n_{H_2} if the sub-thermal and thermal solutions are considered separately (see Fig. 13). Thus, while the velocities that the gas is subject to may be different between these two components, the excitation is not.

The comparison with $H_2^{18}O$, the line intensity ratios, the line ratios as a function of velocity and the RADEX analysis (see Figs. 3, 8, 9 and Table 6 respectively) all agree that all H_2O transitions are likely optically thick across the whole line. However, the RADEX determinations for the density lie below the critical density of some or all of the observed transitions, so the lines are optically thick but effectively thin. The same determinations also suggest that the ground-state $H_2^{18}O$ may be marginally optically thick ($\tau \sim 1$), explaining why the determinations of optical depth from $H_2O/H_2^{18}O$ ratios are lower than those suggested by RADEX.

The lack of variation in line ratio as a function of velocity is in marked contrast to what is found for CO, for which line ratios between lower and higher energy transitions, for example between J = 3−2 and 10−9, often vary by a factor of 2 or more,

Table 6. RADEX results for sources where the 1σ contours include <10% of all models.

Source	Comp.[a]	*FWHM* (km s^{-1})	$\chi^2_{\rm best}$	T (K)	$N_{\rm best}$[b] cm^{-2}	$n_{\rm best}$ cm^{-3}	r (AU)	$\tau_{988\,\rm GHz}$
Average	C	20.0	0.8	300	3×10^{17}	3×10^{5}	78.7	33.7
	S	20.0	0.8	750	1×10^{17}	3×10^{5}	54.2	16.5
L1448-MM	S	23.0	7.0	750	3×10^{17}	4×10^{4}	126.0	54.0
	S	39.8	2.8	750	1×10^{19}	7×10^{7}	15.6	5.5
	C	44.6	1.8	300	7×10^{17}	1×10^{5}	136.9	58.0
IRAS2A	C	14.0	1.3	300	2×10^{17}	2×10^{5}	103.4	43.8
	S	39.2	1.0	750	4×10^{17}	5×10^{5}	58.3	16.4
IRAS4A	S	9.9	1.0	750	4×10^{16}	1×10^{5}	175.7	20.0
	C	41.4	0.1	300	5×10^{17}	3×10^{5}	118.6	31.5
IRAS4B	S	5.1	1.0	750	1×10^{16}	1×10^{6}	166.2	5.0
	C	24.6	7.0	300	3×10^{17}	5×10^{5}	157.6	26.2
L1527	C	20.2	2.3	300	4×10^{17}	1×10^{5}	25.4	58.1
BHR71	S	28.3	2.0	750	6×10^{18}	5×10^{7}	8.5	4.3
	C	52.3	2.5	300	9×10^{17}	1×10^{5}	54.6	57.5
	S	59.0	1.4	750	1×10^{19}	5×10^{7}	8.4	3.8
IRAS 15398	C	16.3	4.3	300	3×10^{17}	1×10^{5}	46.9	54.4
L483	C	18.5	2.1	300	2×10^{18}	2×10^{7}	28.4	25.8
Ser-SMM1	S	3.7	1.2	750	9×10^{17}	9×10^{7}	60.5	4.6
	C	18.9	4.9	300	2×10^{17}	6×10^{5}	334.8	22.5
Ser-SMM3	C	30.1	0.8	300	5×10^{17}	7×10^{4}	156.8	68.0
Ser-SMM4	S	10.7	1.7	750	2×10^{18}	7×10^{7}	32.9	4.1
	C	46.1	2.0	300	5×10^{17}	7×10^{4}	176.3	50.9
L723	C	24.9	2.3	300	5×10^{17}	1×10^{5}	40.5	62.3
B335	S	6.5	1.1	750	1×10^{18}	5×10^{7}	12.0	3.9
	C	40.9	2.4	300	7×10^{17}	2×10^{5}	37.6	49.2
L1157	C	23.2	2.3	300	4×10^{17}	2×10^{5}	73.9	47.3
	S	35.7	1.5	750	8×10^{18}	5×10^{7}	11.7	4.7
	S	47.7	1.2	750	1×10^{19}	5×10^{7}	10.8	4.8
L1489	C	20.0	2.4	300	4×10^{17}	1×10^{5}	32.3	58.5
TMR1	C	13.0	3.4	300	2×10^{17}	2×10^{5}	32.1	45.9
TMC1	C	12.7	2.4	300	2×10^{17}	2×10^{5}	21.2	46.7
IRAS 12496	C	25.5	3.1	300	5×10^{17}	1×10^{5}	30.9	61.3
	S	25.7	1.4	750	6×10^{18}	5×10^{7}	5.0	4.7
GSS30-IRS5	C	14.5	2.0	300	1×10^{18}	1×10^{7}	25.6	26.3
Elias29	C	13.5	2.6	300	9×10^{17}	2×10^{7}	27.2	20.0
RNO91	C	6.0	2.3	300	1×10^{17}	1×10^{5}	24.1	78.2

Notes. [(a)] Component Type: C=cavity shock and S = spot shock. [(b)] Column density over the emitting region.

at least for Class 0 sources, between offsets of 5 and 20 km s^{-1} from the source velocity (e.g. see Fig. 13 of Yıldiz et al. 2013). This is likely because the low and higher J CO transitions trace different parts of the outflow as a function of both excitation and velocity, while the water emission studied here is coming from gas under similar conditions for all velocities and transitions.

The spot shock components contribute 20−30% of the total integrated emission in H_2O lines, while the cavity shock component provides ∼70−80% (see Table 4). This is broadly consistent with the ratio of the number of molecules in the warm (∼300 K) and hot (∼750 K) CO components identified by Karska et al. (2014, see their Table 3) in high-J PACS observations of the same sample. We therefore suggest that the warm and hot components in the PACS CO observations are related to the cavity and spot shock components respectively in our observations, a conclusion also reached for the spot shock components by Kristensen et al. (2013).

The low line offset with respect to the width of the line is consistent with the cavity shock emission originating in a C-type shock. In contrast, the larger offset with respect to the width for spot shock components, in some cases such that there is little or no contribution at the source velocity, suggests that they originate in J-type shocks. The small beam filling factors, of similar order for all components, point towards compact emitting regions. This, combined with light hydrides seen in absorption against the far-IR continuum led Kristensen et al. (2013) to argue that some of the spot shock components are located close to the central source where the impact from any wind will have the highest energy. Some spot shocks, particularly those with large velocity offsets, likely originate in shocks within the protostellar jet, as observed in other species at higher angular resolution (e.g. Santiago-García et al. 2009). Spot shock components originating in either location can have low offsets from the source velocity if there is a large angle between the line of sight and the direction

of motion caused by the shock. In both regions, water is being (re-)formed via high-temperature (≳300 K) gas phase chemistry.

For the cavity shock component, we assumed during the RADEX calculations that the emission is extended along one axis due to the extended H_2O $2_{12}-1_{01}$ (1670 GHz) emission observed towards several of the sources in our sample (see e.g. Vasta et al. 2012; Santangelo et al. 2012, 2013; Nisini et al. 2013). For this to be consistent with the small emitting regions derived, this suggests a very small extent (1−30 AU) perpendicular to the outflow axis. The width of a C-type shock depends on the ion-neutral coupling length, which is proportional to $(n_{H_2} \times x_i)^{-1}$, where x_i the degree of ionisation (Draine 1980). Thus shocks are narrower for higher densities. For the densities inferred here ($\sim 10^5-10^8$ cm^{-3}; Table 6), typical widths of the H_2O emitting regions range from a few hundred AU to less than ten AU (Visser et al. 2012). If the C-type shocks are irradiated as suggested by Karska et al. (2014), the degree of ionisation increases which leads to narrower shocks. Thus, the narrow width of the emitting region inferred here (<30 AU) are consistent with either high densities or irradiated shocks; since the excitation analysis generally points to a lower density, irradiated shocks are the preferred solution.

5.2. Class 0 vs. Class I

The median FWZI of the observed water lines drops significantly from Class 0 to Class I sources (see Table 2). This is also seen in the average spectra (Fig. 14), which are produced by averaging over all spectra with a peak $S/N \geq 4$ after normalising to the peak intensity, and in the FWHM and peak intensity for the Gaussian components (see Figs. 7). This is relatively independent of the source luminosity or envelope mass, but is related to the pre-shock density of the envelope as probed by n_{1000}.

The peak brightness of the water lines also decreases, on average, from Class 0 to Class I, as does the fraction of the total intensity in *J*-shock related spot shock components. There is also a shift from the quiescent envelope appearing in absorption to emission. However, as shown in Fig. 10, this is not directly related to T_{bol} or F_{CO}, but rather to M_{env} and n_{1000}. This correlation holds even though the lines are optically thick because they are likely effectively thin and thus the intensity still scales with $N_{H_2O} \times n_{H_2}$ which is related to M_{env}. While the average M_{env} and n_{1000} values for Class I sources are lower than for Class 0 sources, there is considerable overlap without clear segregation of the two populations. That the available reservoir is only weakly related to the evolutionary stage of the source is further confirmed by the very similar N_{H_2O} and n_{H_2} results obtained from the RADEX analysis (Fig. 13). That said, the emitting region sizes for the Class I sources are on the small end of the distribution seen for the Class 0 sources.

We suggest that the decrease in intensity of water emission ($\propto T_{peak} \times FWHM$) as the source evolves from Class 0 to Class I is primarily related to the decrease in the velocity of the wind which drives the outflow. However, Herbig-Haro objects related to the jet in more evolved Class II/III systems have similar fast velocities to the jets in Class 0/I sources.

One scenario which seems consistent with our findings would be that the velocity of the wind perpendicular to the jet drops as it moves further from the jet (see, e.g., Panoglou et al. 2012; Agra-Amboage et al. 2014; Yvart et al., in prep.) and that as the source evolves the outflow cavity widens, leading to weaker impacts on the cavity wall. In many cases it may have decreased to such an extent as the sources age that it is no longer fast enough to cause a significant *J*-shock even at the base of the outflow, though some emission related to the jet may remain. The cavity shock layer is also likely to get thinner as the shock cannot penetrate as far into the envelope, again leading to smaller filling factors. Indeed, at some distance from the source the oblique velocity of the wind probably becomes so low that it cannot even sputter ice from the grain mantle. The source is probably still capable of powering an entraining layer in CO since this is still in the gas phase, which is why peak H_2O brightness and outflow force from low-*J* CO show little segregation with evolution. The decrease in envelope mass is then a weaker factor, as long as there is still enough gas with high enough density and gas-phase water abundance. We speculate that a lack of reservour may become more important for source evolving from Class I to Class II.

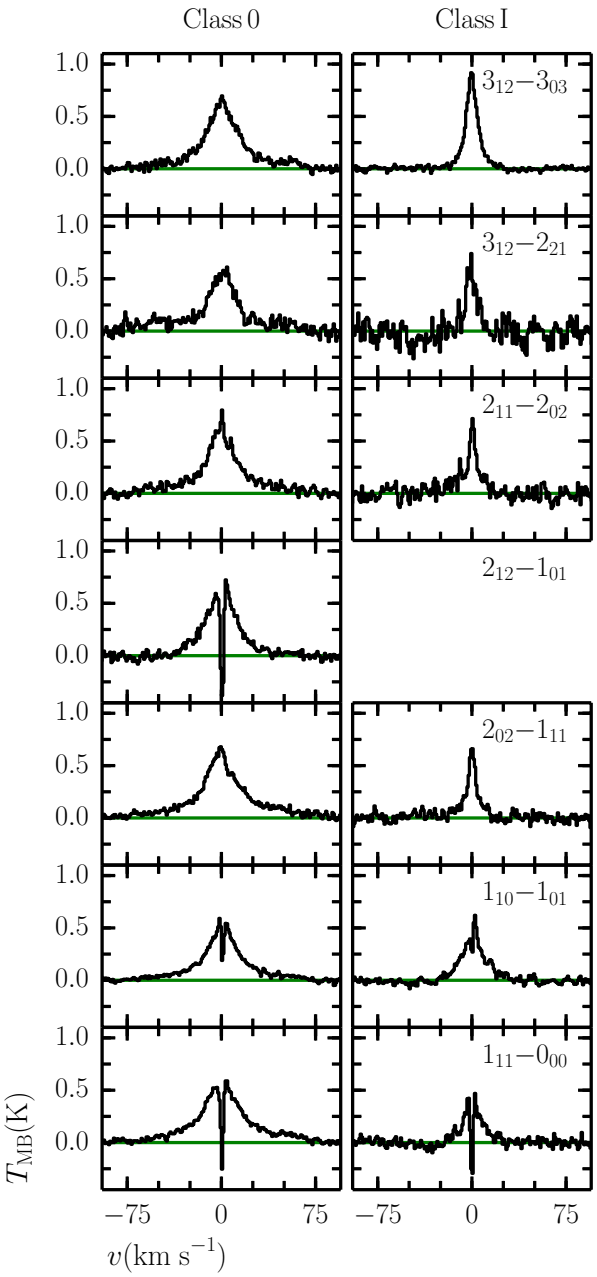

Fig. 14. Normalised average spectra for Class 0 (*left*) and I (*right*) sources. The green line indicates the baseline.

5.3. A consistent picture of water emission

A consistent picture, summarised in Fig. 5, is one where H_2O emission from the cavity shock component traces C-type shocks in a thin layer (of thickness only a few AU) at the interface with the cavity walls. Close to the central source this becomes a *J*-shock as traced by the spot shock component (see also Fig. 9 of Suutarinen et al. 2014). This is because the angle of impact between the wind and the cavity wall is large close to the base of the outflow and becomes more oblique with distance from the central source. The pre-shock conditions probably transition smoothly between these two regimes, given the constant line ratios as a function of velocity (Fig. 9) and similar densities and column densities of the spot and cavity shock components (Fig. 13). However, the change from a C to a *J*-type shock causes a dramatic difference in the velocity distribution of the post-shock material, resulting in the distinctly separate components we observe. This active shocked layer is distinct from the cooler entraining turbulent layer traced by low-*J* CO. It is not clear whether water is sputtered from the ice mantles of dust grains or formed via gas-phase chemistry in this actively shocked region. The answer is probably some combination of both mechanisms, the proportion of each varying smoothly with velocity (Van Loo et al. 2013; Suutarinen et al. 2014).

PACS CO observations of low-mass protostars generally find two temperature components (warm ≈ 300 K and hot ≈ 750 K). The emitting region sizes, column and post-shock densities we have obtained for the different components are similar to those for IRAS4B by Herczeg et al. (2012), for L1448-MM by Lee et al. (2013) and the hot component for Ser-SMM1 by Goicoechea et al. (2012) from PACS observations of H_2O. We exclude the cold component for Goicoechea et al. (2012) because their analysis tied H_2O to low-*J* CO lines which do not trace the same gas (e.g. Santangelo et al. 2013). In particular, the *J*-shock related spot shock components and the C-shock related cavity shock components match well to the hot and warm PACS components respectively, both in their individual properties and their relative fractions of the total intensity. That there are fewer spot shocks observed in emission towards Class I sources is consistent with the lack of hot CO in Class I sources observed by Karska et al. (2014). Green et al. (2013) detect hot CO towards more sources in their sample, but this is still consistent with our results as emission at 20% of the cavity shock component intensity would be too weak to be detected for those sources which are in both samples.

What is clear is that a considerable amount of the energy injected by the jet and/or outflow into the envelope is not traced by the entrained outflowing gas, but rather in the various shocks traced by water. Given that the shock related H_2O components have larger line-widths than seen in low-*J* CO (cf. Yıldiz et al. 2013), there may be a significant amount of momentum and energy carried away by these components compared to that in classical CO outflows. Bjerkeli et al. (2012) compared the momentum and energy in H_2O and CO for the VLA1623 outflow using H_2 observations to calculate abundances for water. They found water abundances with respect of H_2 of $(1-8) \times 10^{-7}$, that the momentum in water was ~25% that of CO and that the energies were comparable. However, the water abundances they derive are quite low compared to determinations for other sources (e.g. Santangelo et al. 2013, find $0.3-1 \times 10^{-5}$), so the mass, momentum and energy calculated from H_2O may be an overestimate. Even so, studies which only use low-*J* CO to quantify the impact of outflows at the source position probably underestimate the true mass, momentum, angular momentum and kinetic energy injected into the envelope and surrounding molecular cloud. Addressing this in a quantitative way requires a determination of the H_2O abundance relative to H_2 as a function of velocity, something that cannot be done with the observations presented here alone. This will be the subject of a future paper using HIFI observations of the high-*J* CO 16−15 line (Kristensen et al., in prep.).

5.4. On source vs. off source

Having compared the various on-source components and their properties, it is also important to consider how our results compare to those obtained for shock positions further away from the central source. In general, the line profiles for off-source emission have similar maximum velocities but are less symmetric than at the source position (Vasta et al. 2012; Santangelo et al. 2012; Busquet et al. 2014), as might be expected for regions with only red or blue shifted outflow emission. While Gaussian decomposition similar to that used here has not been presented for those observations, some additional slightly offset features can be seen in some line profiles which are reminiscent of the on-source spot shock component. At some locations, particularly away from the brightest parts of the outflow, the line shape becomes more like the classical triangular shape of some CO outflows (Santangelo et al. 2014). In addition, there can be significant differences in line shape between H_2O transitions, resulting in line ratios (and thus excitation conditions) which vary with velocity.

Table 7 presents a summary of recent determinations of the excitation conditions towards such regions for some of the sources present in our study (Santangelo et al. 2013, 2014; Busquet et al. 2014). Aside from the differences in isolating which emission to integrate over, these studies used similar Large Velocity Gradient models in their analysis, sometimes simultaneously fitting emission from water and other species also expected to originate in the outflow. As such, though the methods are not precisely the same, the results of these other studies should be comparable with the analysis presented in this paper.

We find much smaller emitting regions for on-source emission than derived for the off-source shock positions. Figure 15 shows a comparison of the densities and beam-averaged column densities we derive with those in Table 7 and those from Tafalla et al. (2013). Averaged over the beam, the densities and column densities are very similar, though the absolute column densities are lower off-source due to the larger emitting regions. Lower column density at larger distances from the central source will lead to lower optical depths in the water lines. There are two possible options for this difference in column density.

Firstly, the water abundance could be higher at the source position than at the shock spots. Certainly lower water abundances have been found at the shock positions (e.g. Santangelo et al. 2013; Busquet et al. 2014) than the value of $\sim 10^{-4}$ expected if all oxygen is forced into water by warm gas-phase chemistry. It is unlikely that H_2O could be converted into other species more efficiently at the off-source positions because the reaction rates for H_2O reacting with H or any other species are low (Snell et al. 2005; McElroy et al. 2013). The gas-phase H_2O abundance could be lower at the shock spots if sputtering is less efficient at the off-source positions because the velocity or density is lower (Caselli et al. 1997). However, the line-widths are large and post-shock densities are similar to the source position (see Fig. 15).

Alternatively, the difference may come from a change in the nature of the shocks being observed on and off source. The on-source cavity and spot shock components most likely exist as

Table 7. Summary of off source H_2O excitation conditions.

Source	Comp.[a]	T (K)	N_{H_2O}[b] (cm^{-2})	n_{H_2} (cm^{-3})	r[c] (AU)	Ref.
L1448-B2	W	450	3×10^{14}	1×10^{6}	2000	1
	H	1100	$(0.4–2)\times10^{16}$	$(0.5–5)\times10^{6}$	~120	1
L1157-B1	W	250–300	$(1.2–2.7)\times10^{16}$	$(1–3)\times10^{6}$	1600	2
	H	900–1400	$(4.0–9.1)\times10^{16}$	$(0.8–2)\times10^{4}$	300–800	2
IRAS4A-R2	W	300–500	$(1.3–2.7)\times10^{13}$	$(3–5)\times10^{7}$	1200–2000	3
	H	1000	$(0.7–1.3)\times10^{16}$	$(1–4)\times10^{5}$	350	3

Notes. [(a)] Component type: W = warm and H = hot. [(b)] Column density over the emitting region. [(c)] Radius of emitting region on the sky, calculated assuming a circular emitting area.

References. (1) Santangelo et al. (2013); (2) Busquet et al. (2014); (3) Santangelo et al. (2014).

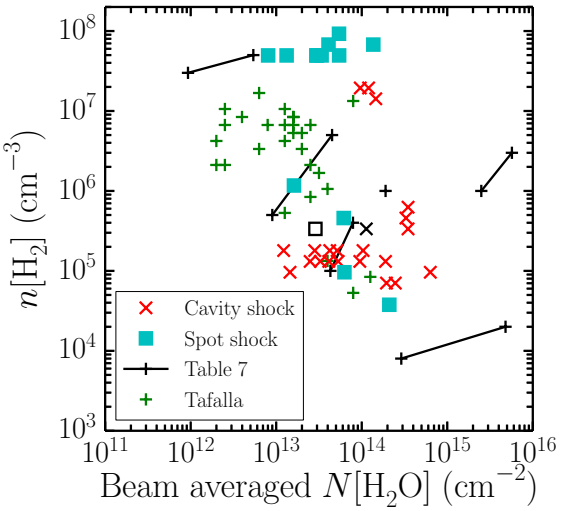

Fig. 15. Comparison of the conditions obtained in Sect. 4.4.2 with those from the literature in Table 7 and from Tafalla et al. (2013). The column densities have been averaged over the $1_{10}-1_{01}$ beam as in Tafalla et al. (2013). The black square and cross indicate the best fit for the average spot and cavity shock line ratios.

a thin layer at the boundary of the outflow cavity, as discussed above. As such, a parcel of post-shock gas cannot move azimuthally as it is in pressure equilibrium with the neighbouring parcels which are also in the post-shock. Expansion perpendicular to the outflow axis into the envelope may take place over time as the cavity opening angle increases but this will be resisted by the higher-density material in the envelope. Thus the only "easy" expansion route for the gas will be away from the central protostar along the outflow cavity layer. This will fill a larger volume at larger distances while being subject to weaker shocks, hence the increasing beam-emitting area and decreasing column density. Indeed, this is consistent with the extended component seen in the water mapping observations of Santangelo et al. (2014).

In contrast, the material in the post-shock of the bow-shocks is subject to the full direct impact of the jet rather than an oblique shock. It will therefore be a *J*-shock at or near the velocity of the jet, and may have a higher temperature and/or harsher UV field than in the on-source spot shocks. This would lead to a lower water abundance at the off-source bow-shock relative to the cavity shock. The post-shock density at the bow-shock is also higher than that of the surrounding cloud and so it can expand in most directions. Indeed, it will seek to do this as it is likely over-pressured with respect to its surroundings. The combination of a more violent and thus hotter initial shock, a pressure difference and freedom to expand in more directions, a different radiation field and different abundance would result in different excitation of the H_2O in the off-source bow-shock than in the spot-shocks on source. This in turn leads to line ratios which vary with both position and velocity, because the off-source cavity shock extends over a larger region and has different physical conditions and velocity field when compared to the bow-shocks. This is again consistent with the smaller emitting area and lower density found by Santangelo et al. (2014) towards the hot component in their maps of the NGC 1333-IRAS4A shock positions compared to their warm component.

6. Summary and conclusions

In this paper, we have presented velocity-resolved *Herschel* HIFI spectra of multiple water transitions for the whole low-mass Class 0/I subsample (29 sources) of the WISH survey. Our main findings are as follows:

- All water transitions for a given source studied here show very similar line profile shapes with consistent kinematic components.
- Three distinct types of kinematic component can be identified: envelope, cavity shock and spot shock. The velocity offsets and line widths of the cavity and spot shock components are consistent with origin in C type shocks along the outflow cavity wall, and with *J*-shocks near the base of the outflow or in the jet respectively. The excitation conditions and relative fraction of the total intensity in each source suggest that the spot shock component is associated with the hot (~750 K) CO component seen in PACS observations of Class 0/I protostars and the cavity shock component is associated with the warm (~300 K) PACS CO component.
- The line ratios are constant with velocity and similar for all sources. The emission is optically thick but effectively thin at all velocities, and traces material with post-shock densities of $n_{H_2} \sim 10^5–10^8$ cm^{-3} and column densities of $N_{H_2O} \sim 10^{16}–10^{18}$ cm^{-2}. All emission originates in compact emitting regions: for the spot shocks these correspond to point sources with radii of order 10–200 AU, while for the cavity shock these come from a thin layer along the outflow cavity wall with thickness of order 1–30 AU.

- The excitation conditions of the different components are relatively similar at the source position. The emitting regions are also similar between the different components.
- The major difference between the Class 0 and I sources is not in excitation conditions, but rather a decrease in line-width and intensity for more evolved sources. Coupled with the lack of *J*-shock components observed in older sources, this suggests that the decrease in water emission as the source evolves is primarily due to a decrease in the velocity of the wind which drives the outflow rather than the decrease in envelope density or mass. The envelope mass will likely become more important in the evolution from Class I to Class II.
- The off-source excitation conditions reported in the literature for H_2O have similar densities but lower column densities and larger emitting regions than the on-source emission. We suggest that this difference is because the material in off-source bow-shocks has more freedom to expand and has a higher pressure difference with surrounding material than the on-source shocks in the jet or near the base of the outflow.

Water is therefore revealing new information about the inner workings of outflows and the relationship between outflows and their driving sources. The remaining steps are to derive the water abundance, and thus obtain a quantitative comparison of the energy, momentum and mass in water compared to other tracers, and to explore these effects in a larger number of sources in order to see whether the trends that the WISH sample hint at, e.g. the separate trends between $L_{\rm bol}$ and water line intensity for Class 0 and I sources, are robust. These will be explored in upcoming papers, paving the way for a comprehensive understanding of all parts of the jet-outflow system.

Acknowledgements. The authors would like to thank the anonymous referee and Gary Melnick for helpful comments which improved the clarity and content of the paper, and U. Yıldiz for assistance with HIPE and data reduction. JCM is funded by grant 614.001.008 from the Netherlands Organisation for Scientific Research (NWO). Astrochemistry in Leiden is supported by the Netherlands Research School for Astronomy (NOVA), by a Spinoza grant and by the European Community's Seventh Framework Programme FP7/2007-2013 under grant agreement 238258 (LASSIE). HIFI has been designed and built by a consortium of institutes and university departments from across Europe, Canada and the United States under the leadership of SRON Netherlands Institute for Space Research, Groningen, The Netherlands and with major contributions from Germany, France and the US. Consortium members are: Canada: CSA, U.Waterloo; France: CESR, LAB, LERMA, IRAM; Germany: KOSMA, MPIfR, MPS; Ireland, NUI Maynooth; Italy: ASI, IFSI-INAF, Osservatorio Astrofisico di Arcetri-INAF; Netherlands: SRON, TUD; Poland: CAMK, CBK; Spain: Observatorio Astronómico Nacional (IGN), Centro de Astrobiología (CSIC-INTA). Sweden: Chalmers University of Technology – MC2, RSS & GARD; Onsala Space Observatory; Swedish National Space Board, Stockholm University – Stockholm Observatory; Switzerland: ETH Zurich, FHNW; USA: Caltech, JPL, NHSC.

References

Agra-Amboage, V., Cabrit, S., Dougados, C., et al. 2014, A&A, 564, A11
Andre, P., Ward-Thompson, D., & Barsony, M. 1993, ApJ, 406, 122
Avrett, E. H., & Hummer, D. G. 1965, MNRAS, 130, 295
Bacciotti, F., & Eislöffel, J. 1999, A&A, 342, 717
Bachiller, R., Martin-Pintado, J., Tafalla, M., Cernicharo, J., & Lazareff, B. 1990, A&A, 231, 174
Bachiller, R., Martin-Pintado, J., & Fuente, A. 1991, A&A, 243, L21
Bjerkeli, P., Liseau, R., Larsson, B., et al. 2012, A&A, 546, A29
Bodo, G., Massaglia, S., Ferrari, A., & Trussoni, E. 1994, A&A, 283, 655
Bontemps, S., Andre, P., Terebey, S., & Cabrit, S. 1996, A&A, 311, 858
Busquet, G., Lefloch, B., Benedettini, M., et al. 2014, A&A, 561, A120
Canto, J., & Raga, A. C. 1991, ApJ, 372, 646
Caselli, P., Hartquist, T. W., & Havnes, O. 1997, A&A, 322, 296
Chieze, J.-P., Pineau des Forets, G., & Flower, D. R. 1998, MNRAS, 295, 672
Codella, C., Maury, A. J., Gueth, F., et al. 2014, A&A, 563, L3
Daniel, F., Dubernet, M.-L., & Grosjean, A. 2011, A&A, 536, A76
de Graauw, T., Helmich, F. P., Phillips, T. G., et al. 2010, A&A, 518, L6
Draine, B. T. 1980, ApJ, 241, 1021
Dubernet, M.-L., Daniel, F., Grosjean, A., & Lin, C. Y. 2009, A&A, 497, 911
Dzib, S., Loinard, L., Mioduszewski, A. J., et al. 2010, ApJ, 718, 610
Frank, A., Ray, T. P., Cabrit, S., et al. 2014, in Protostars and Planets VI, eds. H. Beuther, R. Klessen, C. Dullemond, & T. Henning (Tucson: Univ. of Arizona Press), in press
Goicoechea, J. R., Cernicharo, J., Karska, A., et al. 2012, A&A, 548, A77
Goldsmith, P. F., & Langer, W. D. 1999, ApJ, 517, 209
González-Alfonso, E., Fischer, J., Isaak, K., et al. 2010, A&A, 518, L43
Green, J. D., Evans, II, N. J., Jørgensen, J. K., et al. 2013, ApJ, 770, 123
Griffin, M. J., Abergel, A., Abreu, A., et al. 2010, A&A, 518, L3
Herczeg, G. J., Karska, A., Bruderer, S., et al. 2012, A&A, 540, A84
Hirano, N., Liu, S.-Y., Shang, H., et al. 2006, ApJ, 636, L141
Hogerheijde, M. R., & van der Tak, F. F. S. 2000, A&A, 362, 697
Hollenbach, D. 1997, in Herbig-Haro Flows and the Birth of Stars, eds. B. Reipurth, & C. Bertout (Kluwer Academic Publishers), IAU Symp., 182, 181
Jiménez-Serra, I., Caselli, P., Martín-Pintado, J., & Hartquist, T. W. 2008a, A&A, 482, 549
Jiménez-Serra, I., Martín-Pintado, J., Rodríguez-Franco, A., et al. 2008b, Ap&SS, 313, 159
Jørgensen, J. K., Bourke, T. L., Myers, P. C., et al. 2007, ApJ, 659, 479
Jørgensen, J. K., van Dishoeck, E. F., Visser, R., et al. 2009, A&A, 507, 861
Karska, A., Herczeg, G. J., van Dishoeck, E. F., et al. 2013, A&A, 552, A141
Kaufman, M. J., & Neufeld, D. A. 1996, ApJ, 456, 250
Kristensen, L. E., Ravkilde, T. L., Field, D., Lemaire, J. L., & Pineau Des Forêts, G. 2007, A&A, 469, 561
Kristensen, L. E., Visser, R., van Dishoeck, E. F., et al. 2010, A&A, 521, L30
Kristensen, L. E., van Dishoeck, E. F., Tafalla, M., et al. 2011, A&A, 531, L1
Kristensen, L. E., van Dishoeck, E. F., Bergin, E. A., et al. 2012, A&A, 542, A8
Kristensen, L. E., van Dishoeck, E. F., Benz, A. O., et al. 2013, A&A, 557, A23
Karska, A., Kristensen, L. E., van Dishoeck, E. F., et al. 2014, A&A, 572, A9
Lada, C. J., & Wilking, B. A. 1984, ApJ, 287, 610
Lee, J., Lee, J.-E., Lee, S., et al. 2013, ApJS, 209, 4
Linke, R. A., Goldsmith, P. F., Wannier, P. G., Wilson, R. W., & Penzias, A. A. 1977, ApJ, 214, 50
Manoj, P., Watson, D. M., Neufeld, D. A., et al. 2013, ApJ, 763, 83
Marseille, M. G., van der Tak, F. F. S., Herpin, F., & Jacq, T. 2010, A&A, 522, A40
McElroy, D., Walsh, C., Markwick, A. J., et al. 2013, A&A, 550, A36
Mottram, J. C., van Dishoeck, E. F., Schmalzl, M., et al. 2013, A&A, 558, A126
Müller, H. S. P., Schlöder, F., Stutzki, J., & Winnewisser, G. 2005, J. Mol. Struct., 742, 215
Neufeld, D. A., Gusdorf, A., Güsten, R., et al. 2014, ApJ, 781, 102
Nisini, B., Benedettini, M., Codella, C., et al. 2010, A&A, 518, L120
Nisini, B., Santangelo, G., Antoniucci, S., et al. 2013, A&A, 549, A16
Ott, S. 2010, in Astronomical Data Analysis Software and Systems XIX, eds. Y. Mizumoto, K.-I. Morita, & M. Ohishi (Astronomical Society of the Pacific), ASP Conf. Ser., 434, 139
Pagani, L., Vastel, C., Hugo, E., et al. 2009, A&A, 494, 623
Panoglou, D., Cabrit, S., Pineau Des Forêts, G., et al. 2012, A&A, 538, A2
Persson, M. V., Jørgensen, J. K., & van Dishoeck, E. F. 2012, A&A, 541, A39
Persson, M. V., Jørgensen, J. K., van Dishoeck, E. F., & Harsono, D. 2014, A&A, 563, A74
Pickett, H. M., Poynter, I. R. L., Cohen, E. A., et al. 2010, J. Quant. Spectr. Rad. Transf., 111, 1617
Pilbratt, G. L., Riedinger, J. R., Passvogel, T., et al. 2010, A&A, 518, L1
Poglitsch, A., Waelkens, C., Geis, N., et al. 2010, A&A, 518, L2
Pudritz, R. E., Ouyed, R., Fendt, C., & Brandenburg, A. 2007, in Protostars and Planets V, eds. B. Reipurth, D. Jewitt, & K. Keil (Tucson: Univ. of Arizona Press), 277
Raga, A. C., Cabrit, S., & Canto, J. 1995, MNRAS, 273, 422
Reipurth, B., Heathcote, S., Yu, K. C., Bally, J., & Rodríguez, L. F. 2000, ApJ, 534, 317
Roelfsema, P. R., Helmich, F. P., Teyssier, D., et al. 2012, A&A, 537, A17
San José-García, I., Mottram, J. C., Kristensen, L. E., et al. 2013, A&A, 553, A125
Santangelo, G., Nisini, B., Giannini, T., et al. 2012, A&A, 538, A45
Santangelo, G., Nisini, B., Antoniucci, S., et al. 2013, A&A, 557, A22
Santangelo, G., Nisini, B., Codella, C., et al. 2014, A&A, 568, A125
Santiago-García, J., Tafalla, M., Johnstone, D., & Bachiller, R. 2009, A&A, 495, 169
Schmalzl, M., Visser, R., Walsh, C., et al. 2014, A&A, in press, DOI: 10.1051/0004-6361/201424236

Schöier, F. L., van der Tak, F. F. S., van Dishoeck, E. F., & Black, J. H. 2005, A&A, 432, 369
Shadmehri, M., & Downes, T. P. 2008, MNRAS, 387, 1318
Shang, H., Li, Z.-Y., & Hirano, N. 2007, in Protostars and Planets V, eds. B. Reipurth, D. Jewitt, & K. Keil (Tucson: Univ. of Arizona Press), 261
Snell, R. L., Hollenbach, D., Howe, J. E., et al. 2005, ApJ, 620, 758
Suutarinen, A. N., Kristensen, L. E., Mottram, J. C., Fraser, H. J., & van Dishoeck, E. F. 2014, MNRAS, 440, 1844
Tafalla, M., Liseau, R., Nisini, B., et al. 2013, A&A, 551, A116
van der Tak, F. F. S., Black, J. H., Schöier, F. L., Jansen, D. J., & van Dishoeck, E. F. 2007, A&A, 468, 627
van der Tak, F. F. S., Chavarría, L., Herpin, F., et al. 2013, A&A, 554, A83
van Dishoeck, E. F., Kristensen, L. E., Benz, A. O., et al. 2011, PASP, 123, 138
van Dishoeck, E. F., Herbst, E., & Neufeld, D. A. 2013, Chem. Rev., 113, 9043
Van Loo, S., Ashmore, I., Caselli, P., Falle, S. A. E. G., & Hartquist, T. W. 2013, MNRAS, 428, 381
Vasta, M., Codella, C., Lorenzani, A., et al. 2012, A&A, 537, A98
Velusamy, T., Langer, W. D., & Marsh, K. A. 2007, ApJL, 668, L159
Visser, R., Kristensen, L. E., Bruderer, S., et al. 2012, A&A, 537, A55
Visser, R., Jørgensen, J. K., Kristensen, L. E., van Dishoeck, E. F., & Bergin, E. A. 2013, ApJ, 769, 19
Wilson, T. L., & Rood, R. 1994, ARA&A, 32, 191
Yıldiz, U. A., Kristensen, L. E., van Dishoeck, E. F., et al. 2013, A&A, 556, A89
Yıldiz, U. A., Kristensen, L. E., van Dishoeck, E. F., et al. 2014, A&A, submitted

Pages 23 to 49 are available in the electronic edition of the journal at http://www.aanda.org

Appendix A: Supplementary material

Table A.1. Observed water lines.

Line	Rest frequency[a] (GHz)	E_u/k_b (K)	A_{ul} (s^{-1})	n_{cr} (cm^{-3})	η_{mb}[b]	θ_{mb}[b] ($''$)	WBS resolution (km s^{-1})	HRS resolution (km s^{-1})	Obs. Time[c] Class 0/I (min)
H_2O $1_{10}-1_{01}$	556.93607	61.0	3.458×10^{-3}	1×10^{7}	0.75	38.1	0.27	0.03	13.5/20.7
H_2O $2_{12}-1_{01}$	1669.90496	114.4	5.593×10^{-2}	3×10^{8}	0.71	12.7	0.09	0.02	23.7/–
H_2O $3_{12}-2_{21}$	1153.12682	249.4	2.634×10^{-3}	8×10^{6}	0.64	18.4	0.13	0.06	13.0/9.9
H_2O $3_{12}-3_{03}$	1097.36505	249.4	1.648×10^{-2}	5×10^{7}	0.74	19.3	0.14	0.07	32.5 (306[d])/– (306[d])
$H_2^{18}O$ $1_{10}-1_{01}$	547.67644	60.5	3.290×10^{-3}	1×10^{7}	0.75	38.7	0.27	0.07	33.0–126.0/–
$H_2^{18}O$ $3_{12}-3_{03}$	1095.62739	248.7	1.621×10^{-2}	5×10^{7}	0.74	19.4	0.14	0.07	32.5 (306[d])/– (306[d])
H_2O $1_{11}-0_{00}$	1113.34306	53.4	1.842×10^{-2}	1×10^{8}	0.74	19.0	0.13	0.06	43.5/32.4
H_2O $2_{02}-1_{11}$	987.92670	100.8	5.835×10^{-3}	4×10^{7}	0.74	21.5	0.15	0.07	23.3/23.3
H_2O $2_{11}-2_{02}$	752.03323	136.9	7.062×10^{-3}	2×10^{7}	0.75	28.2	0.20	0.05	18.4/23.3
$H_2^{18}O$ $1_{11}-0_{00}$	1101.69826	52.9	1.785×10^{-2}	1×10^{8}	0.74	19.0	0.13	0.06	43.5/32.4
$H_2^{18}O$ $2_{02}-1_{11}$	994.67513	100.6	6.020×10^{-3}	4×10^{7}	0.74	21.3	0.15	0.04	40.6–46.7/–

Notes. [(a)] Taken from Daniel et al. (2011) and Dubernet et al. (2009) for H_2O and the JPL database (Pickett et al. 2010) for $H_2^{18}O$. [(b)] Calculated using equations 1 and 3 from Roelfsema et al. (2012). [(c)] Total time including on+off source and overheads. [(d)] Deep observation for IRAS2A and sources observed as part of OT2 programme OT2_rvisser_2.

Table A.2. Observation identification numbers.

Source	H_2O $1_{10}-1_{01}$	H_2O $2_{12}-1_{01}$	H_2O $3_{12}-2_{21}$	H_2O $3_{12}-3_{03}$[a]	H_2O $1_{11}-0_{00}$[b]	H_2O $2_{02}-1_{11}$	H_2O $2_{11}-2_{02}$	$H_2{}^{18}O$ $1_{10}-1_{01}$	$H_2{}^{18}O$ $2_{02}-1_{11}$
L1448-MM	1342203202	–	1342203253	1342201802	1342201803	1342203182	1342203216	1342203186	–
NGC 1333-IRAS2A	1342202067	1342215966	1342191701	1342215968[c]	1342191657	1342191606	1342191748	1342192206	1342191607
NGC 1333-IRAS4A	1342202065	1342203951	1342191721	1342249014[e]	1342191656	1342191605	1342191749	1342192207	–
NGC 1333-IRAS4B	1342202064	1342203952	1342191722	1342249851[e]	1342191655	1342191604	1342191750	1342202033	1342203179
L1527	1342192524	–	1342203256	–	1342216335	1342203156	1342203214	1342203188	–
Ced110-IRS4	1342201525	–	1342201734	–	1342200765	1342201756	1342201544	–	–
BHR71	1342201677	–	1342201732	–	1342200764	1342215915	1342201542	1342200755	–
IRAS 15398	1342213732	–	1342214446	–	1342214414	1342203165	1342204795	–	–
L483	1342217691	–	1342217730	1342207375	1342207374	1342218213	1342207618	1342207582	–
Ser-SMM1	1342208580	1342207660	1342207701	1342254450[c]	1342207379	1342194994	1342194561	1342194463	1342207657
Ser-SMM3	1342208579	1342215965	1342207699	1342207376	1342207377	1342207658	1342207617	1342207580	–
Ser-SMM4	1342208577	–	1342207700	1342207381	1342207380	1342194993	1342194562	1342194464	–
L723	1342210077	–	1342210152	–	1342210168	1342210041	1342210154	1342219172	–
B335	1342196409	–	1342230175	–	1342219248	1342219217	1342217716	1342219182	–
L1157	1342196407	–	1342198346	–	1342200763	1342197970	1342201551	1342199077	–
NGC 1333-IRAS3A	1342202066	–	–	–	–	–	–	–	–
L1489	1342203197	–	1342203254	–	1342203938	1342203158	1342203215	–	–
L1551-IRS5	1342203194	–	1342203258	–	1342203940	1342203153	1342203219	–	–
TMR1	1342192525	–	1342225917	–	1342203937	1342203157	1342203213	–	–
TMC1A	1342192527	–	1342225916	–	1342215969	1342203154	–	–	–
TMC1	1342192526	–	1342203255	–	1342216336	1342203155	–	–	–
HH46-IRS	1342196410	–	1342222281	–	1342194785	1342195041	1342194560	–	–
IRAS 12496	1342201526	–	1342201733	–	1342201590	1342201755	1342201543	–	–
GSS30-IRS1	1342205302	–	1342214442	1342250604[e]	1342214413	1342203163	1342204796	–	–
Elias29	1342204011	–	1342214443	1342249849[e]	1342214408	1342203162	1342204798	1342266143[d]	–
Oph-IRS63	1342205304	–	1342214441	–	1342214407	1342203164	1342204799	–	–
RNO91	1342205297	–	1342214440	–	1342214406	1342204512	1342204800	–	–
RCrA-IRS5A	1342215840	–	–	–	–	–	–	–	–
HH100	1342215841	–	–	–	–	–	–	–	–

Notes. [(a)] Observation also contains $H_2{}^{18}O$ $3_{12}-3_{03}$ in same sideband. [(b)] Observation also contains $H_2{}^{18}O$ $1_{11}-0_{00}$ in other sideband. [(c)] Deep integration. [(d)] Observed as part of OT2 programme OT2_evandish_4. [(e)] Observed as part of OT2 programme OT2_rvisser_2.

Table A.3. Observed properties of ortho-water line profiles.

Source	H_2O $1_{10}-1_{01}$				H_2O $2_{12}-1_{01}$				H_2O $3_{12}-2_{21}$				H_2O $3_{12}-3_{03}$			
	σ_{rms} (mK)	T_{MB}^{peak} (mK)	$\int T_{MB}\,dv$ (K km s^{-1})	*FWZI* (km s^{-1})	σ_{rms} (mK)	T_{MB}^{peak} (mK)	$\int T_{MB}\,dv$ (K km s^{-1})	*FWZI* (km s^{-1})	σ_{rms} (mK)	T_{MB}^{peak} (mK)	$\int T_{MB}\,dv$ (K km s^{-1})	*FWZI* (km s^{-1})	σ_{rms} (mK)	T_{MB}^{peak} (mK)	$\int T_{MB}\,dv$ (K km s^{-1})	*FWZI* (km s^{-1})
L1448-MM	12	330	19.31 ± 0.08	153	–	–	–	–	103	440	19.95 ± 0.68	147	22	189	10.83 ± 0.14	150
NGC 1333-IRAS2A	12	325	5.31 ± 0.05	69	123	724	8.83 ± 0.52	60	99	414	5.40 ± 0.40	54	11	210	4.40 ± 0.05	66
NGC 1333-IRAS4A	14	918	18.17 ± 0.08	93	118	850	24.12 ± 0.60	87	100	656	16.52 ± 0.46	72	10	362	11.45 ± 0.05	105
NGC 1333-IRAS4B	13	712	10.64 ± 0.06	75	118	1804	29.39 ± 0.58	81	105	1486	23.27 ± 0.54	90	10	724	12.52 ± 0.06	123
L1527	11	145	1.24 ± 0.04	42	–	–	–	–	109	<326	–	–	–	–	–	–
Ced110-IRS4	8	28	0.25 ± 0.02	24	–	–	–	–	124	<371	–	–	–	–	–	–
BHR71	12	445	9.77 ± 0.08	168	–	–	–	–	106	397	9.97 ± 0.71	147	–	–	–	–
IRAS 15398	8	215	2.05 ± 0.03	51	–	–	–	–	120	<358	–	–	–	–	–	–
L483	12	133	1.40 ± 0.04	45	–	–	–	–	102	332	3.14 ± 0.30	30	21	106	1.56 ± 0.08	48
Ser-SMM1	13	600	11.46 ± 0.07	99	126	2456	37.59 ± 0.55	63	107	1767	23.83 ± 0.38	42	14	1040	17.32 ± 0.08	96
Ser-SMM3	13	139	3.78 ± 0.07	108	123	476	5.23 ± 0.50	54	105	<315	–	–	20	95	1.57 ± 0.08	51
Ser-SMM4	12	484	8.59 ± 0.08	138	–	–	–	–	103	<309	–	–	20	157	3.24 ± 0.09	75
L723	11	129	0.70 ± 0.03	33	–	–	–	–	97	<291	–	–	–	–	–	–
B335	13	98	1.33 ± 0.06	66	–	–	–	–	96	<288	–	–	–	–	–	–
L1157	12	182	3.70 ± 0.07	93	–	–	–	–	105	<314	–	–	–	–	–	–
NGC 1333-IRAS3A	13	259	6.36 ± 0.07	96	–	–	–	–	–	–	–	–	–	–	–	–
L1489	11	74	1.03 ± 0.04	48	–	–	–	–	119	<356	–	–	–	–	–	–
L1551-IRS5	9	114	0.76 ± 0.04	48	–	–	–	–	124	<372	–	–	–	–	–	–
TMR1	8	40	0.32 ± 0.02	24	–	–	–	–	118	439	1.78 ± 0.34	27	–	–	–	–
TMC1A	8	<25	–	–	–	–	–	–	119	<356	–	–	–	–	–	–
TMC1	8	41	0.28 ± 0.02	30	–	–	–	–	122	<367	–	–	–	–	–	–
HH46-IRS	8	153	1.33 ± 0.03	57	–	–	–	–	136	<408	–	–	–	–	–	–
IRAS 12496	9	81	0.12 ± 0.04	69	–	–	–	–	122	423	1.24 ± 0.28	18	–	–	–	–
GSS30-IRS1	10	737	4.73 ± 0.04	42	–	–	–	–	119	498	4.48 ± 0.34	27	9	273	2.89 ± 0.03	42
Elias29	9	141	1.76 ± 0.04	60	–	–	–	–	123	503	3.05 ± 0.26	15	9	177	2.58 ± 0.03	42
Oph-IRS63	11	<32	–	–	–	–	–	–	120	<359	–	–	–	–	–	–
RNO91	10	65	0.53 ± 0.03	33	–	–	–	–	125	<375	–	–	–	–	–	–
RCrA-IRS5A	17	521	4.29 ± 0.07	51	–	–	–	–	–	–	–	–	–	–	–	–
HH100	10	508	2.56 ± 0.04	42	–	–	–	–	–	–	–	–	–	–	–	–

Table A.4. Observed properties of para-water line profiles.

Source	H_2O $1_{11}-0_{00}$				H_2O $2_{02}-1_{11}$				H_2O $2_{11}-2_{02}$			
	σ_{rms} (mK)	T_{MB}^{peak} (mK)	$\int T_{MB}\,dv$ (K km s^{-1})	$FWZI$ (km s^{-1})	σ_{rms} (mK)	T_{MB}^{peak} (mK)	$\int T_{MB}\,dv$ (K km s^{-1})	$FWZI$ (km s^{-1})	σ_{rms} (mK)	T_{MB}^{peak} (mK)	$\int T_{MB}\,dv$ (K km s^{-1})	$FWZI$ (km s^{-1})
L1448-MM	19	393	22.51 ± 0.13	156	23	408	25.13 ± 0.16	159	20	252	14.11 ± 0.13	144
NGC 1333-IRAS2A	19	369	5.44 ± 0.09	72	23	394	8.43 ± 0.10	69	21	266	6.69 ± 0.10	84
NGC 1333-IRAS4A	18	720	19.56 ± 0.11	108	23	771	22.60 ± 0.12	96	20	550	16.23 ± 0.10	96
NGC 1333-IRAS4B	18	1108	15.62 ± 0.10	102	22	1365	23.62 ± 0.12	96	21	855	13.99 ± 0.11	93
L1527	18	61	0.57 ± 0.06	30	22	82	1.05 ± 0.08	45	21	<62	–	–
Ced110-IRS4	25	<74	–	–	22	<66	–	–	18	<54	–	–
BHR71	19	202	9.94 ± 0.15	195	25	137	8.49 ± 0.18	183	18	129	5.65 ± 0.13	189
IRAS 15398	26	236	3.19 ± 0.09	36	22	201	2.59 ± 0.06	27	17	104	1.12 ± 0.06	48
L483	18	155	2.33 ± 0.08	60	23	149	2.65 ± 0.09	48	18	81	1.16 ± 0.07	48
Ser-SMM1	20	1263	21.74 ± 0.12	120	22	1606	27.66 ± 0.13	114	21	837	12.02 ± 0.08	48
Ser-SMM3	19	179	3.94 ± 0.10	93	22	202	6.06 ± 0.12	96	20	132	2.78 ± 0.11	102
Ser-SMM4	19	352	8.72 ± 0.10	93	23	330	8.06 ± 0.12	93	19	192	3.92 ± 0.09	75
L723	18	152	0.74 ± 0.06	39	21	168	1.17 ± 0.06	30	20	109	0.99 ± 0.07	45
B335	18	88	1.84 ± 0.08	66	23	120	1.83 ± 0.09	51	20	<59	–	–
L1157	20	165	5.17 ± 0.12	126	22	135	4.27 ± 0.14	135	20	74	0.32 ± 0.04	15
NGC 1333-IRAS3A	–	–	–	–	–	–	–	–	–	–	–	–
L1489	26	156	1.59 ± 0.10	48	22	135	1.30 ± 0.08	39	17	70	0.90 ± 0.05	33
L1551-IRS5	25	187	−0.08 ± 0.09	42	22	168	0.79 ± 0.06	21	17	102	0.44 ± 0.04	21
TMR1	25	82	0.89 ± 0.09	39	22	106	0.96 ± 0.07	33	17	54	0.43 ± 0.04	21
TMC1A	24	<71	–	–	22	<67	–	–	–	–	–	–
TMC1	25	<75	–	–	22	89	0.37 ± 0.05	18	–	–	–	–
HH46-IRS	24	91	0.46 ± 0.06	24	22	92	0.55 ± 0.06	27	16	51	0.41 ± 0.05	36
IRAS 12496	24	166	−0.49 ± 0.12	87	23	162	1.89 ± 0.10	60	18	83	0.19 ± 0.04	18
GSS30-IRS1	23	770	4.53 ± 0.09	48	22	1152	6.10 ± 0.07	36	18	647	3.14 ± 0.06	36
Elias29	24	323	3.28 ± 0.09	42	23	369	4.11 ± 0.09	51	17	189	2.89 ± 0.08	66
Oph-IRS63	24	<74	–	–	23	<69	–	–	18	<53	–	–
RNO91	25	<76	–	–	22	74	0.49 ± 0.06	21	18	<53	–	–
RCrA-IRS5A	–	–	–	–	–	–	–	–	–	–	–	–
HH100	–	–	–	–	–	–	–	–	–	–	–	–

Table A.5. Observed properties of $H_2^{18}O$ line profiles.

Source	$H_2^{18}O$ $1_{10}-1_{01}$				$H_2^{18}O$ $3_{12}-3_{03}$				$H_2^{18}O$ $1_{11}-0_{00}$				$H_2^{18}O$ $2_{02}-1_{11}$			
	σ_{rms} (mK)	T_{MB}^{peak} (mK)	$\int T_{MB}\,dv$ (K km s^{-1})	*FWZI* (km s^{-1})	σ_{rms} (mK)	T_{MB}^{peak} (mK)	$\int T_{MB}\,dv$ (K km s^{-1})	*FWZI* (km s^{-1})	σ_{rms} (mK)	T_{MB}^{peak} (mK)	$\int T_{MB}\,dv$ (K km s^{-1})	*FWZI* (km s^{-1})	σ_{rms} (mK)	T_{MB}^{peak} (mK)	$\int T_{MB}\,dv$ (K km s^{-1})	*FWZI* (km s^{-1})
L1448-MM	4	<13	–	–	21	<62	–	–	18	<54	–	–	–	–	–	–
NGC 1333-IRAS2A	4	<10	–	–	8	27	0.09 ± 0.02	12	19	<56	–	–	16	<49	–	–
NGC 1333-IRAS4A	4	68	0.46 ± 0.01	45	8	<25	–	–	17	<52	–	–	–	–	–	–
NGC 1333-IRAS4B	4	30	0.41 ± 0.01	48	8	<25	–	–	17	<50	–	–	16	<48	–	–
L1527	3	<10	–	–	–	–	–	–	18	<54	–	–	–	–	–	–
Ced110-IRS4	–	–	–	–	–	–	–	–	26	<79	–	–	–	–	–	–
BHR71	3	<9	–	–	–	–	–	–	18	<54	–	–	–	–	–	–
IRAS 15398	–	–	–	–	–	–	–	–	26	<78	–	–	–	–	–	–
L483	5	<14	–	–	22	<65	–	–	18	<53	–	–	–	–	–	–
Ser-SMM1	3	25	0.18 ± 0.01	30	8	26	0.12 ± 0.02	12	18	50	−0.31 ± 0.04	16	18	<53	–	–
Ser-SMM3	5	<14	–	–	20	<62	–	–	17	<52	–	–	–	–	–	–
Ser-SMM4	4	<11	–	–	22	<65	–	–	18	<53	–	–	–	–	–	–
L723	4	<13	–	–	–	–	–	–	18	<53	–	–	–	–	–	–
B335	4	<13	–	–	–	–	–	–	17	<51	–	–	–	–	–	–
L1157	4	<13	–	–	–	–	–	–	18	<54	–	–	–	–	–	–
NGC 1333-IRAS3A	–	–	–	–	–	–	–	–	–	–	–	–	–	–	–	–
L1489	–	–	–	–	–	–	–	–	26	<77	–	–	–	–	–	–
L1551-IRS5	–	–	–	–	–	–	–	–	25	<76	–	–	–	–	–	–
TMR1	–	–	–	–	–	–	–	–	26	<77	–	–	–	–	–	–
TMC1A	–	–	–	–	–	–	–	–	27	<80	–	–	–	–	–	–
TMC1	–	–	–	–	–	–	–	–	27	<80	–	–	–	–	–	–
HH46-IRS	–	–	–	–	–	–	–	–	24	<74	–	–	–	–	–	–
IRAS 12496	–	–	–	–	–	–	–	–	22	<67	–	–	–	–	–	–
GSS30-IRS1	–	–	–	–	8	<24	–	–	26	<78	–	–	–	–	–	–
Elias29	4	<11	–	–	8	25	0.16 ± 0.02	33	25	<76	–	–	–	–	–	–
Oph-IRS63	–	–	–	–	–	–	–	–	25	<75	–	–	–	–	–	–
RNO91	–	–	–	–	–	–	–	–	26	<78	–	–	–	–	–	–
RCrA-IRS5A	–	–	–	–	–	–	–	–	–	–	–	–	–	–	–	–
HH100	–	–	–	–	–	–	–	–	–	–	–	–	–	–	–	–

Table A.6. Gaussian decomposition results.

Source	Comp.[a]	*FWHM*	v_{peak}	v_{source}	H_2O $1_{10}-1_{01}$		H_2O $2_{12}-1_{01}$		H_2O $3_{12}-2_{21}$		H_2O $3_{12}-3_{03}$	
					T_{MB}^{peak}	$\int T_{MB}\,dv$	T_{MB}^{peak}	$\int T_{MB}\,dv$	T_{MB}^{peak}	$\int T_{MB}\,dv$	T_{MB}^{peak}	$\int T_{MB}\,dv$
		(km s^{-1})	(km s^{-1})	(km s^{-1})	(K)	(K km s^{-1})	(K)	(K km s^{-1})	(K)	(K km s^{-1})	(K)	(Kkm s^{-1})
L1448-MM	S	7.8 ± 0.8	4.6 ± 0.3	5.2	−0.12 ± 0.02	−1.01 ± 0.21	–	–	<0.26	<5.02	−0.07 ± 0.02	−0.59 ± 0.17
	S	23.0 ± 1.7	59.6 ± 0.7	5.2	0.12 ± 0.01	3.00 ± 0.37	–	–	0.15 ± 0.03	3.71 ± 0.73	0.07 ± 0.01	1.82 ± 0.28
	S	39.8 ± 3.7	−41.5 ± 1.6	5.2	0.08 ± 0.01	3.20 ± 0.46	–	–	0.19 ± 0.02	7.88 ± 1.18	0.06 ± 0.01	2.68 ± 0.40
	C	44.6 ± 2.0	16.8 ± 0.7	5.2	0.30 ± 0.01	14.25 ± 0.79	–	–	0.18 ± 0.02	8.70 ± 1.02	0.15 ± 0.01	6.99 ± 0.50
IRAS2A	E	4.9 ± 0.8	8.0 ± 0.3	7.7	–[b]	–[b]	–[b]	–[b]	<0.20	<2.39	0.10 ± 0.01	0.49 ± 0.11
	C	14.0 ± 0.7	11.5 ± 0.3	7.7	0.17 ± 0.01	2.57 ± 0.24	0.30 ± 0.11	4.49 ± 1.63	0.25 ± 0.04	3.68 ± 0.65	0.10 ± 0.01	1.55 ± 0.19
	S	39.2 ± 2.3	−5.4 ± 1.3	7.7	0.07 ± 0.01	2.92 ± 0.18	0.19 ± 0.07	7.93 ± 0.48	<0.20	<19.30	0.07 ± 0.01	2.92 ± 0.18
IRAS4A	S	9.9 ± 0.4	−0.8 ± 0.1	7.2	0.31 ± 0.03	3.21 ± 0.34	0.29 ± 0.08	3.01 ± 0.81	0.11 ± 0.06	1.14 ± 0.59	0.12 ± 0.01	1.25 ± 0.15
	S	18.0 ± 1.6	8.4 ± 0.8	7.2	0.23 ± 0.02	4.43 ± 0.58	<0.26	<11.55	0.04 ± 0.07	0.76 ± 1.26	0.08 ± 0.01	1.46 ± 0.29
	C	41.4 ± 0.7	9.9 ± 0.3	7.2	0.26 ± 0.02	11.52 ± 0.75	0.52 ± 0.04	22.74 ± 1.84	0.34 ± 0.05	14.84 ± 2.01	0.20 ± 0.01	8.72 ± 0.50
IRAS4B	E	2.6 ± 0.1	8.1 ± 0.0	7.4	−1.03 ± 0.07	−2.86 ± 0.23	−2.49 ± 0.34	−6.92 ± 0.99	<0.20	<1.31	<0.03	<0.21
	S	5.1 ± 0.2	8.6 ± 0.1	7.4	0.55 ± 0.07	2.98 ± 0.41	1.06 ± 0.30	5.75 ± 1.62	0.45 ± 0.11	2.47 ± 0.60	0.35 ± 0.02	1.93 ± 0.12
	C	24.6 ± 0.4	8.0 ± 0.1	7.4	0.40 ± 0.01	10.40 ± 0.34	0.97 ± 0.06	25.44 ± 1.74	0.80 ± 0.05	21.06 ± 1.37	0.39 ± 0.01	10.08 ± 0.31
L1527	C	20.2 ± 3.8	5.3 ± 1.5	5.9	0.05 ± 0.01	1.14 ± 0.33	–	–	<0.20	<10.10	–	–
Ced110-IRS4	C	15.7 ± 3.7	5.3 ± 1.4	4.2	0.02 ± 0.01	0.36 ± 0.12	–	–	<0.23	<9.06	–	–
BHR71	S	6.4 ± 2.3	−11.8 ± 0.9	−4.4	0.05 ± 0.02	0.35 ± 0.17	–	–	0.07 ± 0.07	0.51 ± 0.52	–	–
	S	28.3 ± 4.5	59.0 ± 1.9	−4.4	0.04 ± 0.01	1.08 ± 0.26	–	–	0.05 ± 0.03	1.40 ± 0.95	–	–
	C	52.3 ± 3.9	−1.1 ± 1.6	−4.4	0.13 ± 0.01	7.12 ± 0.71	–	–	0.09 ± 0.03	4.78 ± 1.58	–	–
	S	59.0 ± 14.3	−57.4 ± 7.6	−4.4	0.01 ± 0.01	0.86 ± 0.43	–	–	0.06 ± 0.02	3.71 ± 1.66	–	–
IRAS 15398	C	16.3 ± 0.6	−0.4 ± 0.3	5.1	0.09 ± 0.01	1.59 ± 0.12	–	–	<0.22	<8.99	–	–
L483	C	18.5 ± 0.9	3.2 ± 0.4	5.2	0.08 ± 0.01	1.61 ± 0.15	–	–	0.15 ± 0.03	2.93 ± 0.55	0.07 ± 0.01	1.41 ± 0.18
Ser-SMM1	E	2.7 ± 0.1	8.6 ± 0.0	8.5	−0.65 ± 0.04	−1.86 ± 0.14	−3.30 ± 0.32	−9.51 ± 1.00	<0.19	<1.26	<0.04	<0.25
	S	3.7 ± 0.3	4.4 ± 0.1	8.5	0.09 ± 0.04	0.36 ± 0.16	0.26 ± 0.29	1.02 ± 1.14	0.55 ± 0.17	2.16 ± 0.72	0.37 ± 0.04	1.45 ± 0.20
	C	18.9 ± 0.4	7.0 ± 0.1	8.5	0.43 ± 0.04	8.55 ± 0.86	2.07 ± 0.15	41.72 ± 3.24	1.17 ± 0.08	23.56 ± 1.69	0.72 ± 0.02	14.40 ± 0.53
	S	41.1 ± 5.4	24.2 ± 4.2	8.5	0.10 ± 0.01	4.55 ± 0.89	<0.29	<29.60	<0.19	<19.07	<0.04	<3.78
Ser-SMM3	S	9.2 ± 1.1	4.7 ± 0.5	7.6	−0.11 ± -0.01	−1.07 ± 0.12	−0.14 ± -0.02	−1.36 ± 0.16	<0.19	<4.45	0.02 ± 0.00	0.19 ± 0.02
	C	30.1 ± 1.6	15.6 ± 0.8	7.6	0.10 ± 0.01	3.26 ± 0.28	0.22 ± 0.03	7.21 ± 1.17	<0.19	<14.63	0.05 ± 0.01	1.51 ± 0.22
	S	40.4 ± 6.9	−24.6 ± 3.1	7.6	0.04 ± 0.00	1.93 ± 0.39	<0.26	<26.59	<0.19	<19.62	<0.05	<5.16
Ser-SMM4	S	10.7 ± 1.3	1.9 ± 0.5	8.0	<0.04	<1.02	–	–	<0.18	<4.87	0.07 ± 0.02	0.80 ± 0.21
	C	46.1 ± 1.4	−0.3 ± 0.5	8.0	0.15 ± 0.01	7.47 ± 0.35	–	–	<0.18	<20.98	0.05 ± 0.01	2.53 ± 0.42
L723	E	4.5 ± 1.0	10.7 ± 0.4	11.2	–[b]	–[b]	–	–	<0.20	<2.18	–	–
	C	24.9 ± 3.9	12.6 ± 1.6	11.2	0.03 ± 0.01	0.72 ± 0.18	–	–	<0.20	<12.20	–	–
B335	E	4.2 ± 1.7	9.9 ± 0.7	8.4	0.04 ± 0.02	0.17 ± 0.10	–	–	<0.16	<1.71	–	–
	S	6.5 ± 2.6	17.3 ± 1.0	8.4	<0.05	<0.75	–	–	<0.16	<2.66	–	–
	C	40.9 ± 4.5	7.9 ± 1.9	8.4	0.03 ± 0.01	1.15 ± 0.26	–	–	<0.16	<16.64	–	–
L1157	C	23.2 ± 2.5	5.4 ± 0.9	2.6	0.10 ± 0.01	2.49 ± 0.35	–	–	<0.21	<11.93	–	–
	S	35.7 ± 8.7	39.2 ± 3.9	2.6	0.02 ± 0.00	0.73 ± 0.24	–	–	<0.21	<18.38	–	–
	S	47.7 ± 19.1	−22.7 ± 10.9	2.6	0.01 ± 0.00	0.61 ± 0.34	–	–	<0.21	<24.56	–	–

Notes. [(a)] Component type: E = envelope, C = cavity shock and S = spot shock. [(b)] Non-Gaussian combination of absorption and emission so excluded from fit.

Table A.7. Gaussian decomposition results.

Source	Comp.[a]	*FWHM*	v_{peak}	v_{source}	H_2O $1_{11}-0_{00}$		H_2O $2_{02}-1_{11}$		H_2O $2_{11}-2_{02}$	
					T_{MB}^{peak}	$\int T_{MB}\,dv$	T_{MB}^{peak}	$\int T_{MB}\,dv$	T_{MB}^{peak}	$\int T_{MB}\,dv$
		(km s^{-1})	(km s^{-1})	(km s^{-1})	(K)	(K km s^{-1})	(K)	(K km s^{-1})	(K)	(K km s^{-1})
L1448-MM	S	7.8 ± 0.8	4.6 ± 0.3	5.2	−0.27 ± 0.03	−2.20 ± 0.34	−0.21 ± 0.04	−1.75 ± 0.37	−0.12 ± 0.03	−1.00 ± 0.30
	S	23.0 ± 1.7	59.6 ± 0.7	5.2	0.18 ± 0.02	4.46 ± 0.51	0.21 ± 0.02	5.23 ± 0.54	0.10 ± 0.01	2.39 ± 0.40
	S	39.8 ± 3.7	−41.5 ± 1.6	5.2	0.09 ± 0.01	3.83 ± 0.59	0.11 ± 0.01	4.65 ± 0.64	0.07 ± 0.01	2.87 ± 0.54
	C	44.6 ± 2.0	16.8 ± 0.7	5.2	0.36 ± 0.01	17.02 ± 0.99	0.35 ± 0.01	16.81 ± 0.97	0.21 ± 0.01	9.98 ± 0.73
IRAS2A	E	4.9 ± 0.8	8.0 ± 0.3	7.7	–[b]	–[b]	<0.06	<0.76	0.07 ± 0.03	0.38 ± 0.18
	C	14.0 ± 0.7	11.5 ± 0.3	7.7	0.17 ± 0.02	2.56 ± 0.32	0.25 ± 0.02	3.69 ± 0.31	0.14 ± 0.02	2.10 ± 0.32
	S	39.2 ± 2.3	−5.4 ± 1.3	7.7	0.11 ± 0.01	4.59 ± 0.28	0.12 ± 0.01	5.01 ± 0.30	0.09 ± 0.03	3.76 ± 0.23
IRAS4A	S	9.9 ± 0.4	−0.8 ± 0.1	7.2	0.39 ± 0.02	4.13 ± 0.24	0.34 ± 0.02	3.62 ± 0.28	0.13 ± 0.03	1.35 ± 0.33
	S	18.0 ± 1.6	8.4 ± 0.8	7.2	<0.05	<2.29	0.13 ± 0.03	2.48 ± 0.57	0.22 ± 0.02	4.14 ± 0.57
	C	41.4 ± 0.7	9.9 ± 0.3	7.2	0.38 ± 0.01	16.73 ± 0.53	0.38 ± 0.02	16.67 ± 0.90	0.24 ± 0.02	10.61 ± 0.84
IRAS4B	E	2.6 ± 0.1	8.1 ± 0.0	7.4	−1.75 ± 0.12	−4.87 ± 0.37	<0.06	<0.37	<0.07	<0.43
	S	5.1 ± 0.2	8.6 ± 0.1	7.4	0.93 ± 0.12	5.06 ± 0.66	0.63 ± 0.03	3.44 ± 0.22	0.37 ± 0.04	2.00 ± 0.21
	C	24.6 ± 0.4	8.0 ± 0.1	7.4	0.54 ± 0.02	14.23 ± 0.48	0.70 ± 0.02	18.45 ± 0.56	0.41 ± 0.02	10.84 ± 0.49
L1527	C	20.2 ± 3.8	5.3 ± 1.5	5.9	0.03 ± 0.01	0.71 ± 0.32	0.04 ± 0.01	0.91 ± 0.35	<0.06	<3.15
Ced110-IRS4	C	15.7 ± 3.7	5.3 ± 1.4	4.2	<0.06	<2.56	<0.06	<2.38	<0.05	<1.99
BHR71	S	6.4 ± 2.3	−11.8 ± 0.9	−4.4	<0.05	<0.86	<0.08	<1.22	0.03 ± 0.02	0.20 ± 0.16
	S	28.3 ± 4.5	59.0 ± 1.9	−4.4	0.05 ± 0.01	1.46 ± 0.35	0.04 ± 0.01	1.35 ± 0.41	0.04 ± 0.01	1.14 ± 0.34
	C	52.3 ± 3.9	−1.1 ± 1.6	−4.4	0.12 ± 0.01	6.46 ± 0.70	0.09 ± 0.01	5.27 ± 0.85	0.05 ± 0.01	2.95 ± 0.52
	S	59.0 ± 14.3	−57.4 ± 7.6	−4.4	0.03 ± 0.01	1.99 ± 0.65	0.04 ± 0.01	2.71 ± 0.86	0.02 ± 0.01	1.22 ± 0.52
IRAS 15398	C	16.3 ± 0.6	−0.4 ± 0.3	5.1	0.19 ± 0.01	3.35 ± 0.25	0.16 ± 0.01	2.76 ± 0.18	0.07 ± 0.01	1.27 ± 0.12
L483	C	18.5 ± 0.9	3.2 ± 0.4	5.2	0.13 ± 0.01	2.46 ± 0.23	0.12 ± 0.01	2.44 ± 0.21	0.05 ± 0.01	0.99 ± 0.17
Ser-SMM1	E	2.7 ± 0.1	8.6 ± 0.0	8.5	−1.72 ± 0.08	−4.96 ± 0.30	−0.40 ± 0.08	−1.16 ± 0.22	0.24 ± 0.07	0.69 ± 0.20
	S	3.7 ± 0.3	4.4 ± 0.1	8.5	0.28 ± 0.07	1.11 ± 0.29	0.51 ± 0.07	2.00 ± 0.33	0.31 ± 0.06	1.23 ± 0.27
	C	18.9 ± 0.4	7.0 ± 0.1	8.5	0.95 ± 0.06	19.17 ± 1.20	1.09 ± 0.05	22.02 ± 1.11	0.53 ± 0.03	10.72 ± 0.72
	S	41.1 ± 5.4	24.2 ± 4.2	8.5	0.11 ± 0.02	4.90 ± 1.20	0.08 ± 0.02	3.69 ± 1.09	<0.06	<6.28
Ser-SMM3	S	9.2 ± 1.1	4.7 ± 0.5	7.6	−0.10 ± -0.01	−0.97 ± 0.11	0.05 ± 0.01	0.49 ± 0.06	0.04 ± 0.01	0.39 ± 0.04
	C	30.1 ± 1.6	15.6 ± 0.8	7.6	0.13 ± 0.01	4.02 ± 0.32	0.14 ± 0.01	4.34 ± 0.34	0.06 ± 0.01	1.93 ± 0.28
	S	40.4 ± 6.9	−24.6 ± 3.1	7.6	0.03 ± 0.01	1.48 ± 0.35	0.03 ± 0.01	1.21 ± 0.35	0.01 ± 0.01	0.61 ± 0.32
Ser-SMM4	S	10.7 ± 1.3	1.9 ± 0.5	8.0	0.12 ± 0.03	1.37 ± 0.34	0.16 ± 0.02	1.77 ± 0.31	0.07 ± 0.02	0.76 ± 0.21
	C	46.1 ± 1.4	−0.3 ± 0.5	8.0	0.17 ± 0.01	8.30 ± 0.56	0.13 ± 0.01	6.53 ± 0.60	0.06 ± 0.01	3.19 ± 0.43
L723	E	4.5 ± 1.0	10.7 ± 0.4	11.2	–[b]	–[b]	0.12 ± 0.02	0.56 ± 0.16	0.04 ± 0.02	0.19 ± 0.11
	C	24.9 ± 3.9	12.6 ± 1.6	11.2	0.03 ± 0.01	0.86 ± 0.26	0.02 ± 0.01	0.65 ± 0.29	0.03 ± 0.01	0.71 ± 0.28
B335	E	4.2 ± 1.7	9.9 ± 0.7	8.4	–[b]	–[b]	0.05 ± 0.02	0.20 ± 0.12	<0.06	<0.63
	S	6.5 ± 2.6	17.3 ± 1.0	8.4	<0.05	<0.82	0.06 ± 0.02	0.40 ± 0.20	<0.06	<0.98
	C	40.9 ± 4.5	7.9 ± 1.9	8.4	0.04 ± 0.01	1.95 ± 0.31	0.03 ± 0.01	1.36 ± 0.37	<0.06	<6.12
L1157	C	23.2 ± 2.5	5.4 ± 0.9	2.6	0.09 ± 0.02	2.24 ± 0.63	0.07 ± 0.02	1.72 ± 0.51	<0.06	<3.59
	S	35.7 ± 8.7	39.2 ± 3.9	2.6	0.04 ± 0.01	1.46 ± 0.45	0.03 ± 0.01	1.24 ± 0.40	<0.06	<5.53
	S	47.7 ± 19.1	−22.7 ± 10.9	2.6	0.03 ± 0.01	1.72 ± 0.78	0.03 ± 0.01	1.40 ± 0.65	<0.06	<7.39

Notes. [a] Component type: E = envelope, C = cavity shock and S = spot shock. [b] Non-Gaussian combination of absorption and emission so excluded from fit.

Table A.8. Gaussian decomposition results.

Source	Comp.[a]	*FWHM*	v_{peak}	v_{source}	H_2O 1_{10}-1_{01}		H_2O $2_{12}-1_{01}$		H_2O $3_{12}-2_{21}$		H_2O $3_{12}-3_{03}$	
					T_{MB}^{peak}	$\int T_{MB}\,dv$	T_{MB}^{peak}	$\int T_{MB}\,dv$	T_{MB}^{peak}	$\int T_{MB}\,dv$	T_{MB}^{peak}	$\int T_{MB}\,dv$
		(km s^{-1})	(km s^{-1})	(km s^{-1})	(K)	(K km s^{-1})	(K)	(K km s^{-1})	(K)	(K km s^{-1})	(K)	(Kkm s^{-1})
IRAS3A	E	1.5 ± 0.1	8.8 ± 0.0	8.5	−0.20 ± 0.01	−0.31 ± 0.03	–	–	–	–	–	–
	S	6.1 ± 0.3	5.4 ± 0.1	8.5	−0.19 ± 0.00	−1.23 ± 0.06	–	–	–	–	–	–
	C	28.8 ± 0.3	5.9 ± 0.1	8.5	0.26 ± 0.00	8.11 ± 0.14	–	–	–	–	–	–
L1489	C	20.0 ± 1.5	3.7 ± 0.6	7.2	0.04 ± 0.00	0.93 ± 0.12	–	–	<0.22	<11.27	–	–
L1551-IRS5	E	4.3 ± 0.8	6.7 ± 0.3	6.2	–[b]	–[b]	–	–	<0.24	<2.54	–	–
	C	26.1 ± 6.3	19.2 ± 3.0	6.2	0.02 ± 0.01	0.65 ± 0.21	–	–	<0.24	<15.52	–	–
TMR1	E	1.6 ± 0.6	6.2 ± 0.2	6.3	−0.03 ± 0.01	−0.06 ± 0.03	–	–	<0.23	<0.94	–	–
	C	13.0 ± 1.5	5.6 ± 0.6	6.3	0.03 ± 0.01	0.40 ± 0.09	–	–	0.11 ± 0.03	1.51 ± 0.49	–	–
TMC1A	–	–	–	–	–	–	–	–	–	–	–	–
TMC1	C	12.7 ± 2.6	5.6 ± 1.1	5.2	0.02 ± 0.00	0.26 ± 0.07	–	–	<0.22	<6.89	–	–
HH46-IRS	C	23.5 ± 2.1	10.5 ± 1.1	5.2	0.05 ± 0.01	1.24 ± 0.17	–	–	<0.24	<14.03	–	–
IRAS 12496	E	4.5 ± 0.8	3.5 ± 0.4	3.1	–[b]	–[b]	–	–	<0.23	<2.62	–	–
	C	25.5 ± 4.4	−2.0 ± 2.2	3.1	0.02 ± 0.00	0.43 ± 0.13	–	–	<0.23	<14.78	–	–
	S	25.7 ± 5.5	−31.9 ± 2.2	3.1	−0.01 ± 0.00	−0.36 ± 0.12	–	–	<0.23	<14.89	–	–
GSS30-IRS1	E	2.6 ± 0.1	3.0 ± 0.0	3.5	–[b]	–[b]	–	–	<0.21	<1.38	0.16 ± 0.02	0.45 ± 0.06
	C	14.5 ± 0.4	2.2 ± 0.2	3.5	0.24 ± 0.01	3.77 ± 0.20	–	–	0.30 ± 0.04	4.64 ± 0.69	0.17 ± 0.01	2.62 ± 0.15
Elias29	C	13.5 ± 0.4	5.2 ± 0.2	4.3	0.14 ± 0.01	1.99 ± 0.20	–	–	0.25 ± 0.05	3.64 ± 0.68	0.19 ± 0.01	2.73 ± 0.13
Oph-IRS63	–	–	–	–	–	–	–	–	–	–	–	–
RNO91	S	4.4 ± 1.0	4.0 ± 0.4	0.5	0.05 ± 0.01	0.23 ± 0.07	–	–	<0.24	<2.66	–	–
	C	6.0 ± 2.7	0.5 ± 1.1	0.5	<0.03	<0.50	–	–	<0.24	<3.64	–	–
RCrA-IRS5A	E	4.0 ± 0.1	6.7 ± 0.0	5.7	0.32 ± 0.01	1.36 ± 0.05	–	–	–	–	–	–
	C	19.8 ± 0.6	8.5 ± 0.2	5.7	0.13 ± 0.01	2.79 ± 0.15	–	–	–	–	–	–
HH100	C	16.1 ± 0.5	3.8 ± 0.2	5.6	0.08 ± 0.00	1.45 ± 0.06	–	–	–	–	–	–

Notes. [(a)] Component type: E = envelope, C = cavity shock and S = spot shock. [(b)] Non-Gaussian combination of absorption and emission so excluded from fit.

Table A.9. Gaussian decomposition results.

Source	Comp.[a]	*FWHM*	v_{peak}	v_{source}	H_2O $1_{11}-0_{00}$		H_2O $2_{02}-1_{11}$		H_2O $2_{11}-2_{02}$	
					T_{MB}^{peak}	$\int T_{MB}\,dv$	T_{MB}^{peak}	$\int T_{MB}\,dv$	T_{MB}^{peak}	$\int T_{MB}\,dv$
		(km s^{-1})	(km s^{-1})	(km s^{-1})	(K)	(K km s^{-1})	(K)	(K km s^{-1})	(K)	(K km s^{-1})
IRAS3A	E	1.5 ± 0.1	8.8 ± 0.0	8.5	–	–	–	–	–	–
	S	6.1 ± 0.3	5.4 ± 0.1	8.5	–	–	–	–	–	–
	C	28.8 ± 0.3	5.9 ± 0.1	8.5	–	–	–	–	–	–
L1489	C	20.0 ± 1.5	3.7 ± 0.6	7.2	0.07 ± 0.01	1.42 ± 0.20	0.07 ± 0.01	1.46 ± 0.20	0.05 ± 0.01	0.96 ± 0.15
L1551-IRS5	E	4.3 ± 0.8	6.7 ± 0.3	6.2	–[b]	–[b]	0.13 ± 0.02	0.59 ± 0.15	0.07 ± 0.02	0.34 ± 0.10
	C	26.1 ± 6.3	19.2 ± 3.0	6.2	0.02 ± 0.01	0.66 ± 0.34	<0.06	<4.25	<0.06	<3.65
TMR1	E	1.6 ± 0.6	6.2 ± 0.2	6.3	−0.09 ± 0.04	−0.15 ± 0.09	<0.07	<0.27	<0.05	<0.20
	C	13.0 ± 1.5	5.6 ± 0.6	6.3	0.05 ± 0.01	0.74 ± 0.21	0.07 ± 0.01	0.97 ± 0.18	0.04 ± 0.01	0.49 ± 0.11
TMC1A	–	–	–	–	–	–	–	–	–	–
TMC1	C	12.7 ± 2.6	5.6 ± 1.1	5.2	<0.07	<2.10	0.03 ± 0.01	0.41 ± 0.14	–	–
HH46-IRS	C	23.5 ± 2.1	10.5 ± 1.1	5.2	<0.06	<3.79	<0.06	<3.70	0.02 ± 0.01	0.49 ± 0.14
IRAS 12496	E	4.5 ± 0.8	3.5 ± 0.4	3.1	–[b]	–[b]	0.11 ± 0.02	0.53 ± 0.14	0.05 ± 0.01	0.25 ± 0.08
	C	25.5 ± 4.4	−2.0 ± 2.2	3.1	0.03 ± 0.01	0.69 ± 0.30	0.04 ± 0.01	1.09 ± 0.19	<0.05	<3.41
	S	25.7 ± 5.5	−31.9 ± 2.2	3.1	−0.04 ± 0.01	−1.17 ± 0.35	0.02 ± 0.01	0.55 ± 0.25	<0.05	<3.44
GSS30-IRS1	E	2.6 ± 0.1	3.0 ± 0.0	3.5	–[b]	–[b]	0.78 ± 0.04	2.20 ± 0.15	0.43 ± 0.03	1.22 ± 0.11
	C	14.5 ± 0.4	2.2 ± 0.2	3.5	0.30 ± 0.02	4.62 ± 0.32	0.25 ± 0.02	3.86 ± 0.31	0.12 ± 0.01	1.84 ± 0.23
Elias29	C	13.5 ± 0.4	5.2 ± 0.2	4.3	0.26 ± 0.03	3.77 ± 0.39	0.28 ± 0.01	3.97 ± 0.23	0.16 ± 0.01	2.24 ± 0.17
Oph-IRS63	–	–	–	–	–	–	–	–	–	–
RNO91	S	4.4 ± 1.0	4.0 ± 0.4	0.5	0.06 ± 0.02	0.26 ± 0.12	<0.07	<0.76	<0.06	<0.64
	C	6.0 ± 2.7	0.5 ± 1.1	0.5	<0.08	<1.24	0.05 ± 0.02	0.30 ± 0.18	<0.06	<0.87
RCrA-IRS5A	E	4.0 ± 0.1	6.7 ± 0.0	5.7	–	–	–	–	–	–
	C	19.8 ± 0.6	8.5 ± 0.2	5.7	–	–	–	–	–	–
HH100	C	16.1 ± 0.5	3.8 ± 0.2	5.6	–	–	–	–	–	–

Notes. [(a)] Component type: E = envelope, C = cavity shock and S = spot shock. [(b)] Non-Gaussian combination of absorption and emission so excluded from fit.

Table A.10. Gaussian decomposition results.

Source	Comp.[a]	*FWHM*	v_{peak}	v_{source}	$H_2^{18}O$ $1_{10}-1_{01}$		$H_2^{18}O$ $3_{12}-3_{03}$		$H_2^{18}O$ $1_{11}-0_{00}$		$H_2^{18}O$ $2_{02}-1_{11}$	
					T_{MB}^{peak}	$\int T_{MB}\,dv$	T_{MB}^{peak}	$\int T_{MB}\,dv$	T_{MB}^{peak}	$\int T_{MB}\,dv$	T_{MB}^{peak}	$\int T_{MB}\,dv$
		(km s^{-1})	(km s^{-1})	(km s^{-1})	(K)	(K km s^{-1})	(K)	(K km s^{-1})	(K)	(K km s^{-1})	(K)	(Kkm s^{-1})
IRAS2A	E	4.9 ± 0.8	8.0 ± 0.3	7.7	<0.011	<0.139	0.015 ± 0.008	0.079 ± 0.045	<0.056	<0.684	<0.048	<0.585
	C	14.0 ± 0.7	11.5 ± 0.3	7.7	<0.011	<0.399	<0.023	<0.802	<0.056	<1.966	<0.048	<1.681
	S	39.2 ± 2.3	−5.4 ± 1.3	7.7	<0.011	<1.121	<0.023	<2.252	<0.056	<5.517	<0.048	<4.718
IRAS4A	S	9.9 ± 0.4	−0.8 ± 0.1	7.2	<0.012	<0.304	<0.021	<0.513	<0.048	<1.181	–	–
	S	18.0 ± 1.6	8.4 ± 0.8	7.2	0.022 ± 0.003	0.428 ± 0.071	<0.021	<0.935	<0.048	<2.151	–	–
	C	41.4 ± 0.7	9.9 ± 0.3	7.2	<0.012	<1.276	<0.021	<2.156	<0.048	<4.958	–	–
IRAS4B	E	2.6 ± 0.1	8.1 ± 0.0	7.4	<0.013	<0.084	<0.023	<0.150	<0.047	<0.307	<0.041	<0.268
	S	5.1 ± 0.2	8.6 ± 0.1	7.4	<0.013	<0.163	<0.023	<0.292	<0.047	<0.599	<0.041	<0.524
	C	24.6 ± 0.4	8.0 ± 0.1	7.4	0.016 ± 0.003	0.427 ± 0.065	<0.023	<1.410	<0.047	<2.885	<0.041	<2.523
Ser-SMM1	E	2.7 ± 0.1	8.6 ± 0.0	8.5	−0.054 ± 0.016	−0.156 ± 0.048	0.022 ± 0.019	0.064 ± 0.055	−0.223 ± 0.051	−0.642 ± 0.150	<0.045	<0.309
	S	3.7 ± 0.3	4.4 ± 0.1	8.5	<0.016	<0.146	<0.021	<0.200	<0.049	<0.459	<0.045	<0.423
	C	18.9 ± 0.4	7.0 ± 0.1	8.5	0.019 ± 0.006	0.378 ± 0.125	<0.021	<1.018	0.018 ± 0.019	0.359 ± 0.391	<0.045	<2.157
	S	41.1 ± 5.4	24.2 ± 4.2	8.5	<0.016	<1.623	<0.021	<2.212	<0.049	<5.085	<0.045	<4.689
Elias29	C	13.5 ± 0.4	5.2 ± 0.2	4.3	<0.011	<0.376	0.010 ± 0.004	0.142 ± 0.060	<0.068	<2.310	–	–

Notes. [(a)] Component type: E = envelope, C = cavity shock and S = spot shock.

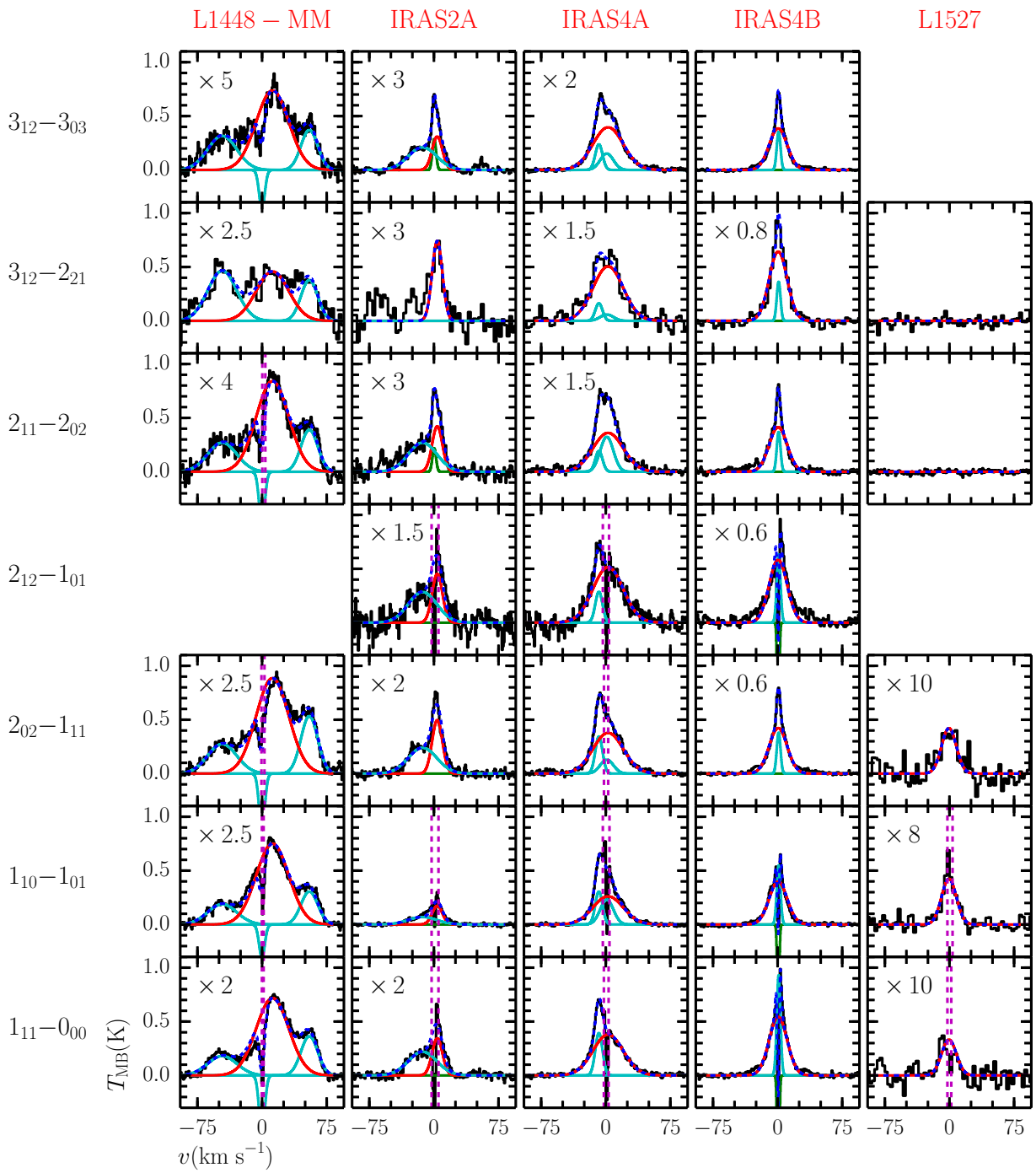

Fig. A.1. Observed H_2O spectra for Class 0 sources in the WISH sample. All spectra are continuum-subtracted and have been recentred so that the source velocity is at 0 km s^{-1} for ease of comparison. Some spectra have also been resampled to a lower velocity resolution for ease of comparison. The red, cyan and green lines show the individual Gaussian components for the cavity shock, spot shocks, and quiescent envelope respectively (see text and Table 3 for details) while the blue dashed line shows the combined fit for each line. The vertical dashed magenta lines indicate regions which are masked during the fitting.

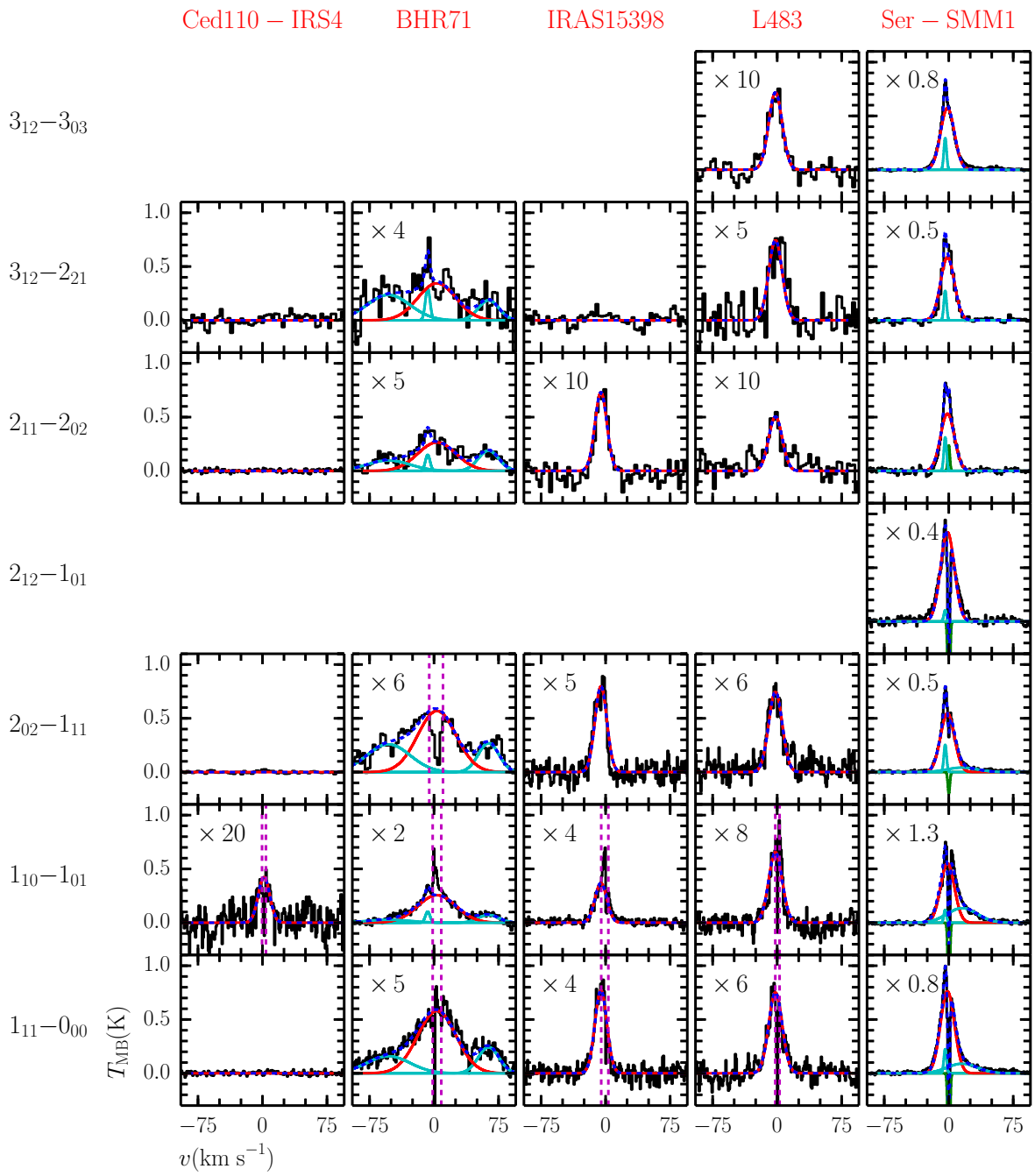

Fig. A.2. As in Fig. A.1.

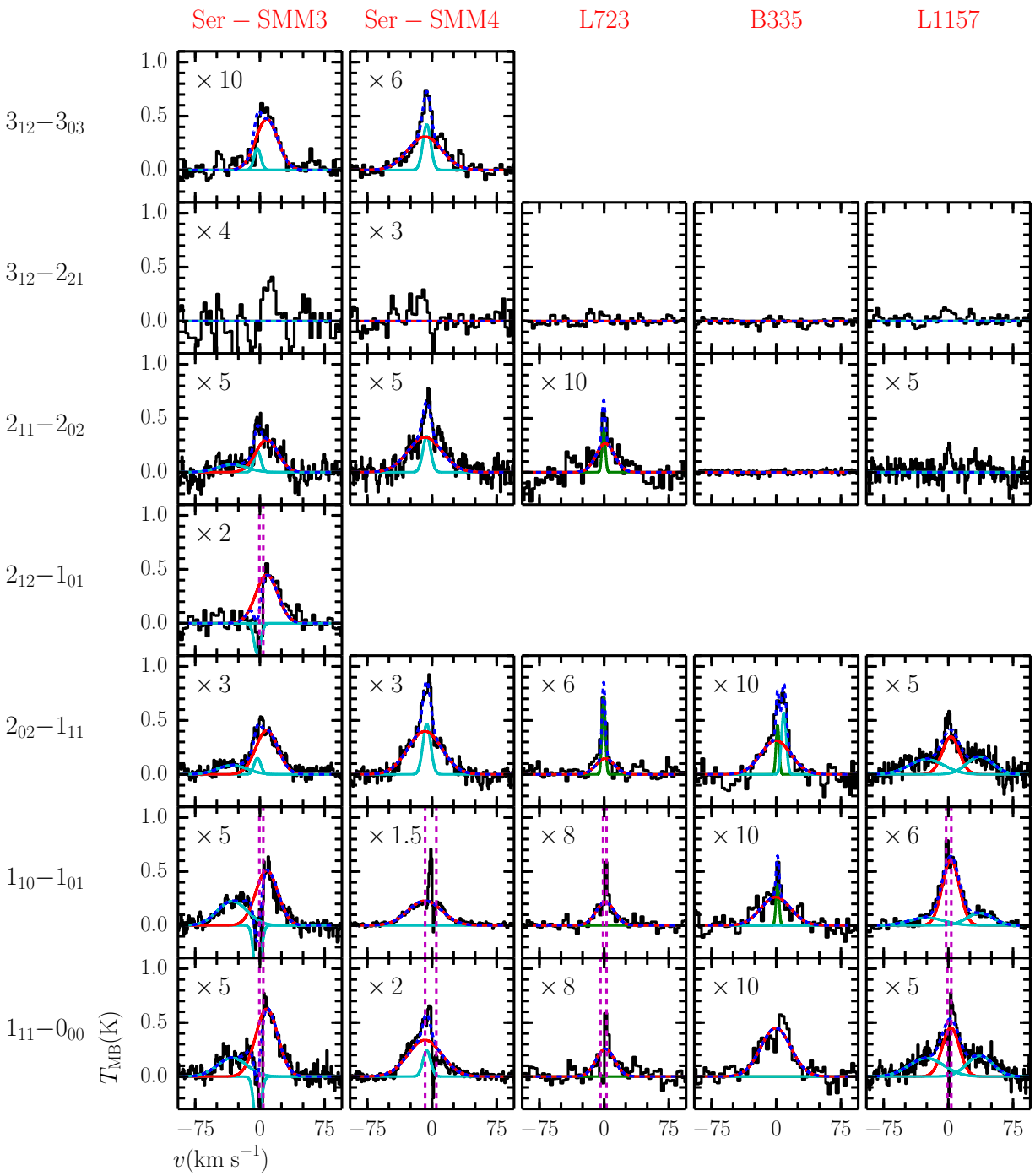

Fig. A.3. As in Fig. A.1.

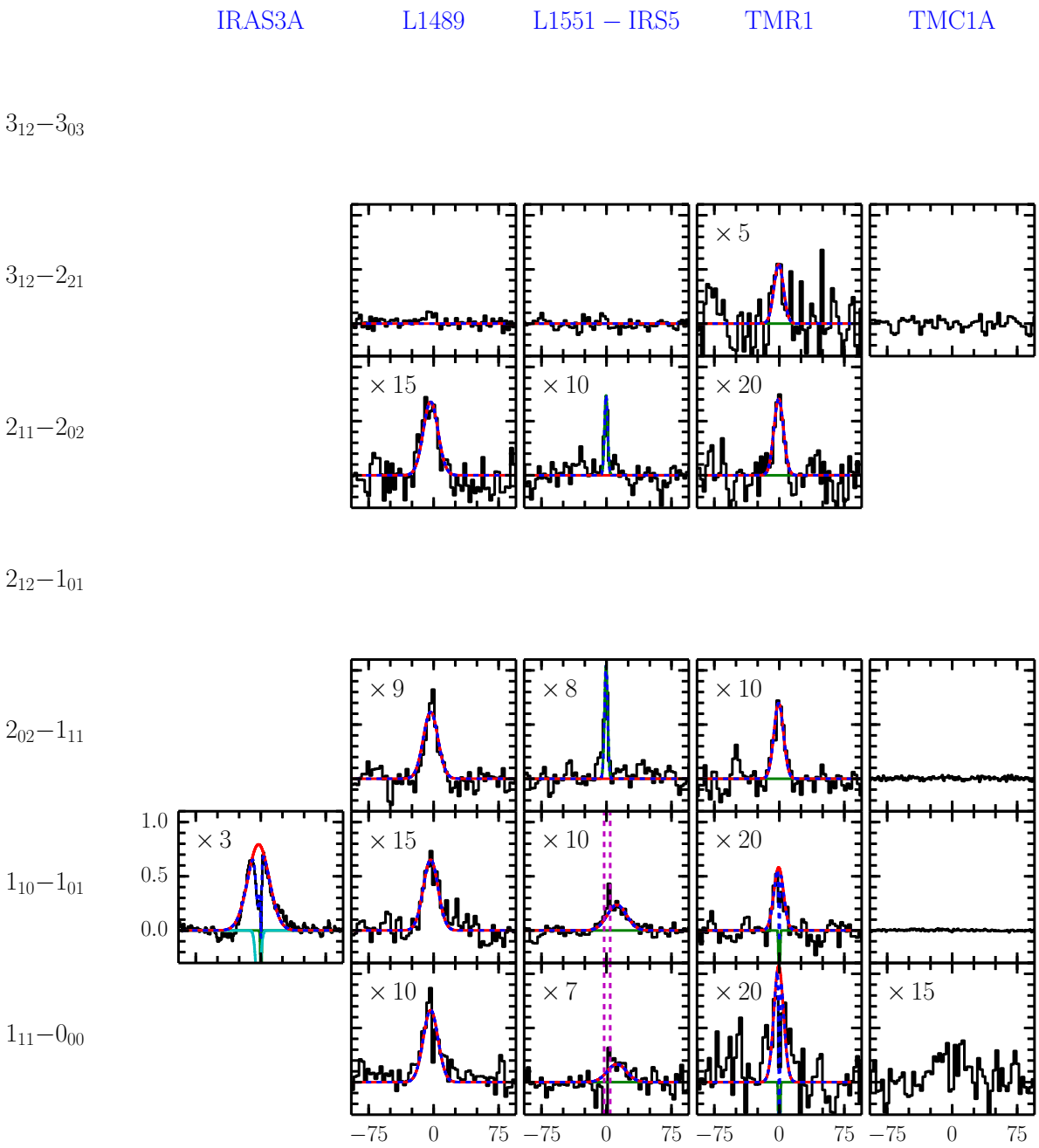

Fig. A.4. As in Fig. A.1 but for Class I sources.

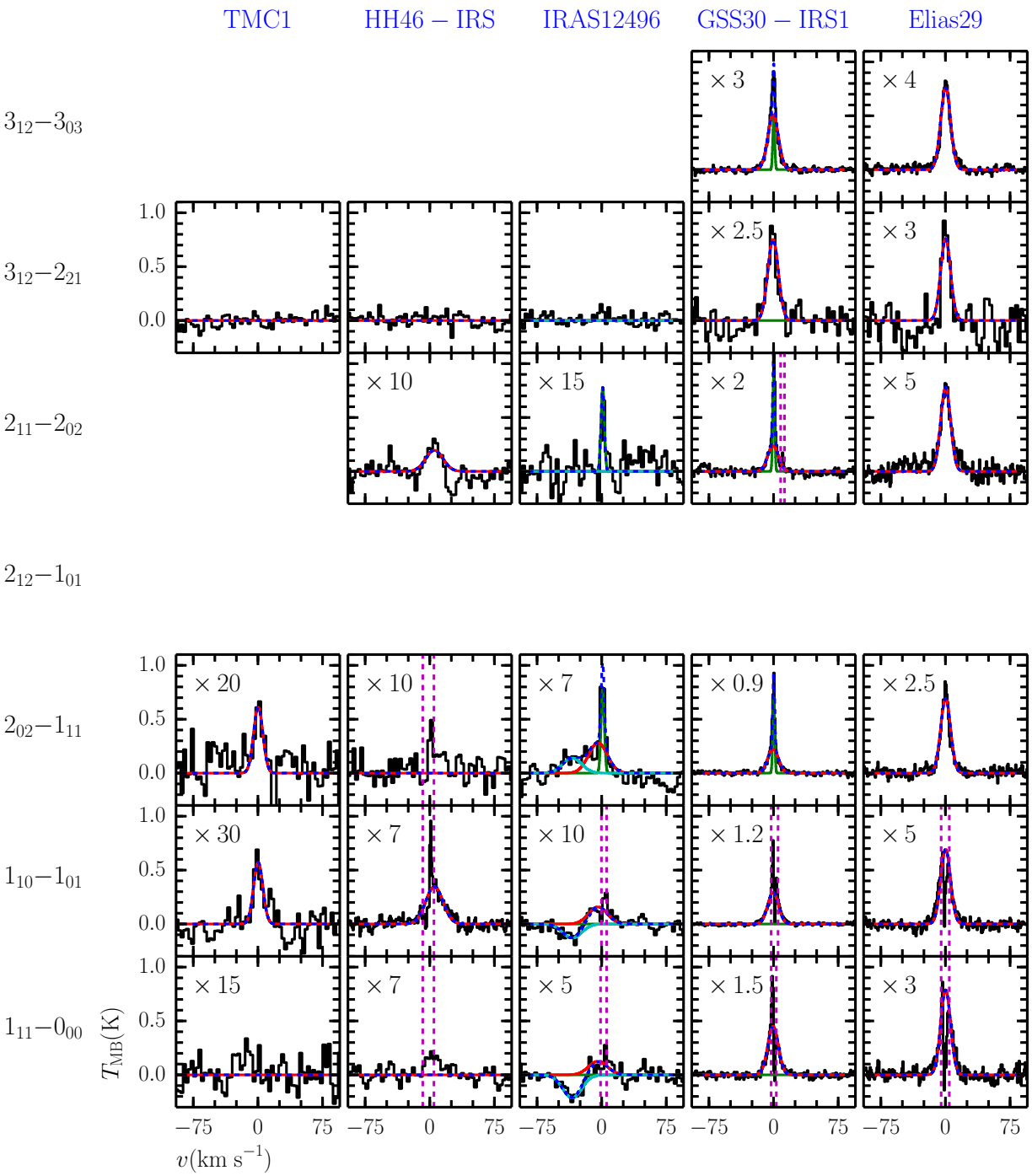

Fig. A.5. As in Fig. A.1 but for Class I sources.

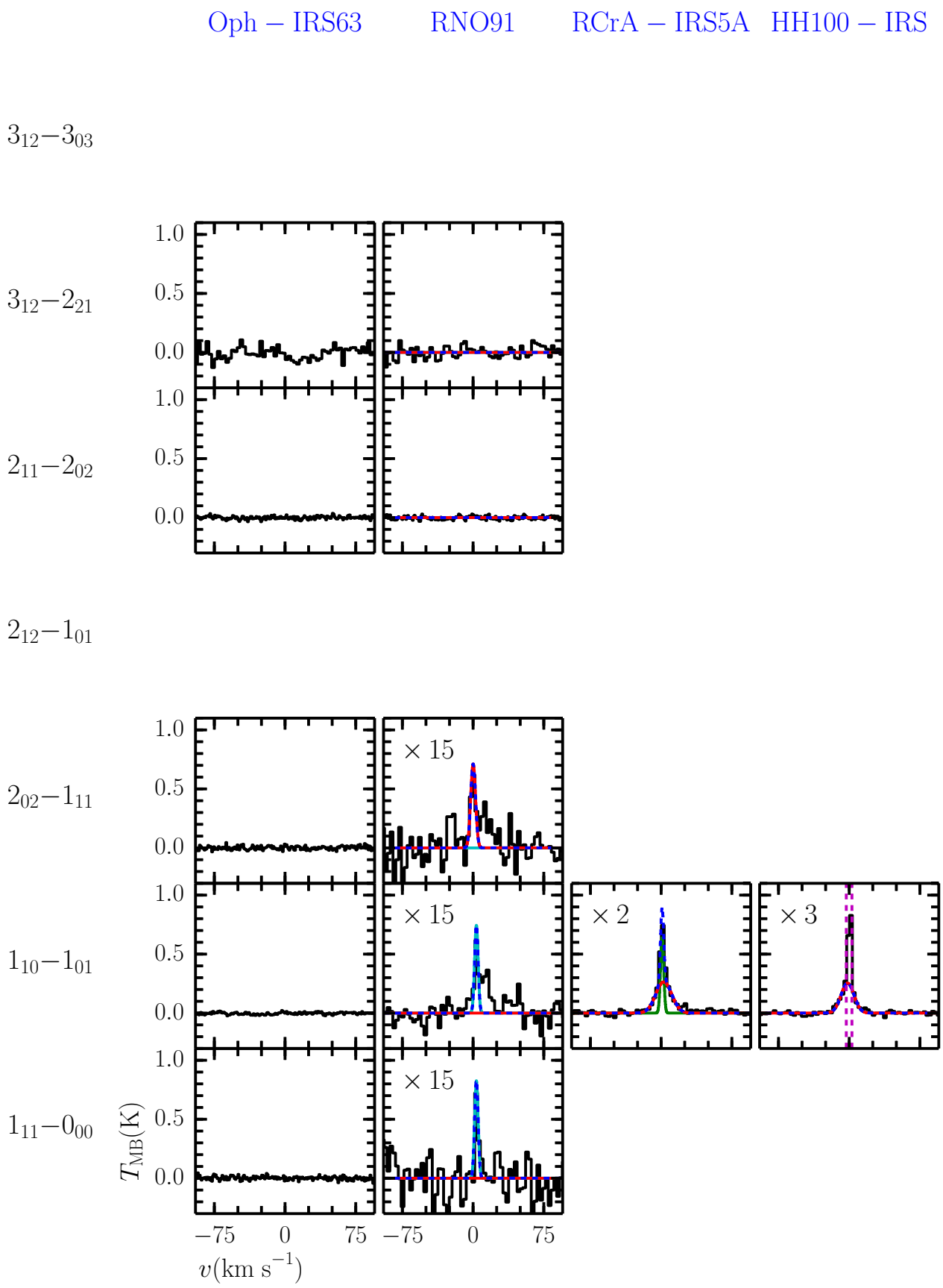

Fig. A.6. As in Fig. A.1 but for Class I sources.

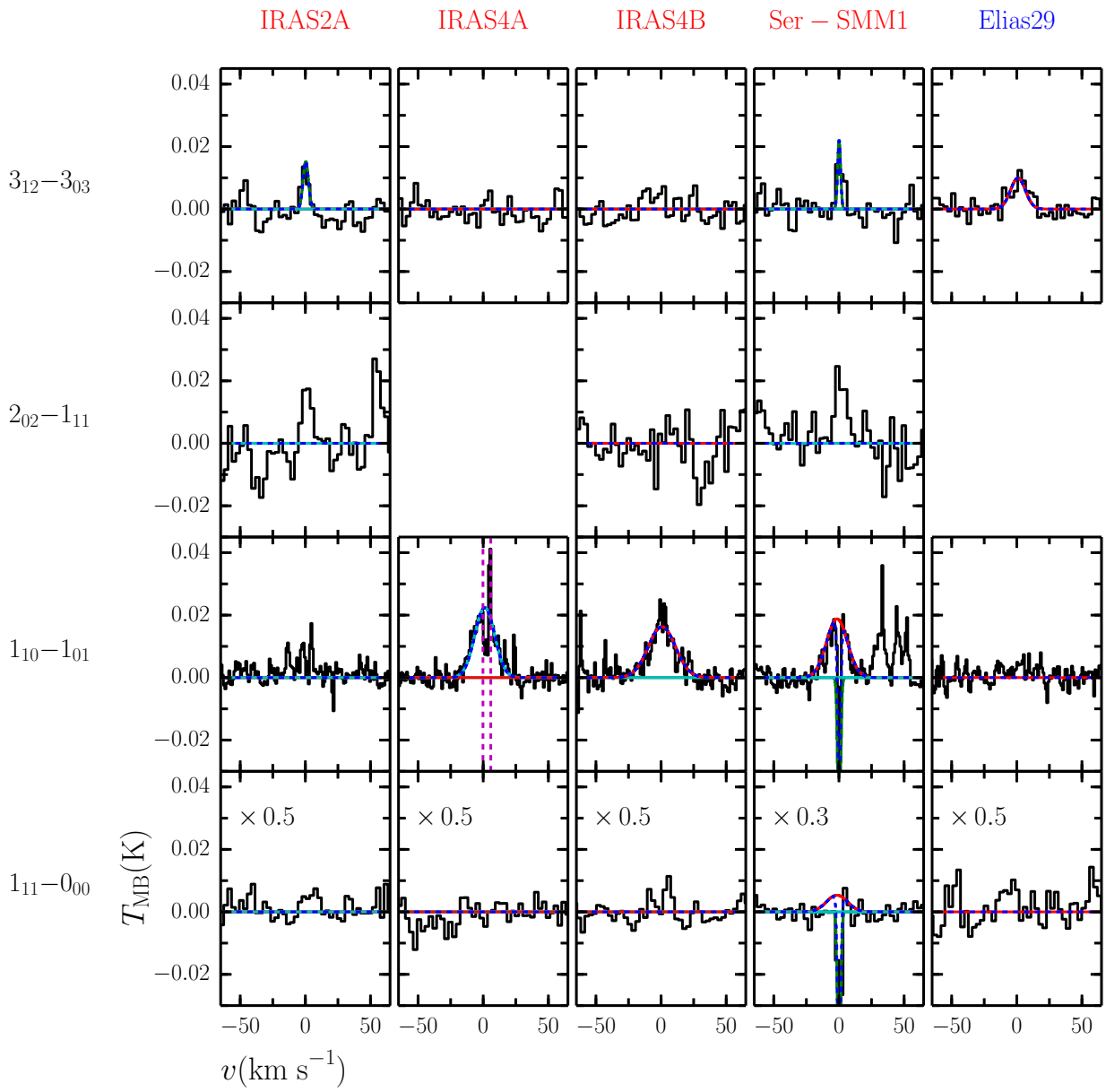

Fig. A.7. Observed $H_2^{18}O$ spectra for those Class 0 (red) and Class I (blue) sources with detections in at least one of the observed transitions. All spectra are continuum-subtracted and have been recentred so that the source velocity is at 0 km s^{-1} for ease of comparison. Some spectra have also been resampled to a lower velocity resolution for ease of comparison. The red, cyan and green lines show the individual Gaussian components for the cavity shock, spot shocks, and quiescent envelope respectively (see text and Table 3 for details) while the blue dashed line shows the combined fit for each line. The vertical dashed magenta lines indicate regions which are masked during the fitting. The $1_{10}-1_{01}$ observations also include the CH triplet which is in the other sideband.

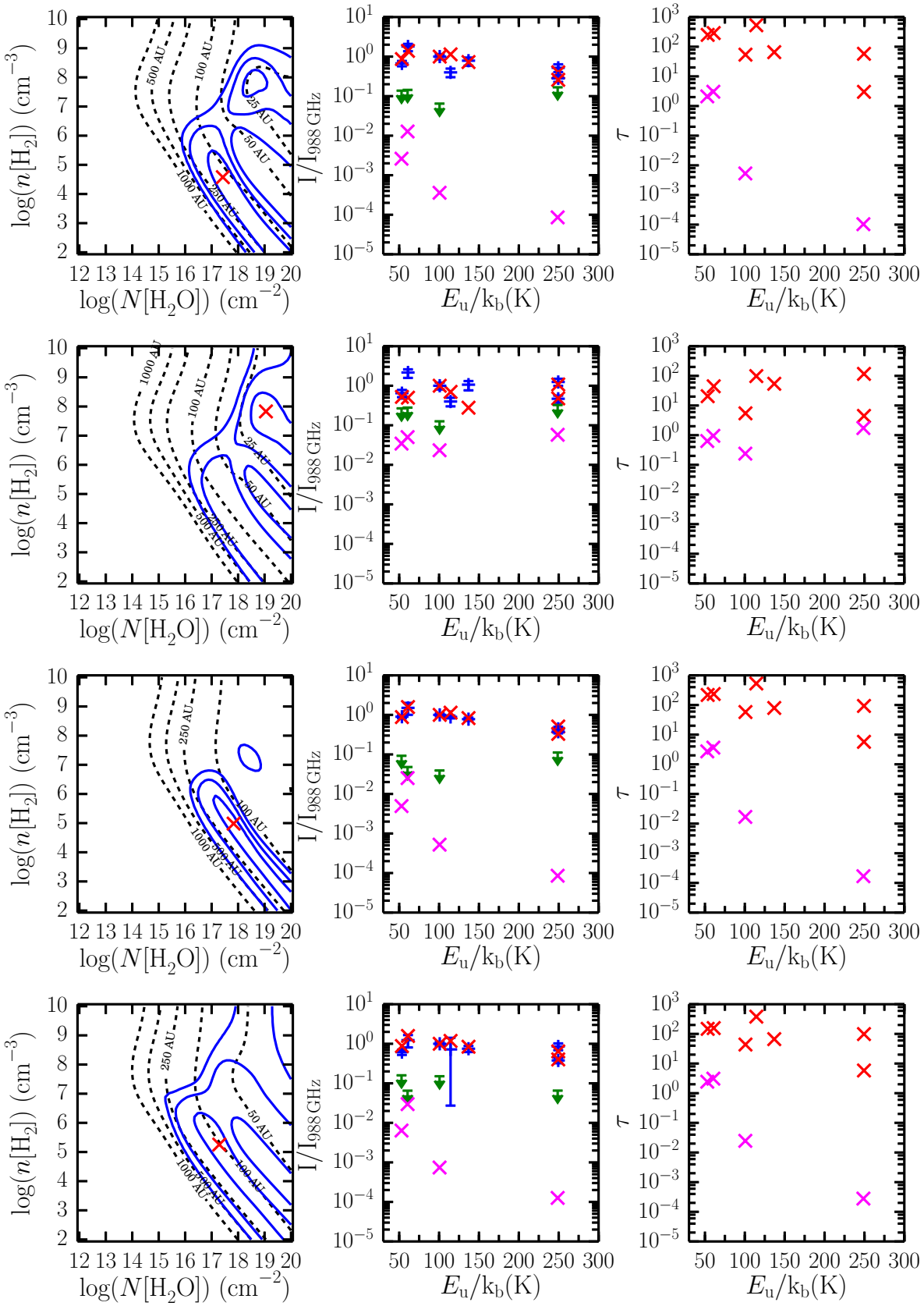

Fig. A.8. RADEX results for the *FWHM* = 23.0 and 39.8 km s^{-1} spot shocks for L1448-MM (*top and upper-middle*) and the cavity shock (*lower-middle*) for L1448-MM and the cavity shock component for IRAS2A (*bottom*). The *left-hand panels* show the best-fit (red cross) and 1, 3 and 5σ confidence limits (blue contours) for a grid in n_{H_2} and N_{H_2O}. The black dashed contours show the corresponding radius of the emitting region. The *middle panels* show a spectral line energy distribution comparing the observed (blue for H_2O, green for $H_2^{18}O$) and best-fit model (red for H_2O, magenta for $H_2^{18}O$) results. The *right-hand panels* show the optical depth for each line for the best-fit model.

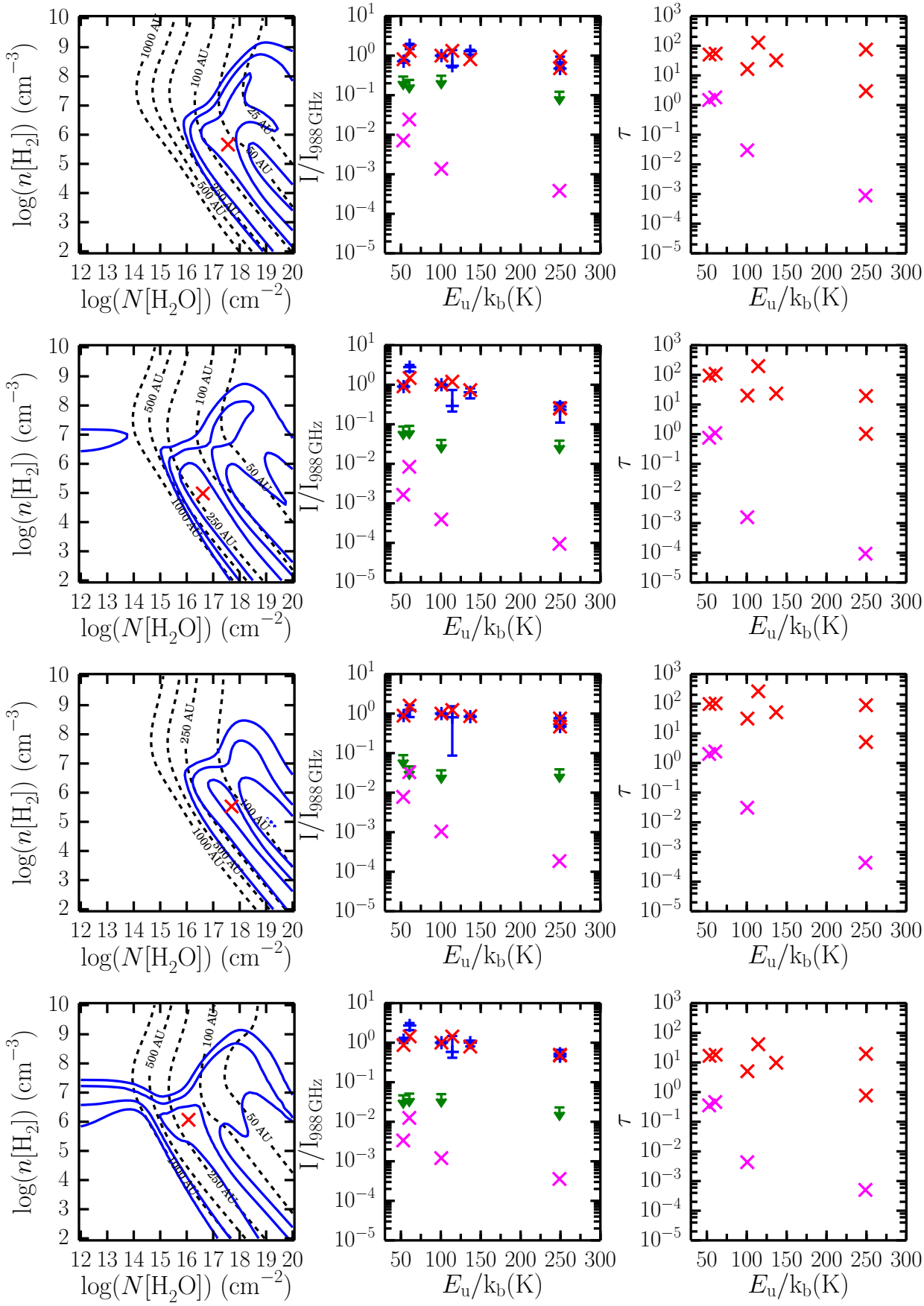

Fig. A.9. As in Fig. A.8 but for the spot shock component of IRAS2A (*top*), the *FWHM* = 9.9 km s^{-1} spot shock and cavity shock components of IRAS4A (*upper and lower-middle*) and the spot shock component of IRAS4B (*bottom*).

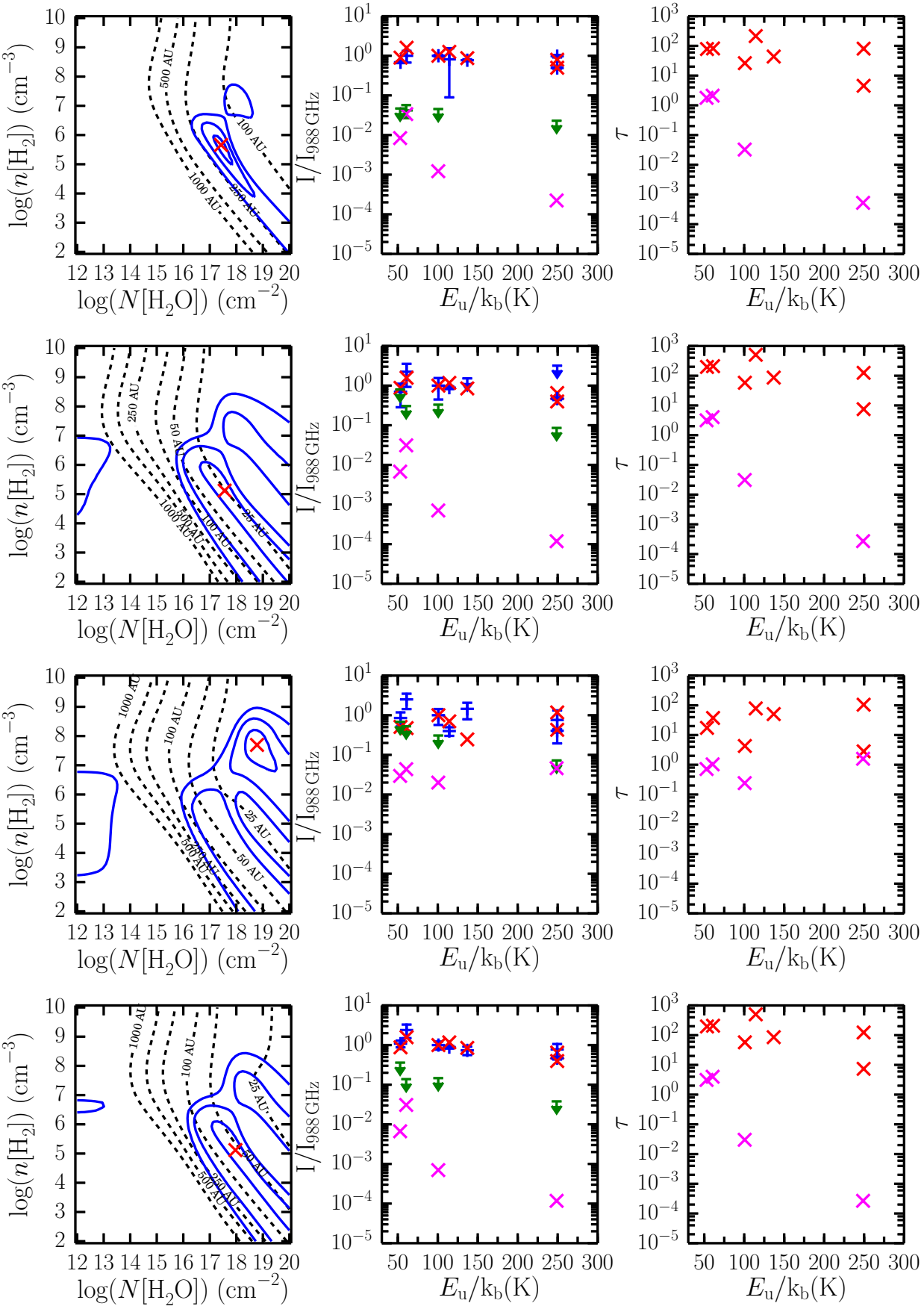

Fig. A.10. As in Fig. A.8 but for the cavity shock components of IRAS4B (*top*) L1527 (*upper-middle*), and the *FWHM* = 28.3 km s^{-1} spot shock and cavity shock components of BHR71.

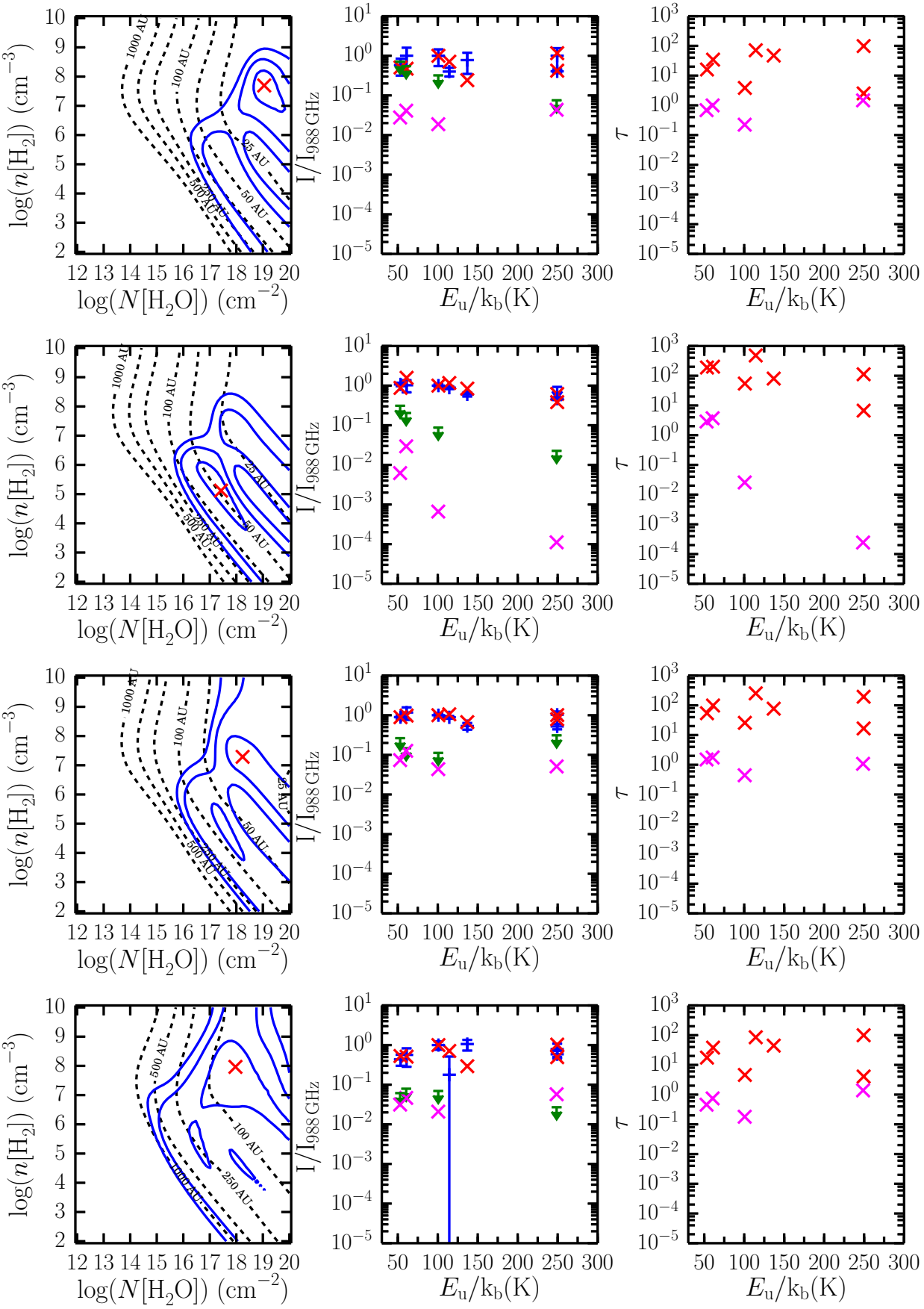

Fig. A.11. As in Fig. A.8 but for the *FWHM* = 59.0 km s^{-1} spot shock of BHR71 (*top*) and the cavity shocks of IRAS 15398 (*upper-middle*), L483 (*lower-middle*) and the *FWHM* = 3.7 km s^{-1} spot shock of Ser-SMM1 (*bottom*).

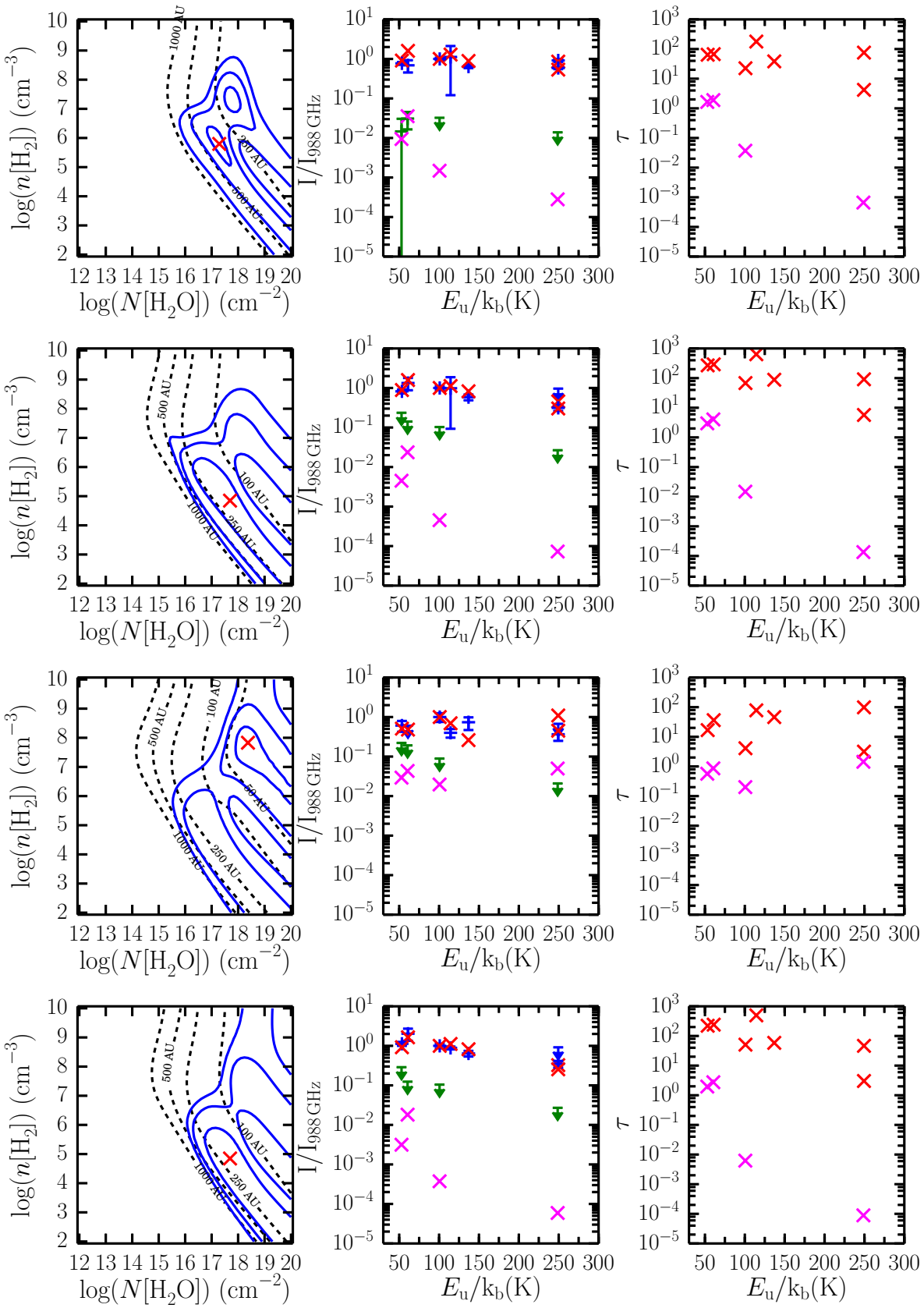

Fig. A.12. As in Fig. A.8 but for the cavity shock of Ser-SMM1 (*top*), Ser-SMM3 (*upper-middle*), the spot shock and cavity shock of Ser-SMM4 (*lower-middle and bottom*).

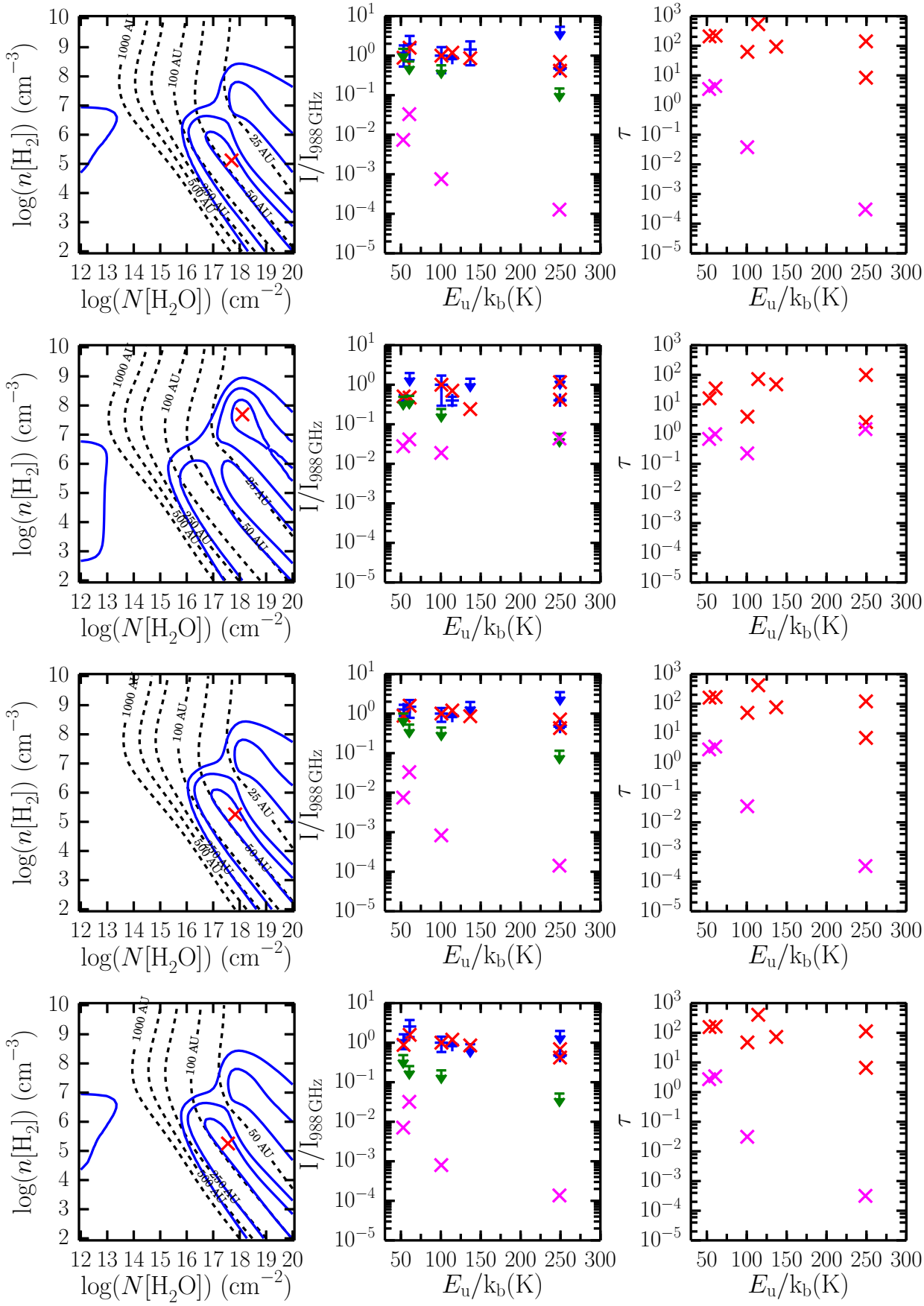

Fig. A.13. As in Fig. A.8 but for the cavity shock of L723 (*top*), the spot and cavity shocks of B335 (*upper and lower-middle*), and the cavity shock of L1157 (*bottom*).

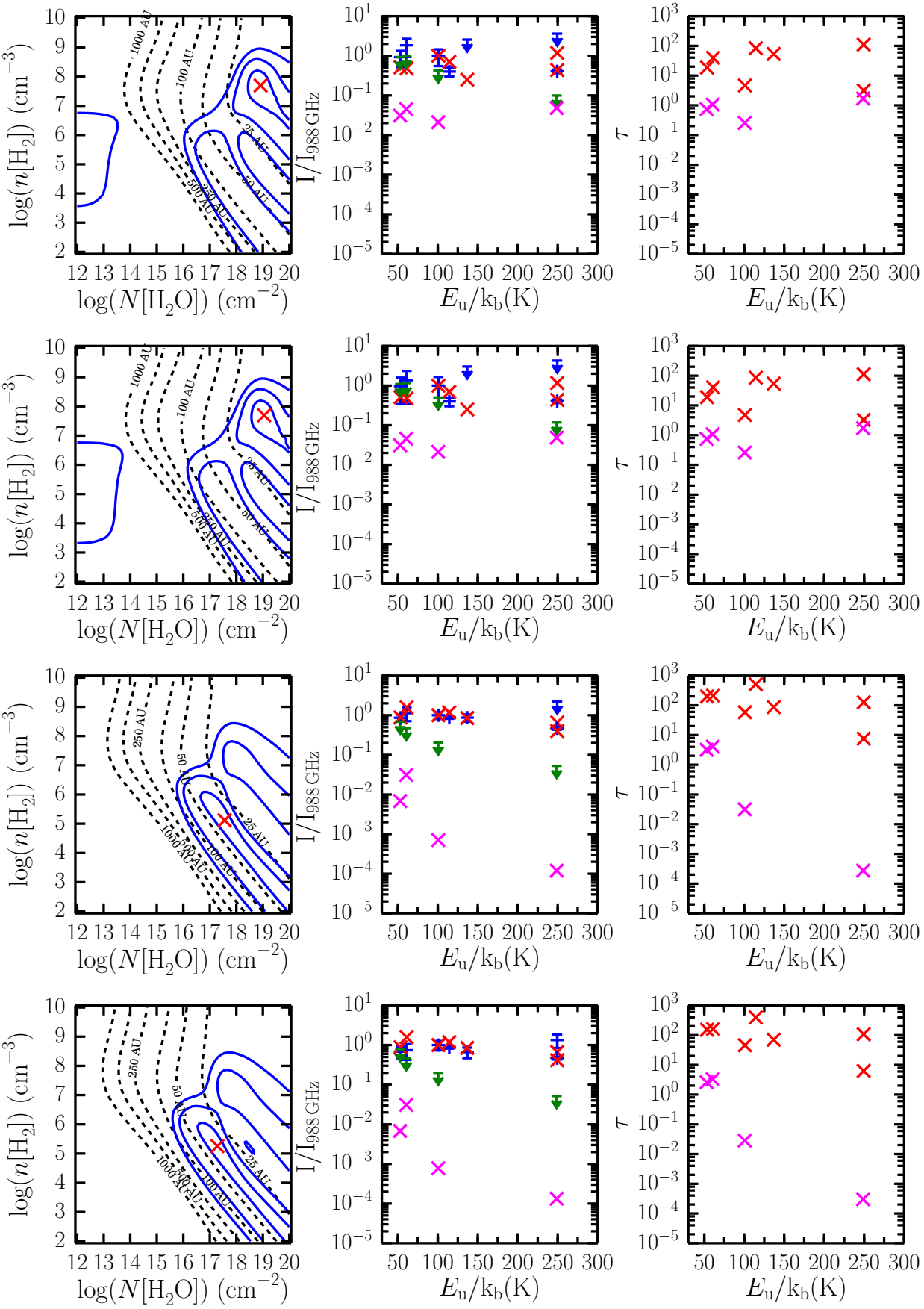

Fig. A.14. As in Fig. A.8 but for the *FWHM* = 35.7 km s^{-1} and 47.7 km s^{-1} spot shocks of L1157 (*top and upper-middle*), and the cavity shocks of L1489 (*lower-middle*) and TMR1 (*bottom*).

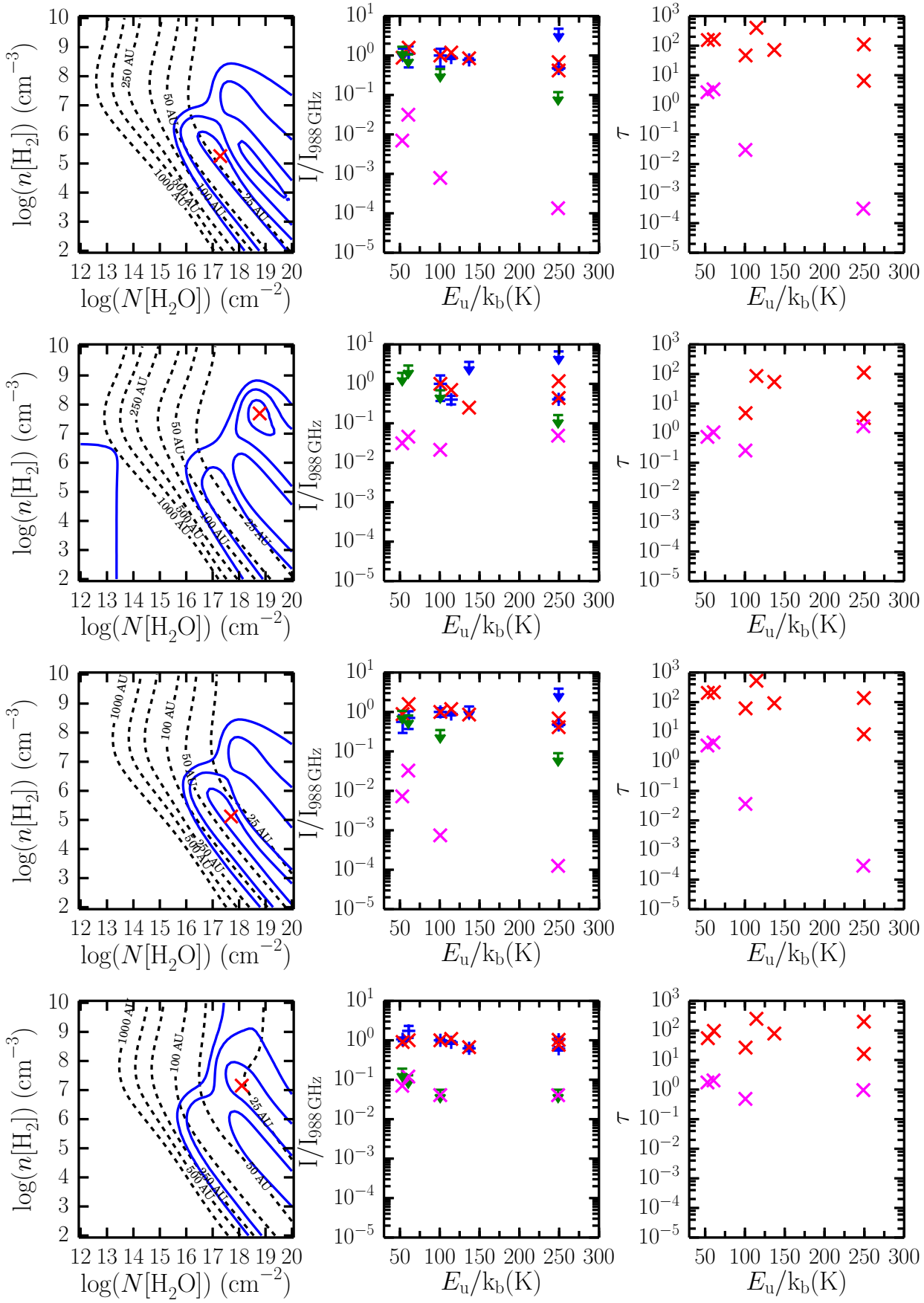

Fig. A.15. As in Fig. A.8 but for the cavity shocks of TMC1 (*top*), the spot and cavity shocks of IRAS 12496 (*upper and lower-middle*) and the cavity shock of GSS30-IRS5 (*bottom*).

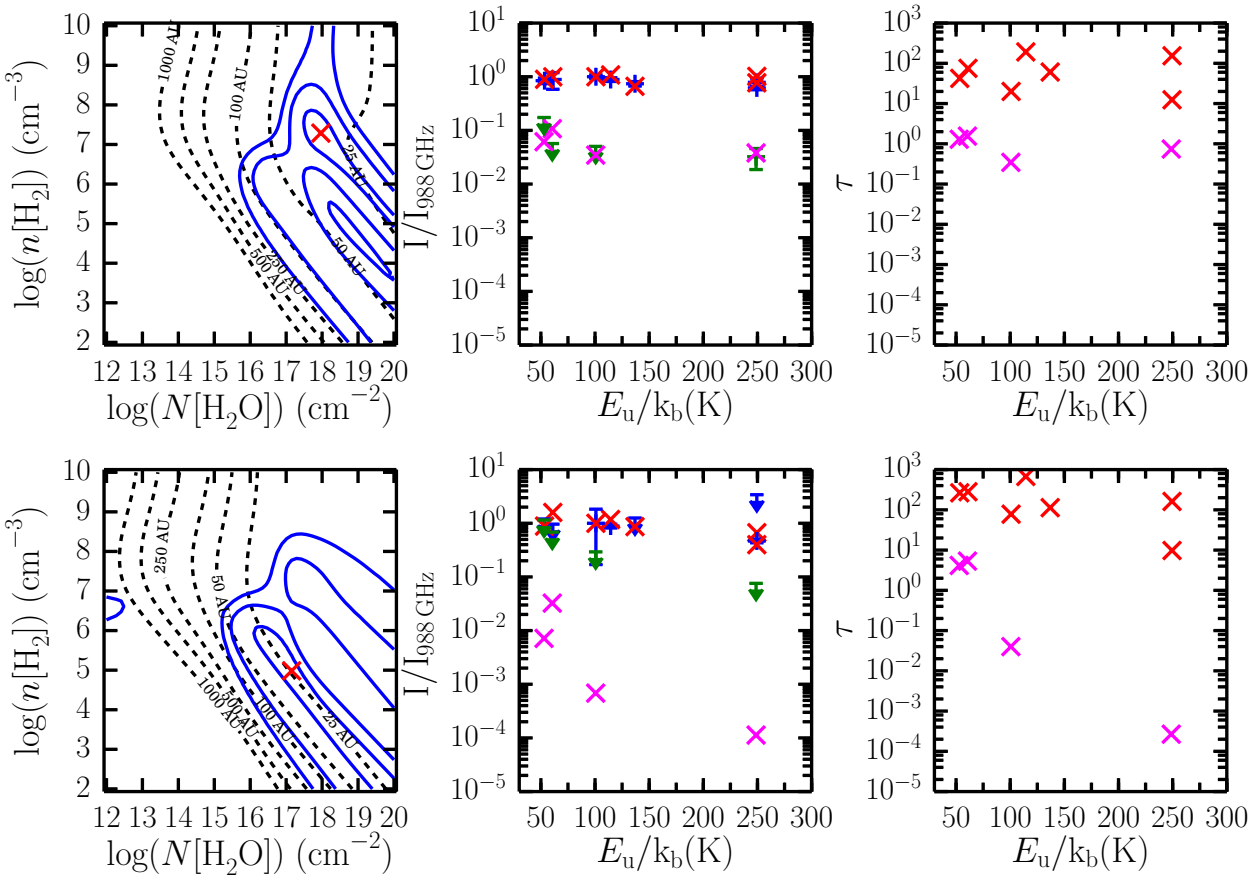

Fig. A.16. As in Fig. A.8 but for the cavity shocks of Elias29 (*top*) and RNO91 (*bottom*).

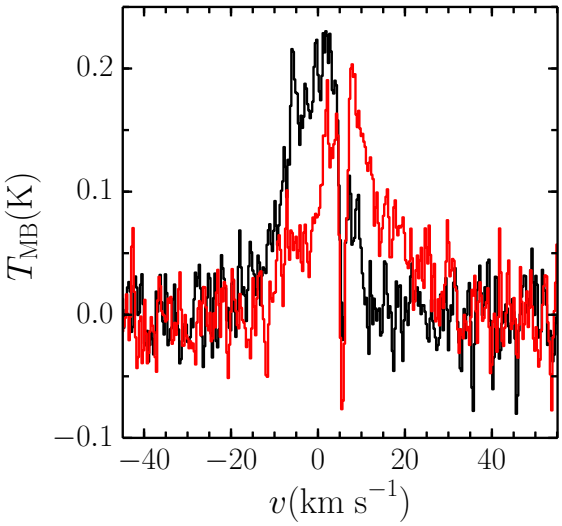

Fig. B.1. Comparison of the H_2O $1_{11}-0_{00}$ observed as part of WISH towards the coordinates and towards the SMA coordinates as part of OT2_evandish_4 (red).

Appendix B: Specific sources

This section discusses in detail the line comparison for three specific sources which require further mention: IRAS 15398, Ser-SMM3 and NGC 1333-IRAS4A.

B.1. IRAS 15398

As noted in Table 1, the position targeted in WISH for a few sources is offset slightly from the source centre as derived by SMA sub-mm interferometric observations. As part of OT2 programme OT2_evandish_4 the H_2O $1_{11}-0_{00}$ line was observed towards the coordinates from Jørgensen et al. (2009). Figure B.1 shows a comparison between the WISH observations (black) and those from OT2_evandish_4 (red, obsid 1342266006). The central absorption and FWHM of the outflow component are broadly the same, though the outflow is centred closer to the source velocity and has a slightly lower $T_{\rm peak}$ value in the newer observations. Ultimately this does not impact the conclusions for this source either in this paper or in Mottram et al. (2013), hence no other lines were re-observed. The $H_2^{18}O$ $1_{10}-1_{01}$ line was also observed towards IRAS 15398 as part of OT2_evandish_4 (obsid 1342266008) with a noise level of 4 mK, but no line emission or absorption was detected.

B.2. Ser-SMM3

Ser-SMM3 is the one source where the line shape seems to vary between the different water transitions. In particular, in Fig. 2 the blue wing of the main outflow component seem to be missing in some of the higher frequency transitions, especially for the $2_{12}-1_{01}$ (1670 GHz) line. This is also one of the few sources to show a shock component in absorption, and it is also blue-shifted with respect to the source velocity. Kristensen et al. (2013) argue that this component is absorbing only against the continuum, which is stronger at higher frequencies. We therefore suggest that the reason the blue wing is decreased or missing in some transitions is due to absorption by the shock component. This source is therefore still consistent with all sources showing no variation in line profile between the different transitions observed with HIFI.

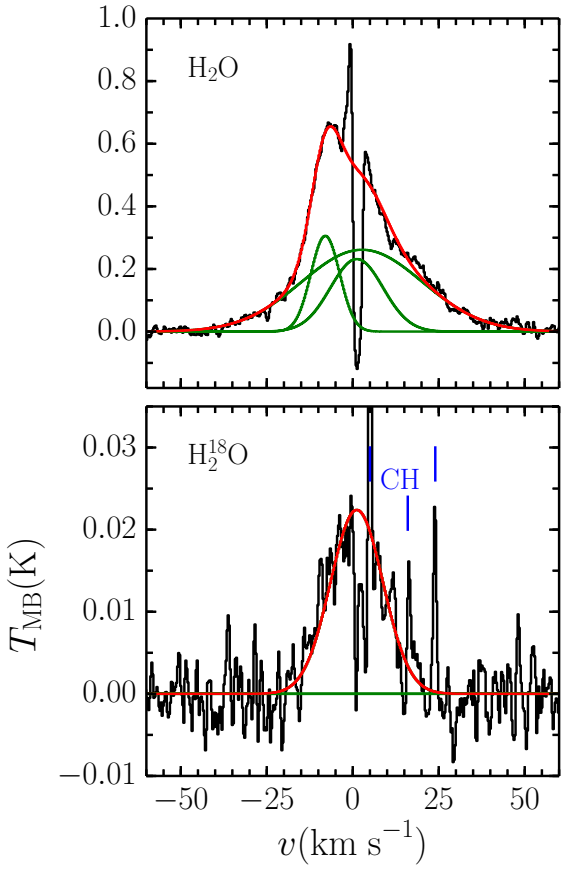

Fig. B.2. Comparison of the $1_{10}-1_{01}$ transitions of H_2O (*top*) and $H_2^{18}O$ (*bottom*) towards IRAS4A. The black lines show the data, the green show the individual Gaussian components while the red shows the combination of all components present in a given line. The blue lines indicate the approximate velocities of the three CH transitions from the other sideband.

B.3. NGC 1333-IRAS4A

Figure B.2 shows a comparison of the H_2O and $H_2^{18}O$ $1_{10}-1_{01}$ observations towards IRAS4A, along with the Gaussian decomposition of those lines. The sharp narrow peaks are due to CH emission in the other side-band and so should be ignored for the following discussion. As discussed in Sect. 3.2 and shown in Fig. B.2, the outflow component (broadest Gaussian) is not detected in the $H_2^{18}O$ observations, but the shock component near the source velocity is. This is also one of the few additional shock components which is approximately at the source velocity and lies in the region occupied by the outflow components in Fig. 7. Unlike any other shock component, the intensity of this component decreases with decreasing beam-size of the observations and it is not detected at all in the $2_{12}-1_{01}$ (1670 GHz) transition, which has a beam-size of 12.7″. There are two off-source shocks in the IRAS4A outflow, B1 and R1, which both lie ∼10″ from the central source. This places at least a part of both B1 and R1 within the beam of most of the on-source observations, with the exception of the $2_{12}-1_{01}$ transition. The R1 position has been observed by Santangelo et al. (2014) and shows similar line-width to the on-source shock component. We therefore conclude that this component is coming from the B1 and/or R1 off-source shocks.